MODELING OF COMPLEX MOLECULES ADSORBED ON COMPLEX COPPER SURFACES

A Dissertation
Presented to
The Academic Faculty

by

Daniel S. Wei

In Partial Fulfillment
of the Requirements for the Degree
Doctor of Philosophy in the
School of Chemical and Biomolecular Engineering

Georgia Institute of Technology
December 2014

MODELING OF COMPLEX MOLECULES ADSORBED ON COMPLEX COPPER SURFACES

Approved by:

Dr. David S. Sholl, Advisor
School of Chemical & Biomolecular Engineering
Georgia Institute of Technology

Dr. Michael A. Filler
School of Chemical & Biomolecular Engineering
Georgia Institute of Technology

Dr. Dennis W. Hess
School of Chemical & Biomolecular Engineering
Georgia Institute of Technology

Dr. Carsten Sievers
School of Chemical & Biomolecular Engineering
Georgia Institute of Technology

Dr. Thomas Orlando
School of Chemistry and Biochemistry
Georgia Institute of Technology

Date Approved: November 10, 2014

To my wife, Jiayi Shen, and my parents, I-Chien Wei and Huey-Jin Shen

ACKNOWLEDGEMENTS

The work presented in this thesis was conducted in the School of Chemical and Biomolecular Engineering at the Georgia Institute of Technology in Atlanta, Georgia. The thesis was the culmination of four years of work between January 2010 and November 2014. Here, I would like to acknowledge those whose assistance has helped me to complete this work.

First of all, I would like to express my immense gratitude towards Dr. David S. Sholl, my thesis advisor. It is through his support, confidence, and patience in me that I may progress to the conclusion of my thesis. His enthusiasm, intellectual curiosity, and work ethic had set an excellent example for me and had pushed me to bring my best skills to the table on a daily basis.

I would like to express my appreciation to Dr. Bharat Mhatre, Dr. Yongju Yun, and Dr. Andrew Gellman at Carnegie Mellon University in Pittsburgh, PA, Guo Shiou Foo and Dr. Carsten Sievers at Georgia Institute of Technology in Atlanta, GA, and Dr. Timothy Lawton, Dr. Vladimir Pushkarev, and Dr. Charlie Sykes at Tufts University in Boston, MA. Their experimental data and insight into the surfaces have greatly bolstered the impact and influence of this thesis. I would also like to thank Dr. Thomas Orlando, Dr. Michael Filler, and Dr. Dennis Hess, my committee members, for their helpful comments and suggestions.

I would also like to thank all the current and previous Sholl group members: Dr. Shiqiang Hao, Dr. Taku Watanabe, Dr. Thomas Manz, Dr. Ji Zang, Dr. Mohamad Kassaee, Dr. Xuerong Shi, Dr. Hanjun Fang, Dr. Iyad Hijazi, Dr. Salah Boulfelfel, Dr. Veronika

Walkosz, Dr. Rongshun Zhu, Dr. Melissa Lucero, Dr. Sung Gu Kang, Dr. Emmanuel Haldoupis, Dr. Dieh Teng, Dr. Ambarish Kulkarni, Dr. Nita Chandrasekhar, Dr. Liwei Li, Dr. Kelly Nicholson, Timothy van Heest, Rohan Awati, Alex Fergusson, Namory Keita, Jaeyub Chung, Seung Won Choi, Byeong Jae Chun, Jason Gee, Jeff Camp, Hakan Demir, Brandon Plaisance, Krishna Chandran Jayachandrababu, Ross Verploegh, and Dalar Nazarian. Specially, I would like to thank Dr. Shiqiang Hao and Dr. Taku Watanabe for helping me with the various DFT problems when I first joined the group. I would also like to extend a special thank Dr. Kelly Nicholson for providing valuable suggestions, reviews, and comments throughout my researches and publications.

Finally, I would like to thank my wife, Jiayi Shen, my mother, Huey-Jin Shen, and my father, I-Chien Wei, who are always there for me.

Daniel S. Wei, 10 Nov 2014

TABLE OF CONTENTS

LIST OF TABLES

Page

LIST OF FIGURES

Page

SUMMARY

There has been growing demands towards the efficient production of enantiopure compounds through either asymmetric synthesis or separation from racemic mixtures. Recent studies have examined numerous different methods that may address this challenge. One of these methods involved the interaction of chiral molecules on achiral metal surfaces such as copper to create chiral templates while another method utilizes the interaction of chiral molecules on intrinsically chiral surfaces. Earlier studies using nonhybrid Density Functional Theory (DFT) functional has provided some insights into the geometric structures and relative energies of some of these interactions, but it failed to achieve quantitative agreement with experimental studies. Using dispersion corrected DFT functionals, this thesis present a study of chemisorbed dense adlayers of glycine and alanine on Cu(110) and Cu(3,1,17), physisorbed R-3-methycyclohexanone (R-3MCHO) on Cu(100), Cu(110), Cu(111), Cu(221), and Cu(643)^R, and the hydrogenation of formaldehyde and methoxide on Zn or Zr heteroatoms promoted Cu surfaces.

In the dense glycine and alanine adlayer study, we have resolved a disagreement between experimental observation made on LEED, STM, and XPD, and we showed that heterochiral and homochiral glycine adlayer coexist on Cu(110). Our model failed to show the minute enantiospecificity for dense alanine adlayer on Cu(3,1,17) which indicated a numeric limitation for computational modeling of surface adsorption. In the physisorbed system, the dispersion corrected methods calculated adsorption energies were in better quantitative agreement with the experimentally observed values than the nonhybrid functionals, but it also created a significant overestimation of total adsorption

energies. On the other hand, our model had indicated a previously unexpected adsorbate-induced surface reconstruction on Cu(110). This is promising news in term of computational modeling's capability in examining surface-adsorbate interaction on an atomic scale. As for the hydrogenation of formaldehyde and methoxide on copper surfaces, the model showed that the increased binding strength between the reaction intermediates and the heteroatom promoted copper surfaces to be the primary contributor of the increased reaction rates. Furthermore, our model had also indicated that while clustered heteroatoms are relatively rare, a significant portion of reaction takes place near these clustered structures. It is our hope that the results and techniques presented in this thesis can be used to better understand and predict the interaction of more complex surface-adsorbate interactions.

CHAPTER 1

INTRODUCTION

1.1 Introduction

A hallmark of life on Earth is the homochirality of biomolecules such as amino acids, sugars, proteins, and DNA.[1-2] Chirality is the condition in which two molecules of identical composition is arranged such that they represented a non-superimposable mirror images of each other. In the homochiral environment of living organisms, one consequence is that the two enantiomers of a chiral molecule can exhibit significantly different physiological effects.[3-5] For instance, the well-known case of thalidomide where one enantiomer led to severe birth defect demonstrated the importance of enantiospecificity in pharmaceutical. This has created an enormous >$200 billion per year market, particularly in pharmaceuticals, for enantiomerically pure compounds.[6] As a result, enantioselective chemical processes, such as enantioselective catalyst, biocatalyst, and chiral pool synthesis, have attracted a great deal of attention in the biochemical and pharmaceutical industries because they allow for the creation of more enantiopure compounds. The subject of this work, chiral surfaces, may be very attractive for chiral separations and heterogeneous catalysis if enantioselectivity can be achieved.

The most common method for creating single enantiomer chiral surfaces is the irreversible adsorption of enantiomerically pure, chiral organic molecules on achiral metal surfaces, which thereby renders the surfaces chiral.[7-10] Such surfaces can then serve as enantiospecific adsorbents or catalysts; however, their chemical and thermal stabilities are limited by the intrinsic stability of the organic modifier. On the other hand, simple metal surfaces themselves can be much more stable and catalytically active than organically modified surfaces, if prepared in intrinsically chiral form. Although the bulk crystal structures of metals are achiral, intrinsically chiral surfaces can be obtained by cleaving the metal through the (*hkl*) plane where $h \neq k \neq l \neq 0$ which exposed a low symmetry, high Miller index chiral surface.[11-12] Because the terrace−step−kink structures of these surfaces lack symmetry, they are not superimposable on their mirror images and are, therefore, chiral. When adsorbed on naturally chiral surfaces, chiral molecules exhibit enantiospecific desorption kinetics,[13-16] reaction kinetics,[17-18] orientations,[19-20] electrochemistry,[21-22] etc. Various methods have been widely used to study these behaviors.[14, 23-28]

In a variety of experiments chiral surface structures have been shown to exhibit enantiospecific chemical characteristics.[4, 29-32] For example, experimental data obtained using temperature-programmed desorption (TPD) have demonstrated a measurable difference between the adsorption energies of enantiomers on chiral surfaces.[33-37] Currently, large scale studies of all adsorbed enantiomer−surface combinations are very challenging to do experimentally. However, an improved fundamental knowledge of enantiomer−surface interactions will allow experimental studies to narrow the focus to combinations with the most enantiospecific potential.

Recent advances in computational capacity and efficacy has allowed researchers simulate real systems with better accuracy. Using density functional theory (DFT), it is possible to model the adsorption of molecules on surfaces using quantum chemistry principles. While earlier work using DFT yielded promising results that agree with experimental trends,[38-42] the calculated results did not yield quantitatively accurate adsorption energy for the adsorbed molecules. This is typically attributed to a shortcoming of the nonhybrid functionals used in these calculations, which fail to correctly describe long-range van-der-Waals forces.[43] In recent years, several approaches have been developed within the DFT community to address this issue.[44-47] In this work, we examine the ability of these methods to narrow the accuracy gap between computational and experimental results, and we investigate van der Waals forces dominated physisorbed system systems to gain fundamental knowledge which would facilitate future studies.

1.2 Chemisorption of chiral D- and L- alanine on the chiral Cu(3,1,17)^S

Previous studies have shown that adsorption energies calculated by DFT tracks closely with the experimental results when surface adsorption is not dominated by van der Waals forces. Glycine, the simplest amino acid, is achiral in the gas phase, but, when adsorbed onto a flat surface, it becomes chiral.[48-50] Initial experiments were in disagreement on the structure of dense glycine adlayer on Cu(110).[49-50] Chen et al. concluded that heterochiral and homochiral domains coexist based on low-energy electron diffraction (LEED) and scanning tunneling microscope (STM) images, but Toomes et al. concluded from X-ray photoelectron diffraction (XPD) measurements that only one domain exists. To address this inconsistency, Rankin and Sholl investigated the structures of glycine and alanine, the simplest chiral amino acid, on atomically flat Cu surfaces using DFT.[51-56] Their calculations showed a slight preference for the heterochiral footprint domain for glycine on Cu(110) surface, and this domain was in quantitative agreement with the results obtained by Toomes et al. Furthermore, there were no observable differences between adsorption of D- and L- alanine on Cu surfaces, indicating the enantiomers are unlikely to separate into enantiospecific domains as suggested by Chen et al. This was later validated by further experiments.[57-60]

1.3 Physisorption of R-3-methycyclohexanone on Cu surfaces

To examine the impact of dispersion forces on the adsorption of molecules on metal surfaces, it is natural to consider examples where dispersion forces are expected to dominate the adsorption energy. 3-methylcyclohexanone (3MCHO) is an ideal model for a chiral adsorbate. It has been extensively studied and shown experimentally to undergo enantiospecific separation on chiral Cu surfaces.[34-35] STM conducted by Zhao and Perry indicates ordered adsorption of 3MCHO on the Cu(643) surface.[61] Additionally, 3MCHO adsorbed on the step edges of Cu(533) and Cu(221) surfaces created enough surface stress to induce kink formation.[62] Previous work by Bhatia and Sholl investigated 3MCHO adsorption on Cu surfaces with plane wave DFT with PW91-GGA functional. They calculated the adsorption energy on straight step edge and kink sites to be 0.09 and 0.36 eV more favorable than on the Cu(111) terrace, respectively. Experimental data show similar differences in adsorption energy between the three different surfaces, but indicate ~0.45 eV more favorable absorption energies for each surface than calculated by DFT. This underestimation is expected since the nonhybrid functional used by Bhatia does not account for dispersion forces.[38] Since the energy differences between straight edge, kink site, and the flat surfaces are consistent with the experimental results, the absolute difference is likely a result of systematic error in which the dispersion force contribution from the cyclohexane ring was not entirely accounted for in the PW91 functional. This inference is supported by experiments that estimate the cyclohexane adsorption energy to be ~0.53 eV.[63] While ~0.53 eV is slightly stronger than the ~0.45 eV underestimation calculated by the nonhybrid functional, it strongly support the notion that dispersion corrected methods will allow for a more accurate estimation of adsorption energies. Whether dispersion corrected functionals can close the gap with regard to quantitative accuracy will impact their ability to model surface adsorption of complex molecules.

The understanding and practical application of enantiospecific processes involving metal surfaces demands detailed knowledge of the geometry, aggregation pattern, and energies of adsorbed molecules. These issues are also important in the broader context of multifunctional molecules adsorbed on catalytic surfaces, as, for instance, in catalytic treatment of biomass-derived molecules.

1.4 Promoter impact on kinetics of methanol formation on Cu surfaces

Methanol is a highly sought after commodity chemical with applications in transportation and as a chemical feedstock. Its global demand exceeds 65 million tons/yr, generating $36 billion/yr in economic activity. Industrially, methanol is currently synthesized by reacting mixtures of H_2, CO_2, and CO at elevated temperature (400 – 600 K) and pressure (50 – 100 atm) with $Cu/ZnO/Al_2O_3$ catalysts.[64-67] With increased demand for greenhouse gas mitigation and advancements in carbon capture technology, there has been growing interest in using captured CO_2 to fuel the methanol synthesis.[65, 67-72] This, in part, drives the demand to develop a strategic, rational design of heterogeneous catalysts. One major roadblock lies in the complexity of catalyst surface structures and its impact on reaction mechanisms. While the metallic Cu catalyst is generally accepted to be structure sensitive, the exact mechanism and step impacts are uncertain. Several preliminary studies have examined these effects.[65-67, 73] Behrens et al. has proposed that small amounts of Cu surface, activated by presence of Zn atoms, contribute the majority of catalytic activity during methanol synthesis.[67] An improved understanding of surface structure and promoter impact on this particular segment may assist in the rational design of future catalysts. In this spirit, we use DFT to determine the positions and behaviors of Zn and Zr atoms on Cu surfaces and investigate the impact of these heteroatoms on the adsorption energies of MeOH synthesis intermediates and on the reaction barriers for key reaction steps.

1.5 Thesis summary

In order to improve the fundamental understanding of these surface−adsorbate interactions and to benchmark DFT capabilities, we present a broad study that encompasses several different types of surface−adsorbate interactions. Additionally, we collaborated extensively with an experimental group supervised by Dr. Andrew Gellman at Carnegie Mellon University.

We first provide a brief overview of DFT in Chapter 2, which served as the primary computational modeling method throughout our work.

In Chapter 3, we re-examine the chemisorption of glycine and alanine on Cu using dispersion corrected DFT functionals. For glycine and alanine on flat Cu surfaces, the chemisorption contribution from the deprotonated carboxylic group dominates the adsorption energy, and the adsorbates are horizontally stabilized by two hydrogen bonds per molecule. These effects diminish the influence of van der Waals forces on surface geometry. When dispersion force corrections are applied, the total adsorption energy will increase, but we do not expect changes to the overall adlayer structure. To quantify the overall effect of van der Waals forces on these chemisorbed molecules, we first examine the adsorption of dense glycine and alanine adlayer on Cu(110) with dispersion corrected calculations. Then we attempt to describe the equilibrium adsorption of D- and L-alanine mixtures on naturally chiral Cu(3,1,17) surfaces both through computational simulation and direct measurement. The combined experimental and computational studies provide insight into the enantioselectivity of chiral amino acid adsorption on naturally chiral surfaces.

In Chapter 4, we investigate R-3MCHO adsorption on Cu surfaces as a benchmark test for the three dispersion corrected methods and to quantify the effectiveness of these methods for predicting surface–adsorbate interactions. The incorporation of dispersion forces potentially makes it possible to study and model the adsorption behavior of large compounds on surfaces with quantitative accuracy. We compare the utility of three dispersion-corrected DFT methods: (1) Grimme's D2, (2) vdW-DF with optB86b, (3) and vdW-DF with optB88. Using physisorbed 3MCHO, we quantify the efficacy of the dispersion force functional in terms of absolute adsorption energy accuracy on three flat Cu surfaces. Since the goal is to probe the utility of DFT calculations in screening for enantiospecific processes that operate on low and high Miller index Cu surfaces, studying interactions of compounds with flat surfaces alone is not sufficient. Therefore, we model R-3MCHO adsorption on Cu(221), a surface with straight step edges and Cu(643), an intrinsically chiral surfaces. These surfaces were picked for the availability of experimental results and the large terrace of Cu(111) which allows for greater symmetry and reduces the number of surface geometries that needs to be examined.

In Chapter 5, we expand upon the work of Behrens et al.[67] and present a computational study of the impact of Zn and Zr heteroatoms and surface structures of Cu catalyst on methanol synthesis under typical methanol synthesis temperature of 500 K.[64-67] We first utilize DFT to determine the positions and behaviors of Zn and Zr heteroatoms on Cu surfaces. Our study then investigated the impact of these heteroatoms on the overall adsorption of the reaction intermediates. We further investigate the influence of clustered heteroatom on the adsorption of these intermediates. Additionally, we examine the adsorption of these intermediates on different Cu stepped orientations. Finally, we probe the impact of heteroatom on the adsorption of reaction intermediates on Cu kinked sites.

In Chapter 6, we conclude the major results found in this thesis and outline challenges and opportunities for future works.

1.6 REFERENCES

1. Bonner, W. A., The Origin and Amplification of Biomolecular Chirality. *Orig Life Evol Biosph* **1991,** *21* (2), 59-111.

2. Bada, J. L., Biomolecules - Origins of Homochirality. *Nature* **1995,** *374* (6523), 594-595.

3. Merino, I. M.; Gonzalez, E. B.; Sanzmedel, A., Liquid-Chromatographic Separation of Penicillamine Enantiomers Derivatized with Opa/2-Me on a Beta-Cyclodextrin Bonded Phase. *Mikrochim. Acta* **1992,** *107* (1-2), 73-80.

4. Sholl, D. S.; Gellman, A. J., Developing Chiral Surfaces for Enantioselective Chemical Processing. *AIChE Journal* **2009,** *55* (10), 2484-2490.

5. Smith, S. W., Chiral toxicology: it's the same thing...only different. *Toxicol. Sci.* **2009,** *110* (1), 4-30.

6. Erb, S., Single-enantiomer drugs poised for further market growth. *Pharm. Technol.* **2006,** *30*, s14-s18.

7. Baddeley, C. J., Fundamental investigations of enantioselective heterogeneous catalysis. *Top. Catal.* **2003,** *25* (1-4), 17-28.

8. Lorenzo, M. O.; Baddeley, C. J.; Muryn, C.; Raval, R., Extended surface chirality from supramolecular assemblies of adsorbed chiral molecules. *Nature* **2000,** *404* (6776), 376-379.

9. Barlow, S. M.; Raval, R., Complex organic molecules at metal surfaces: bonding, organisation and chirality. *Surface Science Reports* **2003,** *50* (6–8), 201-341.

10. Parschau, M.; Romer, S.; Ernst, K. H., Induction of homochirality in achiral enantiomorphous monolayers. *J. Am. Chem. Soc.* **2004,** *126* (47), 15398-15399.

11. McFadden, C. F.; Cremer, P. S.; Gellman, A. J., Adsorption of chiral alcohols on "chiral" metal surfaces. *Langmuir* **1996,** *12* (10), 2483-2487.

12. Gellman, A. J., Chiral Surfaces: Accomplishments and Challenges. *ACS Nano* **2010,** *4* (1), 5-10.

13. Horvath, J. D.; Gellman, A. J., Enantiospecific desorption of R- and S-propylene oxide from a chiral Cu(643) surface. *J. Am. Chem. Soc.* **2001,** *123* (32), 7953-7954.

14. Horvath, J. D.; Gellman, A. J., Enantiospecific desorption of chiral compounds from chiral Cu(643) and achiral Cu(111) surfaces. *J. Am. Chem. Soc.* **2002,** *124* (10), 2384-2392.

15. Cheong, W. Y.; Gellman, A. J., Energetics of Chiral Imprinting of Cu(100) by Lysine. *J. Phys. Chem. C* **2011,** *115* (4), 1031-1035.

16. Huang, Y.; Gellman, A. J., Enantiospecific Adsorption of (R)-3-Methylcyclohexanone on Naturally Chiral Surfaces Vicinal to Cu(110). *Top. Catal.* **2011,** *54* (19-20), 1403-1413.

17. Rampulla, D. M.; Francis, A. J.; Knight, K. S.; Gellman, A. J., Enantioselective surface chemistry of R-2-bromobutane on Cu(643)$^{(R\&S)}$ and Cu(531)$^{(R\&S)}$. *J. Phys. Chem. B* **2006,** *110* (21), 10411-10420.

18. Gellman, A. J.; Huang, Y.; Feng, X.; Pushkarev, V. V.; Holsclaw, B.; Mhatre, B. S., Superenantioselective Chiral Surface Explosions. *J. Am. Chem. Soc.* **2013,** *135* (51), 19208-19214.

19. Horvath, J. D.; Baker, L.; Gellman, A. J., Enantiospecific orientation of R-3-Methylcyclohexanone on the chiral Cu(643)(R/S) surfaces. *J. Phys. Chem. C* **2008,** *112* (20), 7637-7643.

20. Gladys, M. J.; Stevens, A. V.; Scott, N. R.; Jones, G.; Batchelor, D.; Held, G., Enantiospecific adsorption of alanine on the chiral Cu{531} surface. *J. Phys. Chem. C* **2007,** *111* (23), 8331-8336.

21. Attard, G. A.; Ahmadi, A.; Feliu, J.; Rodes, A.; Herrero, E.; Blais, S.; Jerkiewicz, G., Temperature effects in the enantiomeric electro-oxidation of D- and L-glucose on Pt{643}(S). *J. Phys. Chem. B* **1999,** *103* (9), 1381-1385.

22. Attard, G. A., Electrochemical studies of enantioselectivity at chiral metal surfaces. *J. Phys. Chem. B* **2001,** *105* (16), 3158-3167.

23. Horvath, J. D.; Koritnik, A.; Kamakoti, P.; Sholl, D. S.; Gellman, A. J., Enantioselective separation on a naturally chiral surface. *J. Am. Chem. Soc.* **2004,** *126* (45), 14988-14994.

24. Baber, A. E.; Gellman, A. J.; Sholl, D. S.; Sykes, E. C. H., The real structure of naturally chiral Cu{643}. *J. Phys. Chem. C* **2008,** *112* (30), 11086-11089.

25. Kuhnle, A.; Linderoth, T. R.; Besenbacher, F., Enantiospecific adsorption of cysteine at chiral kink sites on Au(110)-(1x2). *J. Am. Chem. Soc.* **2006,** *128* (4), 1076-1077.

26. Eralp, T.; Ievins, A.; Shavorskiy, A.; Jenkins, S. J.; Held, G., The importance of attractive three-point interaction in enantioselective surface chemistry: stereospecific adsorption of serine on the intrinsically chiral Cu{531} surface. *J. Am. Chem. Soc.* **2012,** *134* (23), 9615-21.

27. Held, G.; Gladys, M. J., The Chemistry of Intrinsically Chiral Surfaces. *Topics in Catalysis* **2008,** *48* (1-4), 128-136.

28. Schillinger, R.; Šljivančanin, Ž.; Hammer, B.; Greber, T., Probing Enantioselectivity with X-Ray Photoelectron Spectroscopy and Density Functional Theory. *Phys. Rev. Lett.* **2007,** *98* (13).

29. Hazen, R.; Sholl, D., Chiral selection on inorganic crystalline surfaces. *Nature* **2003,** *2*, 367-374.

30. Szabelski, P., Enantioseparation on a chiral nanostructured surface: Effect of molecular shape. *Physica A: Statistical Mechanics and its Applications* **2008,** *387* (18), 4615-4622.

31. Szabelski, P., Extended Surface Chirality for Enantiospecific Adsorption. *Chemistry - A European Journal* **2008,** *14* (27), 8312-8321.

32. Zaera, F., Chiral Modification of Solid Surfaces: A Molecular View. *Journal of Physical Chemistry C* **2008,** *112* (42), 16196-16203.

33. Horvath, J.; Gellman, A. J., Enantiospecific desorption of chiral compounds from chiral Cu(643) and achiral Cu(111) surfaces. *Journal of American Chemical Society* **2001,** *124* (10), 2384-2392.

34. Horvath, J.; Koritnik, A.; Kamakoti, P.; Sholl, D.; Gellman, A. J., Enantioselective Separation on a Naturally Chiral Surface. *Journal of American Chemical Society* **2004,** *126*, 14988-14994.

35. Horvath, J.; Baker, L.; Gellman, A. J., Enantiospecific Orientation of R-3-Methycyclohexanone on the Chiral Cu(643)R/S Surfaces. *J. Phys. Chem. C* **2008,** *112* (20), 7.

36. Huang, Y.; Gellman, A. J., Enantiospecific Adsorption of (R)-3-Methylcyclohexanone on Naturally Chiral Cu(531) R&S Surfaces. *Catalysis Letters* **2008,** *125* (3-4), 177-182.

37. Zhao, X., Fabricating Homochiral Facets on Cu(001) with l-lysine. *Journal of the American Chemical Society* **2000,** *122* (50), 12584-12585.

38. Bhatia, B.; Sholl, D. S., Characterization of enantiospecific chemisorption on chiral Cu surfaces vicinal to Cu(111) and Cu(100) using density functional theory. *The Journal of Chemical Physics* **2008,** *128* (14), 144709.

39. Han, J. W. DFT Studies for Separation of Enantiomers of a Chiral Species by Enantiospecific Adsorption on Solid Surfaces. Dissertation, Georgia Institute of Technology, Atlanta, 2010.

40. Han, J. W.; Sholl, D. S., Enantiospecific adsorption of amino acids on hydroxylated quartz (1010). *Physical Chemistry Chemical Physics* **2010,** *12* (28), 8024.

41. Rankin, R. Density Functional Theory Investigation of the Adsorption of Glycine and Alanine on the Cu(110), Cu(100), and Cu(3,1,17) Surfaces. Dissertation, Carnegie Mellon University, Pittsburgh, 2006.

42. Rankin, R.; Sholl, D., Structure of Dense Glycine and Alanine Adlayers on Chiral Cu(3,1,17) Surface. *Langmuir* **2006,** *22* (19), 8096-8103.

43. Grimme, S.; Huenerbein, R.; Ehrlich, S., On the Importance of the Dispersion Energy for the Thermodynamic Stability of Molecules. *ChemPhysChem* **2011,** *12* (7), 1258-1261.

44. Grimme, S., Accurate description of van der Waals complexes by density functional theory including empirical corrections. *Journal of Computational Chemistry* **2004,** *25* (12), 1463-1473.

45. Grimme, S., Semiempirical GGA-type density functional constructed with a long-range dispersion correction. *Journal of Computational Chemistry* **2006,** *27* (15), 1787-1799.

46. Dion, M.; Rydberg, H.; Schröder, E.; Langreth, D. C.; Lundqvist, B. I., Van der Waals Density Functional for General Geometries. *Physical Review Letters* **2004,** *92* (24).

47. Román-Pérez, G.; Soler, J., Efficient Implementation of a van der Waals Density Functional: Application to Double-Wall Carbon Nanotubes. *Physical Review Letters* **2009,** *103* (9).

48. Kang, J. H.; Toomes, R. L.; Polcik, M.; Kittel, M.; Hoeft, J. T.; Efstathiou, V.; Woodruff, D. P.; Bradshaw, A. M., Structural investigation of glycine on Cu(100) and comparison to glycine on Cu(110). *The Journal of Chemical Physics* **2003,** *118* (13), 6059.

49. Chen, Q.; Frankel, D.; Richardson, N., Chemisorption induced chirality: glycine on Cu{110}. *Surf Sci* **2001,** *497*, 37-46.

50. Toomes, R. L.; Kang, J. H.; Woodruff, D.; Polcik, M.; Kittel, M.; Hoeft, J. T., Can glycine form homochiral structural domains on low-index copper surfaces. *Surface Science Letters* **2003,** *522*, L9-L14.

51. Rankin, R.; Sholl, D., Assessment of heterochiral and homochiral glycine adlayers on Cu(110) using density functional theory. *Surf Sci* **2004,** *548* (1-3), 301-308.

52. Rankin, R.; Sholl, D., Structure of Glycine, Enantiopure Alanine, and Racemic Alanine Adlayers on Cu(110) and Cu(100) Surfaces. *Journal of Physical Chemistry B* **2005,** *109* (35), 16764-16773.

53. Rankin, R. B.; Sholl, D. S., First-principles studies of chiral step reconstructions of Cu(100) by adsorbed glycine and alanine. *The Journal of Chemical Physics* **2006,** *124* (7), 074703.

54. Rankin, R. B.; Sholl, D. S., Structure of enantiopure and racemic alanine adlayers on Cu(110). *Surf Sci* **2005,** *574* (1), L1-L8.

55. Efstathiou, V.; Woodruff, D. P., Characterisation of the interaction of glycine with Cu(100) and Cu(111). *Surf Sci* **2003,** *531* (3), 304-318.

56. Zhao, X.; Wang, H.; Zhao, R.; Yang, W., Self-assembly of amino acids on the Cu(001) surface. *Materials Science & Engineering C* **2001,** *16*, 41-50.

57. Barlow, S.; Louafi, S.; Leroux, D.; Williams, J.; Muryn, C.; Haq, S.; Raval, R., Polymorphism in supramolecular chiral structures of R- and S-alanine on Cu(110). *Surf Sci* **2005,** *590* (2-3), 243-263.

58. Haq, S.; Moslemzadeh, N.; Robin, A.; Barlow, S.; Raval, R., Racemic versus Enantiopure Alanine on Cu110: An Experimental Study. *Langmuir* **2007,** *23* (21), 10694-10700.

59. Iwai, H.; Egawa, C., Molecular Orientation and Intermolecular Interaction in Alanine on Cu(001). *Langmuir* **2010,** *26* (4), 2294-2300.

60. Zhao, X.; Zhao, R.; Yang, W., Adsorption of alanine on Cu(001) studied by scanning tunneling microscopy. *Surf Sci* **1999,** *442,* L995-L1000.

61. Zhao, X.; Perry, S. S., Ordered adsorption of ketones on Cu(643) revealed by scanning tunneling microscopy. *Journal of Molecular Catalysis A: Chemical* **2004,** *216* (2), 257-262.

62. Zhao, X.; Perry, S. S.; Horvath, J.; Gellman, A. J., Adsorbate induced kink formation in straight step edges on Cu(533) and Cu(221). *Surf Sci* **2004,** *563* (1-3), 217-224.

63. Fosser, K.; Nuzzo, R.; Bagus, P.; Woll, C., The Adsorption of Cyclopropane and Cyclohexane on Cu(111) : An Experimental and Theoretical Investigation on the Nature of the CH-Metal Interaction. *Angewandte Chemie International Edition* **2002,** *41* (10), 1735-1737.

64. Waugh, K. C., Methanol Synthesis. *Catalysis Today* **1992,** *15* (1), 51-75.

65. Rasmussen, P. B.; Holmblad, P. M.; Askgaard, T.; Ovesen, C. V.; Stoltze, P.; Nørskov, J. K.; Chorkendorff, I., Methanol synthesis on Cu(100) from a binary gas mixture of CO_2 and H_2. *Catalysis Letters* **1994,** *26* (3-4), 373-381.

66. Grabow, L. C.; Mavrikakis, M., Mechanism of Methanol Synthesis on Cu through CO_2 and CO Hydrogenation. *ACS Catalysis* **2011,** *1* (4), 365-384.

67. Behrens, M.; Studt, F.; Kasatkin, I.; Kühl, S.; Hävecker, M.; Abild-Pedersen, F.; Zander, S.; Girgsdies, F.; Kurr, P.; Kniep, B.-L.; Tovar, M.; Fischer, R. W.; Nørskov, J. K.; Schlögl, R., The Active Site of Methanol Synthesis over Cu/ZnO/Al_2O_3 Industrial Catalysts. *Science* **2012,** *336* (6083), 893-897.

68. Pan, W.; Song, C., In-Situ Study of Carbon Deposition during CO_2 Reforming of Methane for Synthesis Gas Production, Using the Tapered Element Oscillation Microbalance. In *Carbon Dioxide as Chemical Feedstock*, Wiley-VCH Verlag GmbH & Co. KGaA: 2010; pp 249-266.

69. Ballivet-Tkatchenko, D.; Dibenedetto, A., Synthesis of Linear and Cyclic Carbonates. In *Carbon Dioxide as Chemical Feedstock*, Wiley-VCH Verlag GmbH & Co. KGaA: 2010; pp 169-212.

70. Aresta, M., Carbon Dioxide: Utilization Options to Reduce its Accumulation in the Atmosphere. In *Carbon Dioxide as Chemical Feedstock*, Wiley-VCH Verlag GmbH & Co. KGaA: 2010; pp 1-13.

71. Yang, Y.; Evans, J.; Rodriguez, J. A.; White, M. G.; Liu, P., Fundamental studies of methanol synthesis from CO2 hydrogenation on Cu(111), Cu clusters, and Cu/ZnO(0001). *Physical Chemistry Chemical Physics* **2010,** *12* (33), 9909.

72. Yoshihara, J.; Campbell, C. T., Methanol synthesis and reverse water-gas shift kinetics over Cu(110) model catalysts: Structural sensitivity. *Journal of Catalysis* **1996,** *161* (2), 776-782.

73. Greeley, J.; Mavrikakis, M., Methanol Decomposition on Cu(111): A DFT Study. *Journal of Catalysis* **2002,** *208* (2), 291-300.

CHAPTER 2

COMPUTATIONAL METHODOLOGY

Density functional theory (DFT) is a common quantum mechanical modeling method used to examine electronic structure in many-body systems. A detailed introduction and discussion of DFT can be found in a series of books and reviews,[1-10] so this chapter only provided a brief overview of DFT as it was used in my work.

The basis of DFT traced back to the Schrödinger equation published by Erwin Schrodinger in 1926.[11] While the Schrödinger equation, in theory, should be able to describe any system, in practice, an exact analytical solution can only be found for simple systems. This became obvious when one examines the expanded form of the simplified Schrödinger's equation, $H\Psi = E\Psi$:

$$\left[-\frac{\hbar^2}{2m}\sum_{i=1}^{N}\nabla_i^2 + \sum_{i=1}^{N}V\left(\vec{r}_i\right) + \sum_{i=1}^{N}\sum_{j<i}U\left(\vec{r}_i, \vec{r}_j\right)\right]\Psi = E\Psi \tag{2.1}$$

The three terms within the brackets describe the kinetic energy of each electron, the interaction energy of each electron and the atomic nuclei, and the interaction between different electrons, respectively. In order to solve for the individual electron wave function, one must simultaneously considers the interaction of this individual electron wave function with all other electrons. It was this interaction between different electrons that made it difficult to obtain an exact analytical solution for a system of any meaningful size. Thus, the desire to investigate the electronic structure of many-body systems and the growth of computational capability had pushed for the development of numerical method approximation to the Schrodinger equation.

The entire DFT field came from two mathematical theorems proved by Hohenberg and Kohn[12] and the subsequent development by Kohn and Sham.[13] First, Hohenberg-Kohn showed that there is a one-to-one mapping between the ground state wave function and the ground state electron density. This significantly reduced the dimension of the Schrödinger equation from 3N to just 3. Secondly, Hohenberg-Kohn stated that the minimized energy of the electron density's overall functional is the true electron density found in the full solution of the Schrödinger equation. Following the Hohenberg-Kohn theorems, Kohn and Sham showed that the many-body interacting electrons can be described by a set of non-interacting, self-consistent, and single particle equations which came to known as the Kohn-Sham equations:

$$\left[-\frac{\hbar^2}{2m}\nabla^2 + V(\vec{r}) + V_H(\vec{r}) + V_{xc}(\vec{r})\right]\Psi_i(\vec{r}) = \varepsilon_i\Psi_i(\vec{r}) \qquad (2.2)$$

The four components within the brackets of the Kohn-Sham equations are kinetic energy, the electron-nuclei interaction energy, the Hartree potential, and the exchange-correlation contribution, respectively. While the first three components can be solved in exact analytical form, the exchange-correlation contribution is unknown. Thus, there existed a series of approximation methods that attempts to describe the exchange-correlation contribution. There are two widely used approaches to approximate the exchange-correlation contribution within the solid material field: the local density approximation (LDA) and the general gradient approximation (GGA). The LDA assumes that each electron in the actual system can be accurately modeled as the same electron in a uniform electron gas with the same global density. The GGA takes a step further and includes a correction for the local gradients in the electron density. This is often seen as an improvement over the LDA approach. Among GGA functionals, the Perdew-Burke-Ernzerhof (PBE-GGA) functional is widely used for its simplification of the exchange-correlation functional, which addressed the shortcoming of the Perdew-Wang 1991 (PW91-GGA) functional.[14-15] However, nonhybrid GGA failed to describe long-range van der Waals forces.[16]

There are three main approaches to correct for the long-range van der Waals interaction: C_6 based correction,[17] density based correction,[18] and effective one-electron potential.[19] Within the C_6 based methods, Grimme et al. proposed the D2 functional to empirically account for dispersion forces within DFT,[20-21]

$$E_{DFT-D} = E_{DFT} + E_{disp} \tag{2.3}$$

with,

$$E_{disp} = -s_6 \sum_{i=1}^{N-1} \sum_{j=i+1}^{N} \frac{C_6^{ij}}{R_{ij}^6} f_{dmp}(R_{ij}) \tag{2.4}$$

Here, s_6 is a global scaling factor, C_6^{ij} is the dispersion coefficient for individual atomic pairs, R is the distance between the two atoms, and $f_{dmp}(R_{ij})$ is a damping function that avoid near-singularities for small values of R. s_6 was determined by empirically fitting binding energies and intermolecular distances to a test set of system, and C_6^{ij} was obtained through mixing of individual atom's C_6 parameter.[20-21]

Within the density based approach, Becke proposed a dispersion correction method using the LDA.[18,22] The optimized B86b[51,52] model accounted for the inhomogeneous electron densities, ρ_σ, using,[23-24]

$$E_x^{SE} = E_X^{LDA} - \beta \sum_{\sigma} \int \rho_\sigma^{4/3} \frac{x_\sigma^2}{(1 + \gamma x_\sigma^2)} d^3r \tag{2.5}$$

where E_x^{SE} is the semi-empirical exchange energy, E_X^{LDA} is the LDA exchange energy, and $x_\sigma = |\nabla\rho_\sigma|/\rho_\sigma^{4/3}$. However, at the asymptotic limit, the optB86b did not converge to the correct values. The proposed optimized B88 shown below attempted to address this issue,[25]

$$E_X = E_X^{LDA} - \beta \sum_{\sigma} \int \rho_\sigma^{4/3} \frac{x_\sigma^2}{(1 + 6\beta x_\sigma \sinh^{-1} x_\sigma)} d^3r \tag{2.6}$$

Klimeš incorporated these methods into the *Vienna Ab-initio Simulation Package* (VASP) as the optB86b and optB88 vdW-DF correction.[26] Based on overall performance against the S22 dataset and metal crystal structures, the optB88 functional yielded the most precise results among revPBE, optPBE, optB86b, optB88, LDA, PBE, and other functionals.[26-27]

In this thesis, we implemented DFT calculations using VASP.[28-31] The electron–electron exchange and correlation interactions were described with a GGA functional. Core–electron interactions were modeled with the projector augmented-wave (PAW) potential.[32-33] Additional details of the specific DFT calculation are provided in the respective chapter.

Reference

1. Parr, R. G.; Yang, W., *Density-Functional Theory of Atoms and Molecules*. Oxford University Press, USA: 1989.

2. Payne, M. C.; Teter, M. P.; Allan, D. C.; Arias, T. A.; Joannopoulos, J. D., Iterative minimization techniques for *ab initio* total-energy calculations: molecular dynamics and conjugate gradients. *Reviews of Modern Physics* **1992,** *64* (4), 1045-1097.

3. Politzer, P.; Seminario, J. M., *Modern Density Functional Theory: A Tool For Chemistry: A Tool For Chemistry*. Elsevier Science: 1995.

4. Hammer, B.; Norskov, J. K., Theoretical surface science and catalysis - Calculations and concepts. In *Advances in Catalysis, Vol 45: Impact of Surface Science on Catalysis*, Gates, B. C.; Knozinger, H., Eds. Elsevier Academic Press Inc: San Diego, 2000; Vol. 45, pp 71-129.

5. Koch, W.; Holthausen, M. C., *A chemist's guide to density functional theory*. Wiley-VCH: 2000.

6. Greeley, J.; Norskov, J. K.; Mavrikakis, M., Electronic structure and catalysis on metal surfaces. *Annu. Rev. Phys. Chem.* **2002,** *53*, 319-348.

7. Fiolhais, C.; Nogueira, F.; Marques, M. A. L., *A Primer in Density Functional Theory*. Springer: 2003.

8. Capelle, K., *A bird's-eye view of density-functional theory*. Departamento de Física e Informática, Instituto de Física de São Carlos-USP: 2004.

9. Martin, R. M., *Electronic Structure: Basic Theory and Practical Methods*. Cambridge University Press: 2004.

10. Sholl, D.; Steckel, J., *Density functional theory : a practical introduction*. John Wiley & Sons: Hoboken, 2009.

11. Schrödinger, E., An Undulatory Theory of the Mechanics of Atoms and Molecules. *Physical Review* **1926,** *28* (6), 1049-1070.

12. Hohenberg, P.; Kohn, W., Inhomogeneous Electron Gas. *Physical Review* **1964,** *136* (3B), B864-B871.

13. Kohn, W.; Sham, L. J., Self-Consistent Equations Including Exchange and Correlation Effects. *Physical Review* **1965,** *140* (4A), A1133-A1138.

14. Perdew, J. P.; Chevary, J. A.; Vosko, S. H.; Jackson, K. A.; Pederson, M. R.; Singh, D. J.; Fiolhais, C., Atoms, molecules, solids, and surfaces: Applications of the

generalized gradient approximation for exchange and correlation. *Physical Review B* **1992,** *46* (11), 6671-6687.

15. Perdew, J.; Burke, K.; Ernzerhof, M., Generalized Gradient Approximation Made Simple. *Physical Review Letters* **1996,** *77* (18), 3865-3868.

16. Grimme, S.; Huenerbein, R.; Ehrlich, S., On the Importance of the Dispersion Energy for the Thermodynamic Stability of Molecules. *ChemPhysChem* **2011,** *12* (7), 1258-1261.

17. Grimme, S.; Antony, J.; Ehrlich, S.; Krieg, H., A consistent and accurate ab initio parametrization of density functional dispersion correction (DFT-D) for the 94 elements H-Pu. *The Journal of Chemical Physics* **2010,** *132* (15), 154104.

18. Dion, M.; Rydberg, H.; Schröder, E.; Langreth, D. C.; Lundqvist, B. I., Van der Waals Density Functional for General Geometries. *Physical Review Letters* **2004,** *92* (24).

19. von Lilienfeld, O. A.; Tavernelli, I.; Rothlisberger, U.; Sebastiani, D., Optimization of Effective Atom Centered Potentials for London Dispersion Forces in Density Functional Theory. *Physical Review Letters* **2004,** *93* (15), 153004.

20. Grimme, S., Accurate description of van der Waals complexes by density functional theory including empirical corrections. *Journal of Computational Chemistry* **2004,** *25* (12), 1463-1473.

21. Grimme, S., Semiempirical GGA-type density functional constructed with a long-range dispersion correction. *Journal of Computational Chemistry* **2006,** *27* (15), 1787-1799.

22. Román-Pérez, G.; Soler, J., Efficient Implementation of a van der Waals Density Functional: Application to Double-Wall Carbon Nanotubes. *Physical Review Letters* **2009,** *103* (9).

23. Becke, A. D., On the large-gradient behavior of the density functional exchange energy. *The Journal of Chemical Physics* **1986,** *85* (12), 7184.

24. Becke, A. D., Density functional calculations of molecular bond energies. *The Journal of Chemical Physics* **1986,** *84* (8), 4524.

25. Becke, A. D., Density-functional exchange-energy approximation with correct asymptotic behavior. *Physical Review A* **1988,** *38* (6), 3098-3100.

26. Klimeš, J.; Bowler, D.; Michaelides, A., Van der Waals density functionals applied to solids. *Physical Review B* **2011,** *83* (19).

27. Klimeš, J.; Bowler, D. R.; Michaelides, A., Chemical accuracy for the van der Waals density functional. *Journal of Physics: Condensed Matter* **2010,** *22* (2), 022201.

28. Kresse, G.; Hafner, J., Ab initio molecular-dynamics for liquid-metals. *Physical Review B* **1993,** *47* (1), 558-561.

29. Kresse, G.; Hafner, J., Ab initio molecular-dynamics simulation of the liquid-metal–amorphous-semiconductor transition in germanium. *Physical Review B* **1994,** *49* (20), 14251-14269.

30. Kresse, G.; Furthmuller, J., Efficiency of ab-initio total energy calculations for metals and semiconductors using a plane-wave basis set. *Comput. Mater. Sci.* **1996,** *6* (1), 15-50.

31. Kresse, G.; Furthmuller, J., Efficient iterative schemes for ab initio total-energy calculations using a plane-wave basis set. *Physical Review B* **1996,** *54* (16), 11169-11186.

32. Blochl, P. E., Projector Augmented-Wave Method. *Physical Review B* **1994,** *50* (24), 17953-17979.

33. Kresse, G.; Joubert, D., From ultrasoft pseudopotentials to the projector augmented-wave method. *Physical Review B* **1999,** *59* (3), 1758-1775.

CHAPTER 3

CHEMISORPTION OF GLYCINE AND ALANINE ON COPPER SURFACES

3.1 Introduction*

An interesting aspect of biological life on Earth is the homochirality of biomolecules such as amino acids, sugars, proteins, and DNA.[1-2] One of the consequences of this homochirality in living organisms is that enantiomers of a chiral molecule can exhibit significantly different physiological effects.[3-5] The resulting demand for enantiomerically pure molecules has created a >$200B/yr market.[6] As a result, enantioselective chemical processes have attracted a great deal of attention in the biochemical and pharmaceutical industries. As one approach to enantioselectivity, chiral surfaces are attractive media for chiral separations and for enantioselective heterogeneous catalysis. Before this can be achieved, we must gain an improved understanding of the interactions between adsorbed species and the metal surfaces.

3.1.1 Dense Ordered Adlayer of Glycine and Alanine on Cu(110)

Previous work has shown that DFT based simulations can accurately predict experimental results when surface adsorption is not dominated by van der Waals forces. However, the lack of consideration of van der Waals forces limited the potential application of DFT based simulations. With the recent development of dispersion

---

* Published as Y. Yun, D. Wei, D. Sholl, and A. Gellman, *J. Phys. Chem. C.*, **2014**, *118* (27), pp 14957-14966

corrected methods which attempted to address this weakness, we examined the impact of these methods on non-van der Waals forces dominated adsorption. Glycine, the simplest amino acid, is achiral in the gas phase, but it adopts chiral characteristics when adsorbed onto a flat surface.[7-9] Initial experiments were in apparent disagreement on the structure of dense glycine adlayers on Cu(110).[8-9] Chen et al. concluded heterochiral and homochiral domains coexisted from low-energy electron diffraction (LEED) and scanning tunneling microscope (STM) images,[10] but Toomes et al. concluded from X-ray photoelectron diffraction (XPD) measurements that only one domain exists.[9] To address this inconsistency, Rankin and Sholl investigated the structure of glycine and alanine, the simplest chiral amino acid, on atomically flat Cu surfaces using DFT.[11-16] These calculations showed a slight preference for the heterochiral footprint domain for glycine on Cu(110), and this domain was in quantitative agreement with the results obtained by Toomes et al. Furthermore, there were no observable differences between adsorption of D- and L- alanine on Cu surfaces, indicating the enantiomers are unlikely to separate into enantiospecific domains. This was also in agreement with experimental results.[17-20] The ordered structures formed by glycine and alanine on these surface greatly aided the use of DFT based calculations to examine these adsorbates. To quantify the overall effect of van der Waals forces on these chemisorbed molecules, we first re-examined these structures with dispersion corrected method calculations.

3.1.2 Adsorption of Enantiopure and Racemic Alanine on Cu(3,1,17)

Recently, Yun et al. reported the first unequivocal observation of the enantioselective separation of a racemic mixture on a naturally chiral metal surface.[21] The equilibrium adsorption of a gas phase, racemic mixture of D- and L-aspartic acid on naturally chiral Cu(3,1,17)$^{R\&S}$ surfaces resulted in ~39% surface enantiomeric excess in the adsorbed phase, favoring adsorption of D-aspartic acid over L-aspartic acid on the Cu(3,1,17)^{S} and vice versa on the Cu(3,1,17)^{R}. Adsorption of alanine on Cu surfaces has been extensively studied as a model system for understanding the surface chemistry of chiral biomolecules such as amino acids on metal surfaces. Previous studies using reflection absorption infrared spectroscopy (RAIRS) have shown that alanine adsorbs on Cu surfaces in its anionic form (CH_3-CH(NH_2)-COO).[22-24] LEED, near edge X-ray absorption fine structure spectroscopy (NEXAFS), and STM have been used to show that enantiomerically pure D- and L-alanine adsorbed on the naturally chiral Cu(531)^{R} surface exhibit enantiospecific differences in their adsorption geometries and long-range order.[25-26] Furthermore, Clegg et al. showed that adsorption of D- and L-alanine leads to reconstruction of naturally chiral Cu(531)^{S} surface that created enantiospecifically different surface orientations.[27] The greater goal of this type of work is to understand the origin of the enantiospecific differences in the energetics of chiral adsorbates on chiral surfaces. However, the direct quantitative measurement of enantiospecific energy differences of chiral adsorbates on chiral surfaces is experimentally challenging. In spite of the extensive studies of alanine on chiral Cu surfaces, enantioselectivity has been predicted only on the basis of computational modeling.[28-29] Later in this chapter, we attempt to describe the equilibrium adsorption of D- and L-Alanine mixtures on naturally chiral Cu(3,1,17) surfaces through computational simulation and direct measurement. The combined experimental and computational studies provided insight into the enantioselectivity of chiral amino acid adsorption on naturally chiral surfaces.

3.2 Methodology

3.2.1 Density Functional Theory for Glycine/Alanine on Cu(110) and Alanine on $Cu(3,1,17)^S$

Computational simulations were carried out using periodic DFT calculations with the Vienna Ab initio Simulation Package (VASP).[30-33] The PBE-GGA functional was used to describe the electron–electron exchange and correlation.[34-35] Core–electron interactions were modeled with the projector augmented-wave (PAW) potential.[36-37] All calculations used a plane wave expansion cutoff of 500 eV. Structural optimization was performed by a conjugate gradient algorithm with a force stopping criterion of 0.03 eV/Å. The effects of long range dispersion forces was included through Grimme's D2 dispersion correction method.[38] The interatomic spacing of Cu was obtained through modeling of bulk FCC Cu atoms with a supercell containing 8 Cu atoms in an FCC lattice using $16\times16\times16$ k-points. All surface slabs were 7 Å thick with the bottommost 3 Å immobilized in their bulk positions. All surface calculations used a Monkhorst-Pack grid of $4\times4\times1$ k-points. All surface slabs were created with a vacuum spacing of at least 10 Å. Both glycine and alanine adsorbed in the deprotonated form with a tridentate footprint.[15, 17, 19-20, 39-42] A dense adlayer was defined as two alanines coadsorbed on the Cu(110) surface unit cell.

The Cu(110) slab were made up of p(2 × 4) surface unit cells. The surface geometries of the dense glycine and alanine adlayer were obtained from earlier work conducted by Rankin and Sholl.[11-12, 14] The construction of a $Cu(3,1,17)^S$ slab was similar to earlier work by Rankin and Sholl.[43] The surface consisted of a single $Cu(3,1,17)^S$ surface unit cell. To ensure a systematic examination of the surface, the study modified the n_A_x denotation of the adlayer defined by Rankin and Sholl to be m_n_A_3.[43] Here, m denotes whether the adlayer was enantiopure (L-/D-) or racemic (DL-) alanine. The surface geometries for each dense L-Alanine adlayers and dense DL-Alanine adlayers were generated from the most favorable configurations found by Rankin and Sholl.[43] The configurations for dense D-Alanine adlayers were created by taking the earlier configurations and modifying the methyl group position as needed.

Since both glycine and alanine adsorbed in a deprotonated form, the calculation is balanced with glycine or alanine and ½ H_2 in vacuum. An isolated glycine, alanine, or H_2 molecule in a 20 × 20 × 20 Å cell sampled at the Γ point was used as the reference. The adsorption energy was defined as,

$$\Delta E_{Adsorption} = E_{total} - E_{\text{isolated}} - E_{Surface} \tag{3.2}$$

where E_{total}, E_{isolated}, $E_{Surface}$ are the total energy of the relaxed structure including the adsorbed molecule, the energy of the isolated molecule, and the clean surface energy, respectively. On the Cu(3,1,17) surface, a dense adlayer was defined as two alanine coadsorbed on one surface unit cell.

3.2.2 TPD experiment for dense alanine on Cu(3,1,17)•

Study of enantioselective adsorption of D- and L-alanine on Cu(3,1,17)[R&S] surfaces was performed in an ultrahigh vacuum surface analysis chamber with a base pressure of 2 × 10^{-10} Torr. The chamber is equipped with an Ar^+ ion sputter gun to clean the sample, LEED optics to examine the ordering of clean surfaces, a homemade evaporator to deposit alanine on the Cu single crystal surfaces, and an Extrel mass

---

• Experimental results reported in this chapter were obtained by Dr. Gellman's group at Carnegie Mellon University spectrometer to detect chemical species in the gas phase and those desorbing from the surface.

The Cu(3,1,17) single crystal sample (Monocrystals Company) was approximately 10 mm in diameter and 2 mm thick. The Cu single crystal disk exposed the $Cu(3,1,17)^R$ surface on one side and the $Cu(3,1,17)^S$ surface on the other side. The temperature of the sample was controlled within the range 90 - 1000 K by resistive heating and liquid nitrogen cooling and was measured using a chromel-alumel thermocouple spot welded to its edge. The temperature was controlled by a computer monitoring the temperature and varying the heating current. The Cu sample was cleaned by repeated cycles of 1 keV Ar^+ ion sputtering while annealing at 850 K for 500 seconds. In the final step of the sputtering-annealing procedure, the sample was cooled at a controlled rate of -1 K/sec at a pressure of $<1\times10^{-9}$ Torr in order to obtain a well-ordered surface structure. The long range order of the clean $Cu(3,1,17)^{R\&S}$ surfaces was verified by LEED before adsorption of alanine.

Unlabeled D-alanine (Alfa Aesar, 99% chemical and optical purity) and isotopically labeled L-alanine ($HO_2{}^{13}CCH(NH_2)CH_3$, Cambridge Isotope Laboratories, 98% chemical purity, 99 atom%) were vapor deposited onto the $Cu(3,1,17)^{R\&S}$ surfaces by sublimation from a homemade Knudsen cell evaporator with two glass vials; one for each enantiomer. The glass vials were wrapped with resistance heating wires and their temperatures were measured by thermocouples bonded to their exteriors. The fluxes of D- and L-alanine from each vial were controlled independently by heating the vials to different temperatures. The time of exposure of the $Cu(3,1,17)^{R\&S}$ surfaces to the D- and L-alanine vapors was controlled by opening and closing a shutter placed in front of the glass vials. After exposure to alanine, the sample was position in front of the aperture to the mass spectrometer and then heated at 1 K/sec to conduct temperature programmed reaction spectroscopy of the adsorbed species. The relative coverages of D- and L-Alanine on the Cu(3,1,17)$^{R\&S}$ surfaces were determined by monitoring the signals for CO_2 (m/q = 44) and $^{13}CO_2$ (m/q = 45) with the mass spectrometer while heating the surfaces from 250 to 670 K at 1 K/s.

3.3 Results and Discussion

3.3.1 Dense Ordered Adlayer of Glycine and Alanine on Cu(110)

Our work briefly examined the overall effect of dispersion corrected methods on these systems. Working from the adsorption geometries determined by Rankin and Sholl,[11] we applied the DFT-D2 dispersion correction to estimate its effect on glycine and alanine adlayers on Cu(110). Since glycine is achiral, the heterochiral and homochiral labels denote their footprint on the surface. Table 3.1 lists the tabulated adsorption energy (AE) using the PBE-GGA and PBE-D2 functional. The D2 contribution was calculated as,

$$D2_{Contribution} = \frac{AE_{PBE-D2} - AE_{PBE-GGA}}{AE_{PBE-D2}} \qquad (3.3)$$

where $AE_{PBE-GGA}$ and AE_{PBE-D2} are the adsorption energies obtained using the PBE-GGA and PBE-D2 functional, respectively. As seen in Table 3.1, the inclusion of van der Waals interactions increased adsorption energy by 29-35%. This was consistent with the expectation that van der Waals forces contributed significantly to the total adsorption energy. However, the contributions were approximately consistent among structures of similar configuration and surface coverages.

Table 3.1: Tabulated effect of D2 correction on dense glycine/alanine adlayers.

System	$AE_{PBE-GGA}$ (eV)	AE_{PBE-D2} (eV)	$D2_{Contribution}$
Heterochiral Glycine	-1.78	-2.49	29%
Homochiral Glycine	-1.74	-2.49	30%
Enantiopure L-Alanine	-1.60	-2.43	34%
Racemate Alanine	-1.60	-2.45	35%

In the alanine adlayer, the similar enantiopure and racemate adsorption energies for both PBE-GGA and PBE-D2 functional suggested the racemate alanine domain will not separate into L- and D- enantiopure domains. This is consistent with previous calculations and experimental measurements.[14, 17] Since both glycine and alanine are chemisorbed on Cu(110), we did not expect the van der Waals forces to dominate the adsorption energy. The ~30% and ~35% dispersion force contribution to adsorption energy for adsorbed glycine and alanine, respectively, corroborated this expectation. The large binding energies seen for these species indicate that molecular decomposition is likely to occur before desorption of intact molecules can occur, consistent with our TPS experiments.

For glycine on Cu(110), the PBE-GGA results showed a minor preference for the heterochiral footprint, but this difference disappeared when dispersion corrected method was applied. This suggested the coexistence of both heterochiral and homochiral domains on the surface as proposed by Chen et al.[8] Since the early work by Rankin and Sholl[11] inferred a mismatch between the homochiral domain and the XPD data observed by Toomes et al.,[9] we compared the calculated N and O offsets as seen by the PBE-D2 functional in Table 3.2.

Table 3.2: Calculated and observed N and O offset distances (in Å) of adsorbed glycine relative to the closest surface Cu atom.

		Rankin and Sholl[11]		Dispersion Corrected	
	XPD[9]	Heterochiral	Homochiral	Heterochiral	Homochiral
N offsets at <-110>	0.24 ±0.10	0.20	0.17	0.16	0.17
			0.20	0.19	0.19
O offsets at <001>	0.68 ±0.09	0.70	0.76	0.63	0.63
			0.87	0.77	0.80
	0.97 ±0.08	0.98	0.23	1.12	1.12
			1.10	1.16	1.18

In the XPD experiments, Toomes et al. saw a single N offset distance and two O offset distances. The work by Rankin and Sholl indicated one N offset and two O offset distances for the heterochiral domain, and two N offset and four O offset distances for the homochiral domain. Based on these results, Rankin and Sholl inferred the homochiral footprint was inconsistent with the XPD data. However, DFT calculations with PBE-D2 method suggested that the homochiral footprint was not inconsistent with the experimental measurements. Unlike the earlier calculation where an O offset of 0.23 Å was observed for the homochiral domain, calculations with the PBE-D2 method observed N and O offsets that were consistent with the XPS study for both the heterochiral and homochiral domain. This suggested, contrary to earlier studies that neglected dispersion interactions, that both heterochiral domain and homochiral domain can coexist on Cu(110).

3.3.2 Adsorption of Enantiopure and Racemic Alanine on Cu(3,1,17)

The energetics of alanine adsorption on the $Cu(3,1,17)^S$ surfaces were calculated using DFT based simulation. These calculations used the PW91-GGA functional, the

PBE-GGA functional, and the PBE-D2 functional. Preliminary calculations had shown that PW91-GGA and PBE-GGA did not produce significant changes to energy differences between the different dense adlayers. This was important as the D2 dispersion correction used here was available only for the PBE-GGA functional rather than PW91-GGA functional. Comparison of the earlier PW91-GGA and the PBE-D2 results are found in Table 3.3. Both the PW91-GGA and the PBE-D2 functionals predicted the same configuration to have the lowest energy and roughly the same ordering of energies among higher energy configurations. This was consistent with the expectation that the total adsorption energy for these molecules is affected by dispersion contributions but that these contributions are approximately equal for a large variety of adsorbate configurations at similar coverages. Since there were no significant changes to the ordering of energies among these configurations, it is unlikely for the other configurations examined by Rankin and Sholl to be more favorable than the configurations already identified.[43]

Table 3.3: Relative energies of dense alanine adlayers on Cu(3,1,17)^S. All reported energies are referenced to the most stable adlayer (L_1_0_a).

Dense Adlayer PW91-GGA[43]	E (eV/unit cell)	Dense Adlayer PBE-D2	E (eV/unit cell)
L_1_0_a	0.00	L_1_0_a	0.00
DL_1_0_a	0.09	DL_1_0_a	-0.01
L_1_90_a	0.11	L_1_90_a	0.03
L_2_180_a	0.13	DL_2_180_a	0.22
DL_2_90_b	0.14	D_1_0_a	0.23
L_2_270_a	0.16	D_2_180_a	0.24
DL_1_90_b	0.20	L_2_180_a	0.25
DL_2_180_a	0.22	DL_2_90_b	0.28
L_4_270_b	0.24	DL_1_90_b	0.30
DL_2_270_a	0.26	L_2_270_a	0.30
DL_4_270_b	0.26	D_1_90_a	0.35
DL_1_90_a	0.27	D_1_90_b	0.37
L_1_90_b	0.30	D_2_90_b	0.39
L_2_90_b	0.40	D_2_270_a	0.40

These calculations modeled the energetics of two enantiopure phases (D-Alanine and L-Alanine) and a racemate phase (DL-Alanine). On the chiral Cu(3,1,17)$^{R\&S}$ surfaces, the adsorption energies of the enantiopure phases differ by $\Delta\Delta E_{DL} = \Delta E_{D/R} - \Delta E_{L/R} = \Delta E_{L/S} - \Delta E_{D/S}$. The adsorption energetics of the racemate phases are identical on the two surfaces, $\Delta E_{DL/R} = \Delta E_{DL/S}$, but they differ from the average energy of the enantiopure phases by $\Delta\Delta E_{r-c} = \Delta E_{DL/R} - \frac{1}{2}\left(\Delta E_{D/R} + \Delta E_{L/R}\right)$. Figure 3.1 shows the most stable configurations of D-, L-, and DL-Alanine on Cu(3,1,17)^S identified using DFT and the associated energies referenced to the most stable phase, L-alanine/Cu(3,1,17)^S. An interesting result of the calculations is that they predicted the energetics of the enantiopure L-alanine on Cu(3,1,17)^S to be comparable to the racemate phase. This indicated that both phases should be considered during the adsorption of alanine.

L-alanine/Cu(3,1,17)^S 0 eV/adsorbate | DL-alanine/Cu(3,1,17)^S -0.005 eV/adsorbate | D-alanine/Cu(3,1,17)^S 0.11 eV/adsorbate

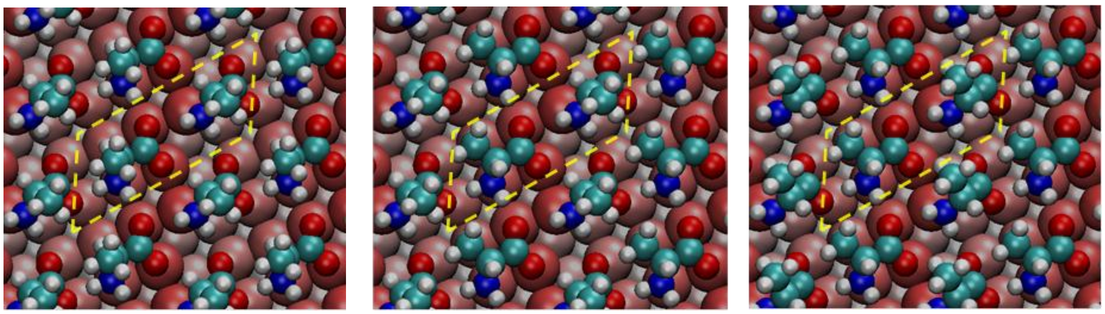

Figure 3.1: Structures and relative energies predicted using DFT-D2 for the most stable conformations of L-alanine, DL-alanine and D-alanine on the Cu(3,1,17)^S. The energies are defined relative to the that of L-alanine/Cu(3,1,17)^S. The unit cell contains two adsorbed molecules. In the case of the racemate DL-alanine overlayer the D-alanine enantiomer is adsorbed at the top of the step and extends onto the terrace, while the L-alanine enantiomer is adsorbed at the bottom of the step with the $–NH_2$ interacting with the least coordinated Cu atom in the step edge.

Inspection of the structures of the adsorbed overlayers of D- and L-alanine on the Cu(3,1,17)^S surface showed that there was a single motif for the two adsorbates in each unit cell that was dictated by the binding of the $–CO_2$ and $–NH_2$ groups to the surface and is independent of chirality. The unit cells drawn into the structures shown in Figure 3.1 have been chosen to highlight the two alanine adsorbates within the unit cell. In all three structures, the alanine at the upper right of the unit cell was adsorbed at the bottom of the step edge with its $–CO_2$ group binding to two nearest neighbor Cu atoms in the Cu(100) terrace and$–NH_2$ binding to the least coordinated Cu atom along the step edge. The alanine in the lower left of the unit cell in all three structures has the $–CO_2$ group binding to two nearest neighbor Cu atoms at the top of the step edge and the $–NH_2$ binding to a Cu atom in the Cu(100) terrace. The enantiospecific differences in the adsorption energetics of the two enantiopure phases and the racemate phase are dictated by stereospecific orientations of the –H and $–CH_3$ groups on the C_α atom. The enantiopure L-alanine phase has the lower of the energies of the enantiopure phases and adopts a structure in which both of the $–CH_3$ groups are oriented away from the surface. Going from the L-alanine phase to the racemate DL-alanine phase, the adsorbate on the terrace is reversed in chirality from L-alanine to D-alanine and has its $–CH_3$ interacting with the Cu(100) terrace. The DL-alanine phase was very slightly more stable (-0.005 eV/molecule) than the L -alanine phase. Going from the DL-alanine phase to the D-alanine phase, the chirality of the molecule at the bottom of the step edge was reversed. This has a much larger impact on the adsorption energy than reorientation of the $–CH_3$ group in the alanine on the terrace and destabilizes the D-alanine phase with respect to the L-alanine and the DL-alanine phases by ~0.11 eV/molecule.

DFT predicted a number of common features of the enantiopure and racemate structures of D- and L-alanine on $Cu(3,1,17)^S$. However, it also predicted that the subtle differences in structures induced by the reversal of the chirality are accompanied by adsorption energy differences of ~0.11 eV/molecule. As discuss below, these predictions are at odds with experimental observations.

3.3.3 LEED patterns of the clean $Cu(3,1,17)^{R\&S}$ surfaces*

The chirality of the $Cu(3,1,17)^{R\&S}$ surface structures was verified experimentally using LEED. Figure 3.2 shows the ideal structures of the $Cu(3,1,17)^{R\&S}$ surfaces in the top panels and the LEED patterns obtained from the clean $Cu(3,1,17)^{R\&S}$ surfaces in the lower panels. The ideal atomic structures of the $Cu(3,1,17)^{R\&S}$ surfaces have monoatomic kinked steps formed by (110) and (111) microfacets, and separated by (100) terraces.

* Results reported in this section were obtained by Dr. Gellman's group at Carnegie Mellon University

Although it is known that the real structures of such high Miller index surfaces are subject to thermal roughening,[44-46] STM imaging of Cu(643)^{R} and Cu(531)^{S} surfaces have shown that the net chirality of the surfaces is preserved.[47-48] Although thermal roughening of the steps results in the coalescence of kinks and loss of the periodic distribution of kinks along the step edge, the chirality of the remaining kinks is the same as that of the ideal surface structure. LEED patterns from high Miller index surfaces with kinked steps have periodicity based on that of the terraces but modified by splitting of the diffraction spots due to the presence of the step edges.[49] The LEED patterns of the clean Cu(3,1,17)$^{R\&S}$ surfaces (Figure 3.2) display the square symmetry of the (100) terraces with obvious spot splitting. The split spots in the diffraction patterns are misoriented from the low Miller index directions, indicating that the steps run along low symmetry directions and are, therefore, kinked. Close inspection of the LEED patterns reveals that the direction of the spot splitting is reversed on Cu(3,1,17)^{S} and Cu(3,1,17)^{R} images and that the LEED patterns are non-superimposable mirror images of one another. Thus, the LEED patterns of the clean Cu(3,1,17)^{S} and Cu(3,1,17)^{R} surfaces reveal the fact that their atomic surface structures are enantiomorphous and retain their surface chirality after sputtering and annealing under UHV conditions.

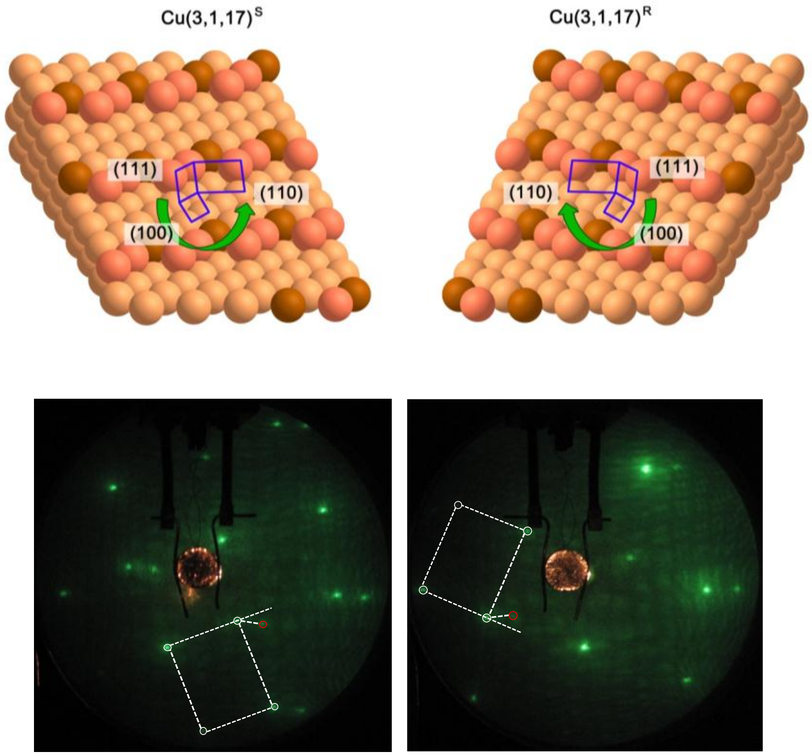

Figure 3.2: Upper panel. Ball model depiction of the naturally chiral Cu{3,1,17}$^{R\&S}$ surfaces. The kinked structures with clockwise and counterclockwise rotations among the three microfacets forming the terrace, step and kink, (111) → (100) → (110), are designated R and S, respectively. Lower panel. LEED patterns from clean Cu(3,1,17)$^{R\&S}$ single crystal surfaces (E = 225 eV, T = 90 K). The dashed lines highlight the repeating unit cell and the direction of the spot splitting due to the step edges. These are non-superimposable mirror images of one another, reflecting the chirality of the surfaces.

3.3.4 Enantiodifferentiation of adsorbed D- and L-alanine*

Prior to probing the enantioselectivity of DL-alanine adsorption on the Cu(3,1,17)$^{R\&S}$ surfaces, temperature programmed reaction spectra (TPRS) were obtained from D-alanine/Cu(3,1,17)^{R}. During exposure to D-alanine, the surface was held at 440 K to prevent multilayer formation on the surface. After the surface was saturated with D-alanine, the sample was heated in front of the mass spectrometer at 1 K/s while monitoring the desorption signals at various mass-to-charge ratios. During heating, D-

* Results reported in this section were obtained by Dr. Gellman's group at Carnegie Mellon University

alanine/Cu(3,1,17)^R decomposed into several products and the species desorbing from the surface yielded prominent signals at m/q = 28, 41, and 44 in the mass spectrometer. While the identification of all decomposition products was not attempted for the purpose of this work, it is expected, by analogy with decomposition of other amino acids on Cu surfaces, that CO_2 (m/q = 44) is one of the major products.[21, 50-51]

For the purpose of enantiodiscrimination of two enantiomers of alanine, we have used isotopically labeled L-alanine ($HO_2{}^{13}C\text{-}CH(NH_2)\text{-}CH_3$) and unlabeled D-alanine. TPR spectra of D-alanine/Cu(3,1,17)^R and L-alanine/Cu(3,1,17)^S at saturation coverage are compared in Figure 3.3. Note that these two combinations are diastereomerically equivalent to one another and, as expected, the TPR spectra are identical, other than the fact that the product desorption signals appear at different masses as a result of isotopic label. During D-alanine decomposition the desorption signal at m/q = 44 is far greater than that m/q = 45, while the signal at m/q = 45 dominates during L-alanine decomposition. It is clear that the signals at m/q = 44 and 45 correspond to CO_2 and $^{13}CO_2$ desorption, respectively, and that they originate from the carboxylate groups of each alanine enantiomer. More importantly, the TPR spectra show that the signals at m/q = 44 from D-alanine and m/q = 45 from L-alanine can be used for enantiodiscrimination and for measurement of the relative coverages of the two enantiomer on the surface. It is also important to note that the TPR spectra of all four combinations of D- and L-alanine on the Cu(3,1,17)$^{R\&S}$ surfaces reveal no enantiospecificity to the decomposition kinetics (Figure 3.4).

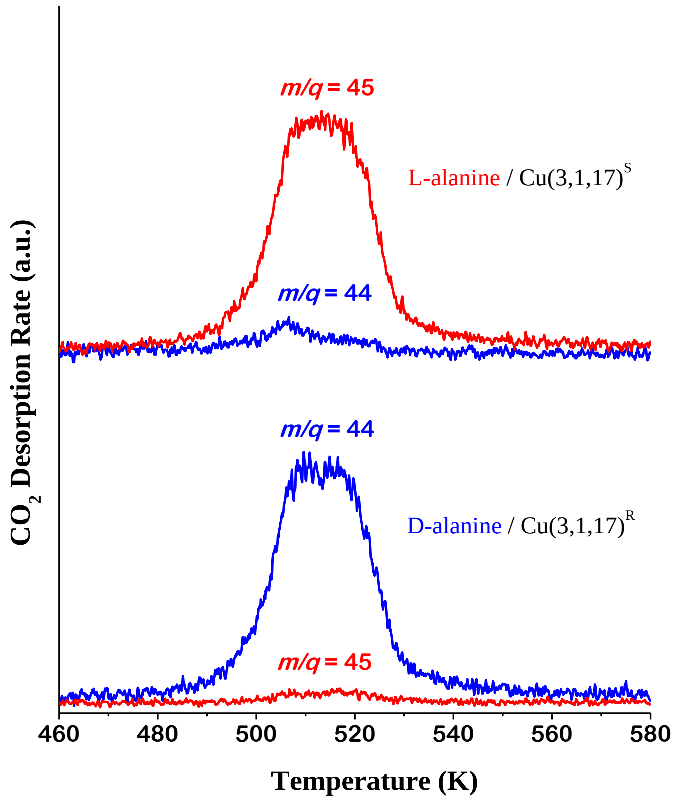

Figure 3.3: TPR spectra of D-alanine/Cu(3,1,17)^R and L-alanine/Cu(3,1,17)^S at saturation coverage. The signals at m/q = 44 and 45 correspond to CO_2 and $^{13}CO_2$ desorption originating from carboxylate groups of D- and L-alanine, respectively. The yields of CO_2 and $^{13}CO_2$ can be used to estimate the coverages of D- and L-alanine

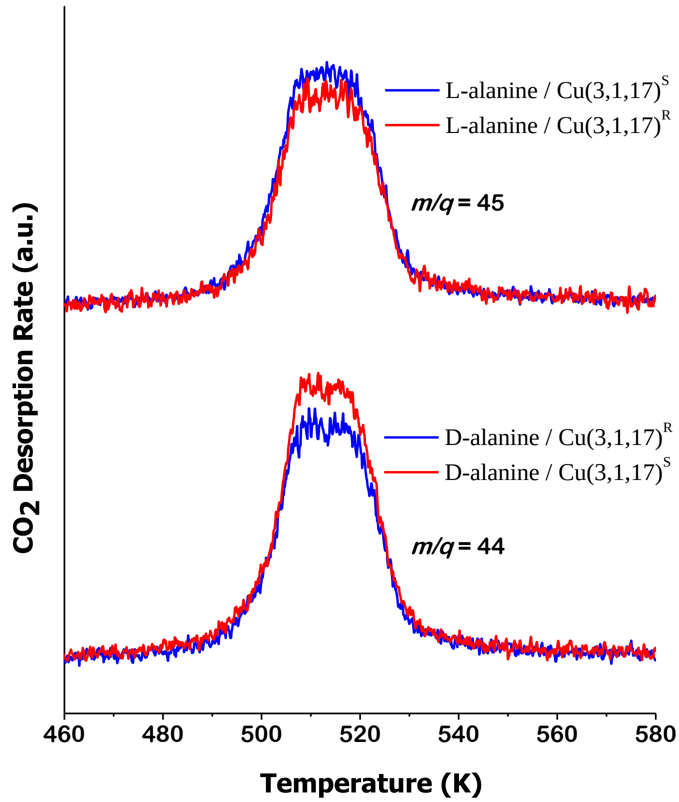

Figure 3.4: TPR spectra of D-alanine/Cu(3,1,17)$^{R\&S}$ and L-alanine/Cu(3,1,17)$^{R\&S}$ at saturation coverage. There is no measurable enantiospecificity in the alanine decomposition kinetics on Cu(3,1,17)$^{R\&S}$ surfaces.

As seen in Figure 3.3, the TPR spectra of L-alanine and D-alanine reveal small signals at m/q = 44 and 45, respectively. These may arise from isotopic impurities or from other decomposition products. In order to account for these minority signals during analysis of TPR spectra from mixed layers of D-alanine and L-alanine, the coverages of D- and L-alanine were calculated by solving the equations

$$Y_{44} = \alpha_{44}^{D}\theta_D + \alpha_{44}^{*L}\theta_{*L}$$

$$\text{and } \; Y_{45} = \alpha_{45}^{D}\theta_D + \alpha_{45}^{*L}\theta_{*L} \tag{3.4}$$

where $Y_{m/q}$ are the integrated areas under TPRS peaks at each m/q ratio, α are the coefficients for D- and L-alanine at each m/q ratio, and θ are the coverages of D- and L-alanine. D- and L-alanine yield signals at both m/q = 44 and 45 that are proportional to their coverages. The coefficients α_{44}^{D} and α_{45}^{D} (α_{44}^{*L} and α_{45}^{*L}) were obtained from the TPR spectra of pure D-alanine at $\theta_D = 1$ (pure L-alanine at $\theta_L = 1$). Using the system of equations ((**3.4**), the coverages of D- and L-alanine can be estimated from the integrated areas under the peaks at m/q = 44 and 45 measured during TPRS obtained after exposure to gas phase mixtures of the two enantiomers.

3.3.5 Relative adsorption energetics from experiment and DFT

The structures of dense D-, L-, and DL-alanine adlayer on Cu(3,1,17)^S surfaces predicted by DFT and illustrated in Figure 3.1 have one of the adsorbates on the (100) terrace and the other at the lower edge of the kinked step. Common features associated with the binding of the –CO_2 and the –NH_2 groups of the two adsorbates to the surface were observed in each of the most stable configurations of the three adlayers. Switching the chirality of the molecule adsorbed on the (100) terrace makes little difference to the adsorption energy, consistent with this being the achiral binding site. However, switching the chirality of the molecule adsorbed at the lower edge of the step has a significant impact on the binding energy, consistent with this being the chiral binding site and with enantiospecific adsorption of D- and L-alanine.

There was a notable inconsistency between DFT calculations and experimental observations. While the DFT calculations predicted an enantiospecific adsorption of D-, and L-alanine on Cu(3,1,17)^S, none was observed in experiment. One possible explanation was that since DFT calculations revealed the enantiopure and racemate alanine Cu(3,1,17)^S can have comparable energies, the contribution of a DL-alanine phase should be considered in analysis of the adsorption equilibria. However, the experimental method measures equilibria between adsorbed phases and gas phases of arbitrary composition. This allows for discrimination between the two mechanisms by which exposure to a racemic mixture in the gas phase leads to adsorption of a racemic mixture on the surface: the scenario in which the racemate DL-Alanine phase is far more stable than either D- or L-Alanine, and the scenario in which the energies of the D- and L-Alanine phases are indistinguishable. The latter with $\Delta\Delta E_{DL} \approx 0$ is consistent with the experimental results.

It is worthwhile addressing the question of why the DFT and experimental results might differ. One possibility is that the enantiospecific and configuration specific energy differences between the D-, L- and DL-Alanine phases on the Cu{3,1,17)$^{R\&S}$ surfaces are simply too small to be resolved by DFT, even when using a dispersion corrected functional. If one examines the enantiospecificities of reaction rates, desorption energetics, and adsorption equilibria measure on well-defined, naturally chiral single crystal surfaces,[21, 52-54] the highest enantiospecific difference in reaction energetics that one would estimate from those measurements is ~4 kJ/mole estimated for the desorption of methyl lactate from Cu(643)^R.[55] This may be the limit for DFT and prediction of enantioselectivities from computational modeling remains a challenge.[56]

The discrepancy between the predictions of DFT and the experimental measurement could also have resulted from an incorrect description of alanine on Cu(3,1,17)^S. The experimental measurements were performed for surfaces that were saturated with adsorbed alanine; however, an absolute coverage had not been quantitatively determined. The DFT model assumed an ideal dense monolayer coverage on Cu(3,1,17)^S unit cell. We were not able to directly measure the surface coverage of alanine in our experiments. It is also possible that other species were actually present on the surface. Other studies suggested that adsorbed acids such as amino acids and tartaric acid can extract Cu atoms from the surface to form adsorbed species that are better described as Cu salts than adsorbed carboxylates.[57-61] It may be possible that the species on the surface was a Cu-alaninate and the surface structures was quite different from the ideal dense monolayer coverage or even the ideal $Cu(3,1,17)^{S}$. Given the sensitive nature of this phenomena, the discrepancy between experimental results and DFT based simulation may not be entirely surprising. Converging to a fully consistent picture of the enantioselective adsorption of alanine on $Cu(3,1,17)^{R\&S}$ poses a challenge to both the computational methods and the experimental characterization of the system.

3.4 Conclusions

Adsorption of dense glycine and alanine adlayers on Cu(110) was studied using DFT calculations. The application of PBE-D2 significantly increased the adsorption energy of the dense adlayers. The calculations predicted that racemate alanine domain on Cu(110) will not segregate into enantiopure D- and L-alanine domains. For glycine domain, it also indicated that there is no preference between the heterochiral and homochiral glycine domains on Cu(110). The calculation also indicated that the O and N atom offset between the heterochiral and homochiral glycine domain were minimal, and the apparent experimental discrepancy between LEED, STM, and XPS discussed in earlier works does not exist.[9-11]

The adsorption energetic of enantiopure alanine and racemate alanine were investigated by both experimental study and DFT calculations. The DFT calculations predicted that there are no measurable differences between the adsorption of enantiopure

L-alanine phase and racemate DL-alanine phase on $Cu(3,1,17)^S$. The suggested a lack of enantiospecificity on Cu(3,1,17); however, experimental measurement indicated a small enantiospecificity between the enantiopure L-alanine phase and the enantiopure D-alanine phase. This discrepancy may be result of limitations of DFT calculations, for examining small energy differences, or differences in the detailed chemical structures between these examined in our calculations and those present experimentally. Due to these constraints, accurate predictions of minute enantiospecificity using computational simulation remain a challenge.

3.5 References

1. Bonner, W. A., The Origin and Amplification of Biomolecular Chirality. *Orig Life Evol Biosph* **1991,** *21* (2), 59-111.

2. Bada, J. L., Biomolecules - Origins of Homochirality. *Nature* **1995,** *374* (6523), 594-595.

3. Merino, I. M.; Gonzalez, E. B.; Sanzmedel, A., Liquid-Chromatographic Separation of Penicillamine Enantiomers Derivatized with Opa/2-Me on a Beta-Cyclodextrin Bonded Phase. *Mikrochim. Acta* **1992,** *107* (1-2), 73-80.

4. Sholl, D. S.; Gellman, A. J., Developing Chiral Surfaces for Enantioselective Chemical Processing. *AIChE Journal* **2009,** *55* (10), 2484-2490.

5. Smith, S. W., Chiral toxicology: it's the same thing...only different. *Toxicol. Sci.* **2009,** *110* (1), 4-30.

6. Erb, S., Single-enantiomer drugs poised for further market growth. *Pharm. Technol.* **2006,** *30*, s14-s18.

7. Kang, J. H.; Toomes, R. L.; Polcik, M.; Kittel, M.; Hoeft, J. T.; Efstathiou, V.; Woodruff, D. P.; Bradshaw, A. M., Structural investigation of glycine on Cu(100) and comparison to glycine on Cu(110). *The Journal of Chemical Physics* **2003,** *118* (13), 6059.

8. Chen, Q.; Frankel, D.; Richardson, N., Chemisorption induced chirality: glycine on Cu{110}. *Surf Sci* **2001,** *497*, 37-46.

9. Toomes, R. L.; Kang, J. H.; Woodruff, D.; Polcik, M.; Kittel, M.; Hoeft, J. T., Can glycine form homochiral structural domains on low-index copper surfaces. *Surface Science Letters* **2003,** *522*, L9-L14.

10. Chen, Q.; Frankel, D. J.; Richardson, N. V., Chemisorption induced chirality: glycine on Cu{110}. *Surf Sci* **2002,** *497* (1-3), 37-46.

11. Rankin, R.; Sholl, D., Assessment of heterochiral and homochiral glycine adlayers on Cu(110) using density functional theory. *Surf Sci* **2004,** *548* (1-3), 301-308.

12. Rankin, R.; Sholl, D., Structure of Glycine, Enantiopure Alanine, and Racemic Alanine Adlayers on Cu(110) and Cu(100) Surfaces. *Journal of Physical Chemistry B* **2005,** *109* (35), 16764-16773.

13. Rankin, R. B.; Sholl, D. S., First-principles studies of chiral step reconstructions of Cu(100) by adsorbed glycine and alanine. *The Journal of Chemical Physics* **2006,** *124* (7), 074703.

14. Rankin, R. B.; Sholl, D. S., Structure of enantiopure and racemic alanine adlayers on Cu(110). *Surf Sci* **2005,** *574* (1), L1-L8.

15. Efstathiou, V.; Woodruff, D. P., Characterisation of the interaction of glycine with Cu(100) and Cu(111). *Surf Sci* **2003,** *531* (3), 304-318.

16. Zhao, X.; Wang, H.; Zhao, R.; Yang, W., Self-assembly of amino acids on the Cu(001) surface. *Materials Science & Engineering C* **2001,** *16*, 41-50.

17. Barlow, S.; Louafi, S.; Leroux, D.; Williams, J.; Muryn, C.; Haq, S.; Raval, R., Polymorphism in supramolecular chiral structures of R- and S-alanine on Cu(110). *Surf Sci* **2005,** *590* (2-3), 243-263.

18. Haq, S.; Moslemzadeh, N.; Robin, A.; Barlow, S.; Raval, R., Racemic versus Enantiopure Alanine on Cu110: An Experimental Study. *Langmuir* **2007,** *23* (21), 10694-10700.

19. Iwai, H.; Egawa, C., Molecular Orientation and Intermolecular Interaction in Alanine on Cu(001). *Langmuir* **2010,** *26* (4), 2294-2300.

20. Zhao, X.; Zhao, R.; Yang, W., Adsorption of alanine on Cu(001) studied by scanning tunneling microscopy. *Surf Sci* **1999,** *442*, L995-L1000.

21. Yun, Y. J.; Gellman, A. J., Enantioselective Separation on Naturally Chiral Metal Surfaces: d,l-Aspartic Acid on Cu(3,1,17)(R&S) Surfaces. *Angew. Chem., Int. Ed.* **2013,** *52* (12), 3394-3397.

22. Williams, J.; Haq, S.; Raval, R., The bonding and orientation of the amino acid L-alanine on Cu{110} determined by RAIRS. *Surf. Sci.* **1996,** *368*, 303-309.

23. Haq, S.; Massey, A.; Moslemzadeh, N.; Robin, A.; Barlow, S. M.; Raval, R., Racemic versus enantiopure alanine on Cu(110): An experimental study. *Langmuir* **2007,** *23* (21), 10694-10700.

24. Iwai, H.; Egawa, C., Molecular orientation and intermolecular interaction in alanine on Cu(001). *Langmuir* **2010,** *26* (4), 2294-300.

25. Gladys, M. J.; Stevens, A. V.; Scott, N. R.; Jones, G.; Batchelor, D.; Held, G., Enantiospecific adsorption of alanine on the chiral Cu{531} surface. *J. Phys. Chem. C* **2007,** *111* (23), 8331-8336.

26. Held, G.; Gladys, M. J., The Chemistry of Intrinsically Chiral Surfaces. *Topics in Catalysis* **2008,** *48* (1-4), 128-136.

27. Clegg, M. L.; Morales de la Garza, L.; Karakatsani, S.; King, D. A.; Driver, S. M., Chirality in Amino Acid Overlayers on Cu Surfaces. *Top. Catal.* **2011,** *54* (19-20), 1429-1444.

28. Rankin, R. B.; Sholl, D. S., Structures of dense glycine and alanine adlayers on chiral Cu(3,1,17) surfaces. *Langmuir* **2006,** *22* (19), 8096-8103.

29. Rankin, R. B.; Sholl, D. S., First-principles studies of chiral step reconstructions of Cu(100) by adsorbed glycine and alanine. *J. Chem. Phys.* **2006,** *124* (7), 74703.

30. Kresse, G.; Hafner, J., Ab initio molecular-dynamics for liquid-metals. *Physical Review B* **1993,** *47* (1), 558-561.

31. Kresse, G.; Hafner, J., Ab initio molecular-dynamics simulation of the liquid-metal–amorphous-semiconductor transition in germanium. *Physical Review B* **1994,** *49* (20), 14251-14269.

32. Kresse, G.; Furthmuller, J., Efficiency of ab-initio total energy calculations for metals and semiconductors using a plane-wave basis set. *Comput. Mater. Sci.* **1996,** *6* (1), 15-50.

33. Kresse, G.; Furthmuller, J., Efficient iterative schemes for ab initio total-energy calculations using a plane-wave basis set. *Physical Review B* **1996,** *54* (16), 11169-11186.

34. Perdew, J. P.; Burke, K.; Wang, Y., Generalized gradient approximation for the exchange-correlation hole of a many-electron system. *Physical Review B* **1996,** *54* (23), 16533-16539.

35. Perdew, J. P.; Burke, K.; Ernzerhof, M., Generalized gradient approximation made simple (vol 77, pg 3865, 1996). *Physical Review Letters* **1997,** *78* (7), 1396-1396.

36. Blochl, P. E., Projector Augmented-Wave Method. *Physical Review B* **1994,** *50* (24), 17953-17979.

37. Kresse, G.; Joubert, D., From ultrasoft pseudopotentials to the projector augmented-wave method. *Physical Review B* **1999,** *59* (3), 1758-1775.

38. Grimme, S., Semiempirical GGA-type density functional constructed with a long-range dispersion correction. *Journal of Computational Chemistry* **2006,** *27* (15), 1787-1799.

39. Zhao, X. Y.; Gai, Z.; Zhao, R. G.; Yang, W. S.; Sakurai, T., Adsorption of glycine on Cu(001) and related step faceting and bunching. *Surf Sci* **1999,** *424* (2-3), L347-L351.

40. Sayago, D. I.; Polcik, M.; Nisbet, G.; Lamont, C. L. A.; Woodruff, D. P., Local structure determination of a chiral adsorbate: Alanine on Cu(110). *Surf Sci* **2005,** *590* (1), 76-87.

41. Sayago, D.; Polcik, M.; Nisbet, G.; Lamont, C.; Woodruff, D., Local structure determination of a chiral adsorbate: Alanine on Cu(110). *Surf Sci* **2005,** *590* (1), 76-87.

42. Ge, S.; Lu, C.; Zhao, R., Adsorption of L-Alanine on Cu(111) Studied by Scanning Tunnelling Microscopy. *Chinese Physics Letter* **2006,** *23* (6), 1558-1561.

43. Rankin, R.; Sholl, D., Structure of Dense Glycine and Alanine Adlayers on Chiral Cu(3,1,17) Surface. *Langmuir* **2006,** *22* (19), 8096-8103.

44. Sholl, D. S.; Asthagiri, A.; Power, T. D., Naturally chiral metal surfaces as enantiospecific adsorbents. *J. Phys. Chem. B* **2001,** *105* (21), 4771-4782.

45. Power, T. D.; Asthagiri, A.; Sholl, D. S., Atomically detailed models of the effect of thermal roughening on the enantiospecificity of naturally chiral platinum surfaces. *Langmuir* **2002,** *18* (9), 3737-3748.

46. Asthagiri, A.; Feibelman, P. J.; Sholl, D. S., Thermal fluctuations in the structure of naturally chiral Pt surfaces. *Top. Catal.* **2002,** *18* (3-4), 193-200.

47. Baber, A. E.; Gellman, A. J.; Sholl, D. S.; Sykes, E. C. H., The real structure of naturally chiral Cu{643}. *J. Phys. Chem. C* **2008,** *112* (30), 11086-11089.

48. Clegg, M. L.; Driver, S. M.; Blanco-Rey, M.; King, D. A., Atomic Roughness of an Intrinsically Chiral Surface Orientation of an fcc Metal: Cu{531}. *J. Phys. Chem. C* **2010,** *114* (9), 4114-4117.

49. Ertl, G.; Küppers, J., *Low energy electrons and surface chemistry*. 2nd, completely rev. ed.; VCH: Weinheim, Federal Republic of Germany ; Deerfield Beach, FL, USA, 1985; p xii, 374 p.

50. Eralp, T.; Cornish, A.; Shavorskiy, A.; Held, G., The Study of Chiral Adsorption Systems Using Synchrotron-Based Structural and Spectroscopic Techniques: Stereospecific Adsorption of Serine on Au-Modified Chiral Cu{531} Surfaces. *Top. Catal.* **2011,** *54* (19-20), 1414-1428.

51. Roth, C.; Ernst, K. H., Surface Explosion Chemistry of Malic Acid on Cu(110). *Top. Catal.* **2011,** *54* (19-20), 1378-1383.

52. Gellman, A. J.; Huang, Y.; Feng, X.; Pushkarev, V. V.; Holsclaw, B.; Mhatre, B. S., Superenantioselective Chiral Surface Explosions. *J. Am. Chem. Soc.* **2013,** *135* (51), 19208-19214.

53. Cheong, W. Y.; Gellman, A. J., Energetics of Chiral Imprinting of Cu(100) by Lysine. *J. Phys. Chem. C* **2011,** *115* (4), 1031-1035.

54. Horvath, J. D.; Gellman, A. J., Enantiospecific desorption of chiral compounds from chiral Cu(643) and achiral Cu(111) surfaces. *J. Am. Chem. Soc.* **2002,** *124* (10), 2384-2392.

55. Fleming, C.; King, M.; Kadodwala, M., Highly Efficient Electron Beam Induced Enantioselective Surface Chemistry. *J. Phys. Chem. C* **2008,** *112* (47), 18299-18302.

56. Sholl, D.; Steckel, J., *Density functional theory : a practical introduction*. John Wiley & Sons: Hoboken, 2009.

57. Roth, C.; Parschau, M.; Ernst, K. H., Chiral Reconstruction of a Metal Surface by Adsorption of Racemic Malic Acid. *ChemPhysChem* **2011,** *12* (8), 1572-1577.

58. Roth, C.; Passerone, D.; Merz, L.; Parschau, M.; Ernst, K. H., Two-Dimensional Self-Assembly of Chiral Malic Acid on Cu(110). *J. Phys. Chem. C* **2011,** *115* (4), 1240-1247.

59. Mhatre, B. S.; Pushkarev, V.; Holsclaw, B.; Lawton, T. J.; Sykes, E. C. H.; Gellman, A. J., A Window on Surface Explosions: Tartaric Acid on Cu(110). *J. Phys. Chem. C* **2013,** *117* (15), 7577-7588.

60. Lawton, T. J.; Pushkarev, V.; Wei, D.; Lucci, F. R.; Sholl, D. S.; Gellman, A. J.; Sykes, E. C. H., Long Range Chiral Imprinting of Cu(110) by Tartaric Acid. *J. Phys. Chem. C* **2013,** *117* (43), 22290-22297.

61. Zhao, X. Y.; Zhao, R. G.; Yang, W. S., Scanning tunneling microscopy investigation of L-lysine adsorbed on Cu(001). *Langmuir* **2000,** *16* (25), 9812-9818.

CHAPTER 4

PHYSISORPTION OF R-3-METHYCYCLOHEXANONE ON COPPER SURFACES

4.1 Introduction*

The emergence of dispersion force corrections to DFT methods has allowed us to reexamine interesting adsorbates for which physisorption forces are expected to contribute significantly to adsorption. In this chapter, we investigated three different dispersion corrected methods – Grimme's D2 (D2), vdW-optB86b (B86b), and vdW-optB88 (B88). The D2 tackles the dispersion correction through the introduction of a semi-empirical dispersion force correction to the GGA functional.[1-2] The optimized B86b method uses a new gradient-corrected exchange energy to account for interaction in systems with large density gradient.[3-4] The optimized B88 method further improves this through an improved asymptotic potential for the gradient-corrected exchange energy approximation.[5-7]

Temperature-programmed desorption (TPD) has been used to study the adsorption and desorption of R-3-methylcyclohexanone (R-3MCHO) on a large set of Cu single crystal surfaces that spans the stereographic triangle and includes the three low Miller index surfaces Cu(111), Cu(110) and Cu(100), six stepped surfaces Cu(221), Cu(771), Cu(533), Cu(511), Cu(410) and Cu(430), and seven kinked surfaces Cu(643)$^{R\&S}$,

---

* Published as Wei, D.; Mhatre, B.; Gellman, A.; Sholl, D., Contributions of dispersion Forces to R-3-Methycyclohexanone Physisorption on Low and High Miller Index Cu Surfaces. *Surface Science*. **2014,** 629, 35-40

Cu(653)$^{R\&S}$, Cu(17,5,1)$^{R\&S}$, Cu(13, 9, 1)$^{R\&S}$, Cu(821)$^{R\&S}$, Cu(651)$^{R\&S}$, and Cu(531)$^{R\&S}$.[8] TPD results show that the desorption energies, ΔE_{des}, of R-3MCHO from the terraces are roughly equivalent on all surfaces, as are the desorption energies from the step sites and the kink sites. Not surprisingly, the trend among the desorption energies is $\Delta E_{des}^{terr} < \Delta E_{des}^{step} < \Delta E_{des}^{kink}$. Using the nonhybrid PW-91 functional, DFT calculation of the adsorption energy of R-3MCHO on Cu(111) and Cu(322) yielded values that were ~0.45 eV lower than the experimental values.[9] This discrepancy was attributed to PW-91's inability to account for dispersion contributions to the binding of R-3MCHO to the Cu surfaces. A similar study using the nonhybrid PBE functional estimated the benzene desorption energy on Cu(111) to be −0.06 eV,[10] but experiments estimated the adsorption energy to be between −0.53 and −0.62 eV.[11-12]

In this chapter, we investigate R-3-methylcyclohexanone (R-3MCHO) adsorption on Cu surfaces as a benchmark test for the three dispersion corrected methods, and to quantify the effectiveness of these dispersion corrected methods for predicting surface–adsorbate interaction by examining R-3MCHO physisorption behavior on the low and high Miller index Cu surfaces. All experimental results discussed below were obtained by Dr. Mhatre in Dr. Gellman's group at Carnegie Mellon University.

4.2 Methodology

4.2.1 Density Functional Theory

Periodic DFT calculations were conducted with the Vienna Ab initio Simulation Package (VASP).[13-16] The electron–electron exchange and correlation interactions were described with the PBE-GGA functional.[17-18] Core–electron interactions were modeled with the projector augmented-wave (PAW) potential.[19-20] All calculations used a plane wave expansion cutoff of 500 eV. Structural optimization was performed by a conjugate gradient algorithm with a force stopping criterion of 0.03 eV/Å. Dispersion force were modelled with Grimme's D2 (PBE-D2), the vdW_optB86b (PBE-B86b), and the vdW_optB88 (PBE-B88) dispersion corrected methods.[2, 7] Bulk Cu atoms were examined with 8 Cu atoms in an FCC lattice with $16 \times 16 \times 16$ *k*-points. The atomic positions, unit cell shape, and unit cell size were allowed to relax for each method. The lattice constants are reported in Table 4.1. The Cu lattice constants predicted by PBE-D2, PBE-B86b, and PBE-B88 were found to be 1.74%, 0.85%, and 0.10% smaller, respectively, than the lattice constant calculated by PBE-GGA. All surface calculations were performed using the optimized lattice constant determined with the functional used in that calculation.

Table 4.1: Bulk Cu lattice constant for each dispersion corrected method

Functional	Lattice constant (Å)
PBE-GGA	3.63
PBE-D2	3.57
PBE-B86b	3.60
PBE-B88	3.63

All surface calculations had a vacuum spacing of at least 10 Å. The required slab thickness was determined with R-3MCHO adsorption on Cu(111). The minimum thickness was achieved when the presence of an additional layer changed the R-3MCHO adsorption energy by less than 0.05 eV. This was determined to be three Cu(111) layers with the bottommost layer immobilized. Unless otherwise stated, surfaces were modeled as an approximately 7 Å thick slab with the bottommost 3 Å immobilized. Molecules were only adsorbed on one side of the slab. The low Miller index Cu(111), Cu(100), and Cu(110) surfaces were made up of p(5 × 5) surface unit cells and were examined with 3 × 3 × 1 *k*-points. The stepped Cu(221) and Cu(322) surfaces were modeled with p(2 × 6) surface unit cells. The kinked $Cu(643)^R$ consisted of one surface unit cell. Calculations for the stepped and kinked surfaces used 2 × 2 × 1 *k*-points. The resolution in *k*-points was chosen to ensure good convergence while minimizing computational cost. Table 4.2 below demonstrated that these *k*-points offer sufficient convergence for our study.

Table 4.2: The total adsorption energy per unit cell (in eV) on different surfaces as a functional of resolution in *k*-points.

k-points	Cu(111)	Cu(100)	Cu(100)	Cu(221)	$Cu(643)^R$
1×1×1	-1.16	-1.20	-1.22	-1.40	-1.58
2×2×1	-1.02	-1.18	-1.14	-1.50	-1.49
3×3×1	-1.05	-1.17	-1.17	-1.44	-1.51
4×4×1	-1.04	-1.18	-1.15	-1.46	-1.52

Calculations were also performed for a reconstructed Cu(110) surface to mimic the (2 × 1) missing-row reconstruction seen for Pt(110).[21-23] The (2 × 1) missing-row reconstructed Cu(110) surface was modeled with a slab approximately 10 Å thick with the bottommost 5 Å immobilized. The reconstructed Cu(110) supercell had a p(2 × 5) surface unit cell and used 2 × 2 × 1 *k*-points. A single R-3MCHO was placed on each computational supercell to simulate adsorption. An isolated R-3MCHO molecule in a 20 × 20 × 20 Å cell sampled at the Γ point was used as the reference. Various geometric configurations were examined, and only the lowest energy state was used as the reference state. On the unreconstructed surfaces, the adsorption energy was defined as,

$$\Delta E_{Adsorption} = E_{total} - E_{3MCHO} - E_{Surface} \tag{4.5}$$

where E_{total}, E_{3MCHO}, $E_{Surface}$ are the total energy of the relaxed structure including the adsorbed molecule, the energy of the isolated R-3MCHO, and the unreconstructed surface energy, respectively. For the reconstructed surface, the adsorption energy had to account for the energy lost to the reconstruction. The effective adsorption energy was defined as,

$$\Delta E_{Effective\ Adsorption} = E_{total} - E_{3MCHO} - E_{Reconstructed\ Surface} - A * \Delta E_{Reconstruction} \tag{4.6}$$

where $E_{Reconstructed\ Surface}$ is the total energy of the clean reconstructed surface, A is the reconstructed surface area, and $\Delta E_{Reconstruction}$ is the energy required to reconstruct 1 Å^2 of the surface. An unfavorable reconstruction where energy from the environment is required for the reconstruction would result in a negative $\Delta E_{Reconstruction}$.

Multiple preferred adsorption configurations and location combinations were systematically examined for each surface. A list of possible adsorption geometries for each surface was generated by placing oxygen on a large number of possible high symmetry surface sites and allowing the methylcyclohexane group to rotate around the oxygen. On high Miller index surface, special attention was paid to examine geometries where the methylcyclohexane group was on top of the stepped or kinked sites. Typically, these initial geometries converged to a few selective local minima, and only the most energetically preferred states were used in this chapter. The unit vectors and fractional coordinates of the most preferred states can be found in Appendix D – G.

4.2.2 TPD experiment

TPD has been used to measure the influence of surface structure on the desorption energies of R-3MCHO from a large set of Cu(hkl) single crystal surfaces under ultra-high vacuum (UHV) conditions. Details of the experimental measurements can be found in prior publications.[24-27] Briefly, the single crystal surfaces were cleaned in UHV by cycles of Ar^+ ion sputtering and annealing at temperatures in the range 800–1000 K. The orientation and the crystallinity of the surfaces were examined using low energy electron diffraction. Once the Cu surfaces were clean, R-3MCHO was adsorbed at temperatures of ~170 K by exposure of the surfaces to vapor introduced into the UHV chamber through a leak valve. The adsorption temperature of 170 K limited the coverage to one monolayer and prevented the formation of condensed multilayers. TPD of the adsorbed monolayer was performed by positioning the Cu single crystal in front of the aperture to a mass spectrometer and heating the crystal at 1 K/s while monitoring the signal at m/q = 39 amu ($C_3H_3^+$).

4.3 Results and Discussion

4.3.1 TPD data

One of the important features of R-3MCHO adsorption on the single crystal Cu surfaces is that its binding energy is sensitive to the local structure of the adsorption site. As a consequence, the desorption temperature in a TPD experiment is indicative of the local structure of the site from which the R-3MCHO desorbed.[24-30] The data in Figure 4.1 show the TPD spectra obtained from saturated monolayer of R-3MCHO adsorbed on the Cu(111), Cu(100), Cu(110), Cu(221), and $Cu(643)^R$ surfaces. In the classification system of Jenkins et al. the Cu(111) and Cu(100) surfaces are considered flat while the Cu(110) and Cu(221) are considered to be stepped.[31] Desorption of R-3MCHO from flat Cu terraces occurs at ~230 K. R-3MCHO desorption from stepped edges occurs at ~345 K. Using the microfacet framework of van Hove and Somorjai, the Cu(643)^R structure has a (111) terrace, (100) step edge, and a (110) kink.[32] The R-3MCHO TPD spectrum from the Cu(643)^R surface exhibits three resolved desorption features at 230, 345, and 385 K that can readily be assigned to desorption from flat terraces, steps, and kinks, respectively.[24, 28-29]

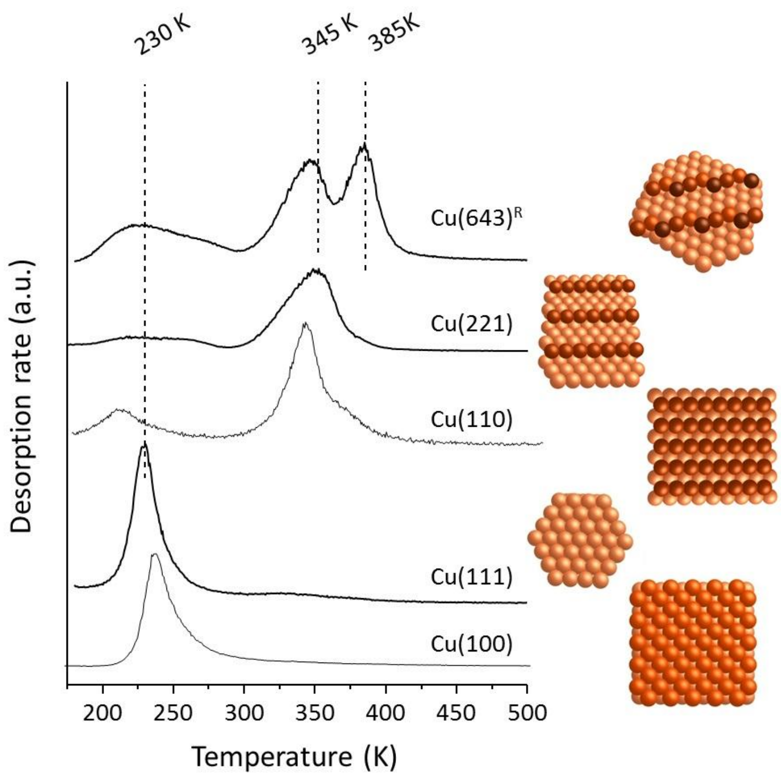

Figure 4.1: TPD of R-3MCHO on various Cu surfaces. The peak temperatures for desorption from the flat terraces, the steps and the kinks are ~230, ~345, and ~385 K, respectively. Insets to the right show the ideal structure of each surface, with color coding used to indicate the coordination number of surface atoms.

The adsorption energies of R-3MCHO on the Cu surfaces are determined from the peak desorption temperatures. Following the Redhead method for first order desorption,[33] we calculated the adsorption energy from the peak desorption temperature using

$$E_d/RT_P^2 = v/\beta * \exp(-E_d/RT_P) \qquad (4.7)$$

where $E_d = -E_a$ is the measured desorption energy, R is the gas constant, T_P is the peak desorption temperature in Kelvin, v is the prefactor, and β is the heating rate. In all cases, β = 1 K/s and we assumed $v = 10^{18}$ s^{-1}.[34] This analysis assumes that the adsorption energy is independent of surface coverage on each surface and that v is constant for R-3MCHO desorption from all Cu surfaces. The peak desorption temperature for each Cu surfaces and the resulting adsorption energies are listed in Table 4.3.

Table 4.3: Adsorption energy ($\boldsymbol{E_a}$) of R-3MCHO on Cu surfaces

Surface	Peak T (K)	E_a (eV)
Cu(111)	230	-0.85
Cu(100)	235	-0.87
Cu(110)	335	-1.26
Cu(221)	348	-1.31
$Cu(643)^R$	385	-1.45

While the pre-factor v is not exact, the adsorption energies are only weakly sensitive to changes in the pre-factor values. If v is lowered by an order of magnitude, the adsorption energy on $Cu(643)^R$ in Table 4.3 changes to−1.37 eV, a decrease of less than 5%. This difference impacts neither the analysis nor the conclusions presented in this chapter.

4.3.2 Adsorption on Cu(111), Cu(110), and Cu(100)

Figure 4.2 illustrates the adsorption geometries of R-3MCHO on low Miller index Cu surfaces, as calculated by PBE-D2. The carbonyl group binds between two adjacent surface Cu atoms. The cyclohexane ring adopts the chair formation with the methyl group in an equatorial position, and the ring lies flat on the surface with a slight tilt towards the methyl group. Similar geometries were observed on Cu(110) and Cu(100). The dominant role of the carbonyl group in binding the R-3MCHO to the surface is consistent with the large frequency shifts observed in the FTIR spectra of R-3MCHO on the Cu(643)$^{R\&S}$ surfaces.[35]

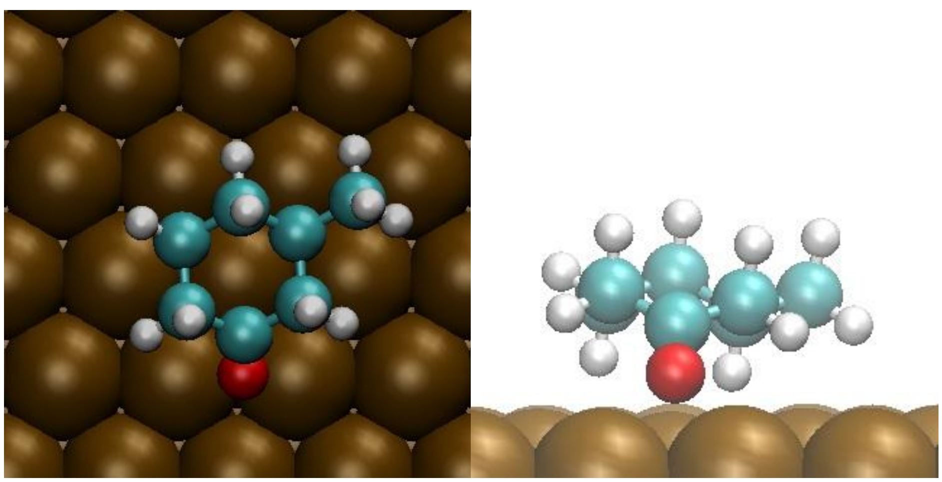

Figure 4.2: Adsorption geometry of 3MCHO on Cu(111), as calculated with DFT using the PBE-D2 functional.

The experimental and DFT calculated R-3MCHO adsorption energies on the low Miller index Cu surfaces are given in Table 4.4. The PBE-GGA functional underestimated the adsorption energy of R-3MCHO by 0.56– 0.85 eV/adsorbate on these Cu surfaces. This result is similar to that of Bhatia and Sholl, who reported a 0.45 eV/adsorbate underestimation of the R-3MCHO adsorption energy on Cu(111) using the

PW-91 functional.[9] It is also consistent with McNellis et al., who reported a 0.55 eV/adsorbate underestimation of the adsorption energy of benzene on Cu(111) with the PBE functional.[10] The dispersion corrected methods overestimated the adsorption energy of R-3MCHO on the low index Cu surfaces by 0.06–0.32 eV/adsorbate. Similar overbinding of adsorption has been reported by Grimme et al.[36]

We also calculated the dispersion contributions to the adsorption energy by subtracting the PBE-GGA based adsorption energy from each of the dispersion corrected methods. Table 4.5 shows the dispersion contribution to total adsorption energy and as a percentage of the total adsorption energy for each method. The large dispersion contributions are consistent with a physisorbed molecule. The variations in dispersion contributions among the surfaces were correlated with the atomic densities of the different surfaces: Cu(111) > Cu(100) > Cu(110). We also reported the distance between the plane of the surface Cu atom and the center of the cyclohexane ring for R-3MCHO on Cu(111) in Table 4.4. The calculated heights for the dispersion corrected methods were similar to the value of 3.6 Å reported by Witte et al. for cyclohexane binding above Cu(111).[37] In that work, the inclusion of the dispersion forces brought the cyclohexane ring closer to the Cu(111) surface by 0.14–0.32 Å, depending upon which correction method was used. Compared to the other two dispersion correction methods, the shorter distance predicted using PBE-D2 also points to its stronger overbinding of the adsorbate.

Table 4.4: Summary of R-3MCHO adsorption energies (eV) on the low Miller index Cu surfaces. Italic values in parenthesis are differences between calculated results and those estimated on the basis of TPD data.

	TPD	PBE-GGA	PBE-D2	PBE-B86b	PBE-B88
Cu(111)	-0.85	-0.15 *(0.70)*	-1.07 *(-0.22)*	-0.98 *(-0.13)*	-0.93 *(-0.08)*
Cu(100)	-0.87	-0.31 *(0.56)*	-1.19 *(-0.32)*	-1.20 *(-0.33)*	-1.15 *(-0.28)*
Cu(110)	-1.26	-0.41 *(0.85)*	-1.19 *(0.07)*	-1.21 *(0.05)*	-1.15 *(0.11)*
Height Above Cu(111) (Å)		3.80	3.48	3.66	3.60

Table 4.5: Dispersion contribution to total adsorption energies (eV) for R-3MCHO adsorption on low Miller index Cu surfaces.

	PBE-D2	PBE-B86b	PBE-B88
Cu(111)	-0.92 (86%)	-0.83 (84%)	-0.78 (83%)
Cu(100)	-0.88 (74%)	-0.89 (74%)	-0.84 (73%)
Cu(110)	-0.78 (65%)	-0.80 (66%)	-0.74 (64%)

On the surfaces listed in Table 4.4, the PBE-GGA functional predicts the strongest binding to the Cu(110) surface followed by binding on Cu(100) and then on Cu(111). The carbonyl group preference for binding to the less coordinated surface Cu atoms probably contributed to this ordering of adsorption strengths. The dispersion corrected methods all predicted similar adsorption energies on Cu(100) and Cu(110), which was not consistent with our TPD observations. The experimental results show that R-3MCHO binds most strongly to Cu(110), and that the adsorption energy on Cu(100) is roughly equal to that on Cu(111). In section 4.3.4, we attempt to address this shortcoming by considering a possible surface reconstruction of Cu(110). While the PBE-B88 method provided the most accurate adsorption energies, the improvement over the other methods was not significant. Since the PBE-D2 method does not account for screening in the sea of electrons, the method may be regarded as less accurate on metal surfaces. Preliminary calculations, however, did not indicate a clear disadvantage to this method as compared to PBE-B86b and PBE-B88. Because our study was focused on examining the adsorption energy differences of R-3MCHO on other Cu surfaces, the inaccuracy due to screening would affect all surfaces similarly and lessen the impact on overall results. With these observations, we reduced calculation complexity for the remaining results described below by employing only the PBE-D2 dispersion corrected method to examine adsorption of R-3MCHO on the Cu(221) and Cu(643) surfaces.

4.3.3 Adsorption on Cu(221) and Cu(643)^{R}

Our study also probed the ability of dispersion corrected DFT methods to describe the differences in R-3MCHO adsorption energies on low and high Miller index Cu surfaces. Earlier calculations have indicated a distinct increase in adsorption energy from low to high Miller index surfaces. The adsorption geometries of R-3MCHO on the straight steps and kinked step edge are illustrated in Figure 4.3. On both Cu(221) and Cu(643)^{R}, the carbonyl group binds between Cu atoms in the straight step edge. Similar to its adsorption on low Miller index surfaces, the cyclohexane ring adopted a chair conformation. The ring lies flat against the terrace with a tilt towards the methyl group. Due to the presence of the kinked step edge, the tilt was more pronounced on Cu(643)^{R}.

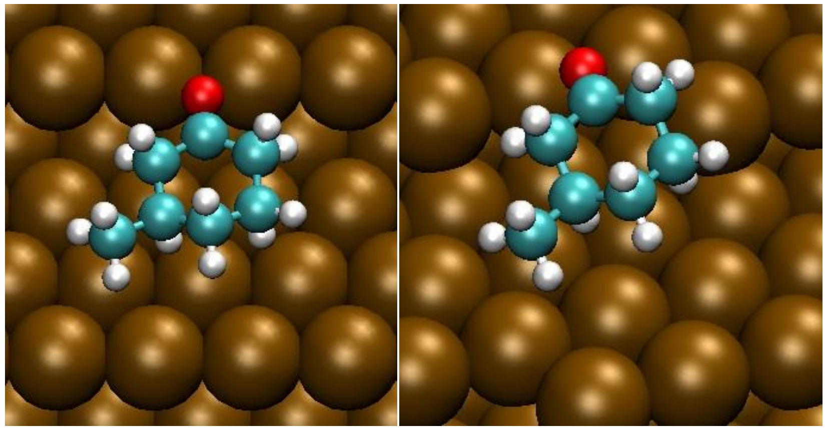

Figure 4.3: Adsorption geometry of R-3MCHO on Cu(221) (Left) and Cu(643)^R (Right), as calculated with DFT using PBE-D2

The calculation using the PBE-D2 functional overbinds R-3MCHO on Cu(221) and Cu(643)^R as on Cu(111). The TPD data indicated adsorption energies of −1.31 eV and −1.45 eV on Cu(221) and Cu(643)^R, respectively, while the PBE-D2 calculation predicted the adsorption energies of −1.50 eV and −1.55 eV on the same two surfaces. On Cu(221), R-3MCHO adsorbed along the bottom of the step with the oxygen atom sitting between two adjacent Cu atoms in the step edge. The cyclohexane ring lies parallel to the terrace, and the side with the methyl group leans towards the terrace. On Cu(643)R, the oxygen atom sits within the kinked site bound between two adjacent atoms in the straight step edge while the cyclohexane ring tilts away from the kink site. Figure 4.4 shows the differences between the adsorption energy on Cu(111) and the adsorption energies on Cu(221), Cu(322), and Cu(643)^R. For each DFT-D method, the difference was calculated by subtracting the adsorption energy of R-3MCHO on Cu(111) from its adsorption energy on the other surfaces. Figure 4.4 also compared our calculated difference to energy differences reported by Bhatia and Sholl.[9] Both PBE and PBE-D2 show larger adsorption energy differences than the experimental values.

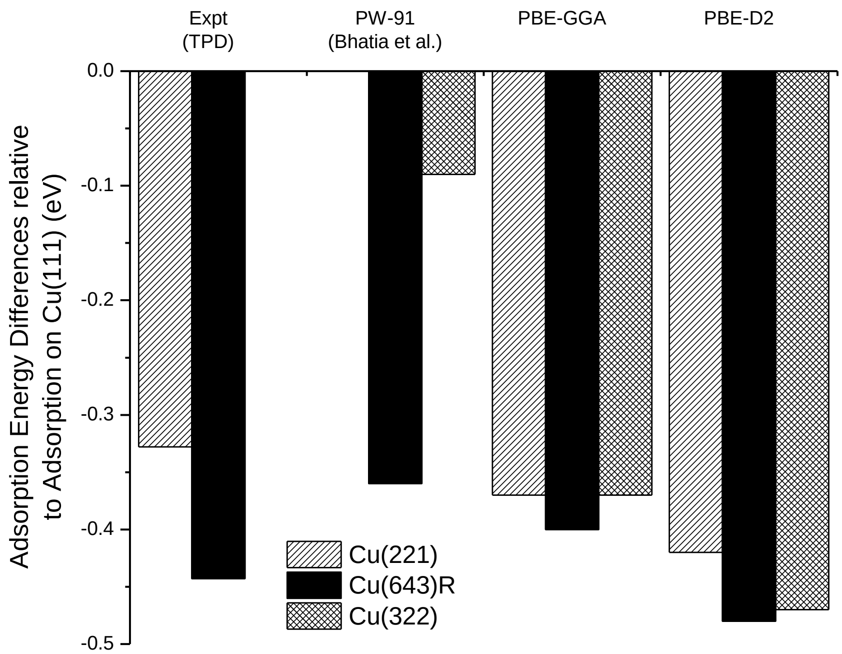

Figure 4.4: R-3MCHO adsorption energy differences between Cu(111) and stepped/kinked Cu surfaces for TPD, PW-91, PBE-GGA, and PBE-D2.

While our PBE calculated energy differences between Cu(111) and kinked Cu surface agreed with those reported by Bhatia and Sholl, our calculation showed a significantly different adsorption energy difference between Cu(111) and the stepped Cu surface. We attempted to understand this discrepancy by calculating the adsorption of R-3MCHO on Cu(322). The calculation indicated a difference of 0.28 eV between our calculated adsorption energy and those reported by Bhatia and Sholl.[9] Calculation on Cu(111) and Cu(221) using PW-91 also indicated an adsorption energy stronger than those reported by Bhatia and Sholl. The consistency of our calculated adsorption energy between Cu(221) and Cu(322) and the agreement between our calculated Cu(221) and the experimental TPD data suggest a possible inaccuracy in the earlier result reported by

Bhatia and Sholl. TPD indicated a larger adsorption energy difference of 0.11 eV between Cu(221) and Cu(643)^R than the difference predicted by our calculations. The PBE-GGA and PBE-D2 calculation showed a difference of only 0.03 eV and 0.06 eV between the two surfaces. While it is clear that dispersion corrected methods such as PBE-D2 can account for part of the dispersion forces, they failed to calculate the absolute binding energies for the range of surface we studied due to its inability to accurately account for parts of the exchange and correlation functional. Nonetheless, the method was able to achieve a useful comparison between adsorption on low and high Miller index Cu surfaces.

4.3.4 Adsorption on reconstructed Cu(110)

We attempted to address the experimental and simulated adsorption energy discrepancy for R-3MCHO adsorption on Cu(100) and Cu(110). Reexamination of the TPD data in Figure 4.1 shows the 3MCHO desorbs from Cu(110) at ~110 K above that of Cu(111) and Cu(100). The ~340 K desorption temperature on Cu(110) was much closer to the desorption temperature of 345 K observed for Cu(221). It was also similar to the desorption temperature of 3MCHO from the straight step of Cu(643)R. This suggested that Cu(110) behaves more like a step edge than a flat terrace. Scanning tunneling microscope (STM) and TPD study of R-3MCHO adsorption on Cu(533) and Cu(221) at elevated temperature showed an adsorbate induced reconstruction on these stepped edges.[38] We therefore investigated possible surface reconstructions in which Cu(110) was transformed into a more stepped surface. FCC Pt naturally undergoes a (2 × 1) missing row reconstruction where every other row of the (110) ridge is removed.[21-23] Furthermore, Raval et al. reported that the adsorption of CO induced a (2 × 1) missing row reconstruction on the Pd(110).[39] While Cu(110) does not undergo this reconstruction naturally, the study used this simple reconstruction to test our hypothesis. R-3MCHO was found to have an adsorption energy of −1.55 eV on the (2 × 1) missing row reconstructed Cu(110). Accounting for the energy required for the surface reconstruction, the R-3MCHO has an effective adsorption energy of −1.37 eV with respect to clean unreconstructed Cu(110). As shown in Figure 4.5, the calculated effective adsorption energy of 3MCHO on the reconstructed Cu(110) surface also overbinds the adsorbate to the surface. This overbinding was consistent with what we have observed on the other Cu surfaces.

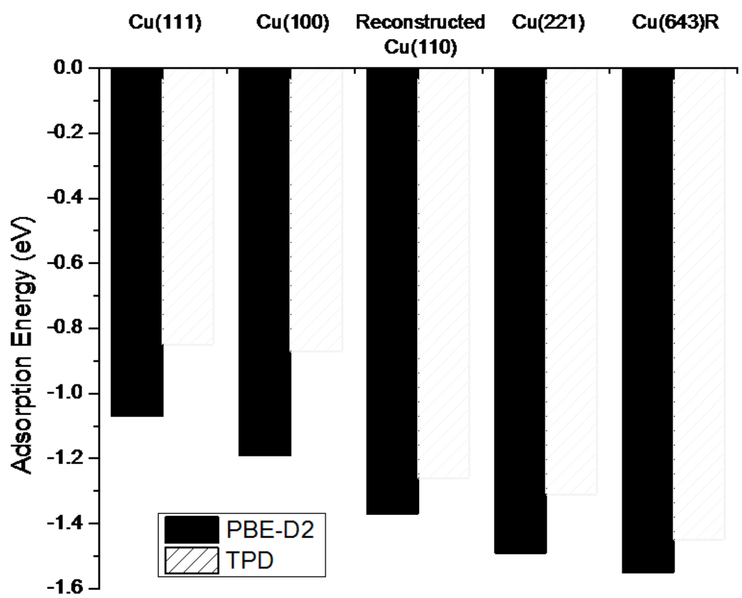

Figure 4.5: Adsorption energy of the most preferred configurations of R-3MCHO on the different Cu surfaces.

While it did not give the correct absolute binding energy, the reconstructed Cu(110) achieved a better agreement with the trends of adsorption energy observed in experimental study for the different surfaces. The presence of the consistent overbinding was also consistent with observation made on R-3MCHO adsorption on different Cu surfaces, and it helped to support the hypothesis of a possible adsorbate induced surface reconstruction on Cu(110). Additional studies will be necessary to determine the exact mechanism and structure of this reconstruction.

4.4 Conclusions

The study examined three different dispersion corrected DFT methods to model R-3MCHO adsorption on low Miller index Cu surfaces. All three methods show an overbinding of R-3MCHO to the surface to varying degrees, and none of them was able to achieve a quantitative agreement with TPD results. This significant weakness made it difficult to examine minute surface-adsorbate and adsorbate-adsorbate interactions. While PBE-B88 performed better than PBE-D2 and PBE-B86, the overall improvement was small. Adsorption calculations on the stepped Cu(221) and the kinked $Cu(643)^R$ using PBE-D2 indicated a similar overbinding of R-3MCHO. However, a qualitative agreement between PBE-D2 and TPD results was observed for adsorption energy differences between R-3MCHO adsorption on Cu(111), Cu(221), and $Cu(643)^R$. Comparison among the three low Miller index Cu surfaces had shown a discrepancy between TPD observations and DFT calculations for Cu(110). DFT calculation employing the (2×1) missing row reconstructed Cu(110) was able to reduce this discrepancy pointing to a possible surface reconstruction. The exact surface reconstruction, however, would require additional experimental observations.

4.5 References

1. Grimme, S., Accurate description of van der Waals complexes by density functional theory including empirical corrections. *Journal of Computational Chemistry* **2004,** *25* (12), 1463-1473.

2. Grimme, S., Semiempirical GGA-type density functional constructed with a long-range dispersion correction. *Journal of Computational Chemistry* **2006,** *27* (15), 1787-1799.

3. Becke, A. D., Density functional calculations of molecular bond energies. *The Journal of Chemical Physics* **1986,** *84* (8), 4524.

4. Becke, A. D., On the large-gradient behavior of the density functional exchange energy. *The Journal of Chemical Physics* **1986,** *85* (12), 7184.

5. Klimeš, J.; Bowler, D. R.; Michaelides, A., Chemical accuracy for the van der Waals density functional. *Journal of Physics: Condensed Matter* **2010,** *22* (2), 022201.

6. Becke, A. D., Density-functional exchange-energy approximation with correct asymptotic behavior. *Physical Review A* **1988,** *38* (6), 3098-3100.

7. Klimeš, J.; Bowler, D.; Michaelides, A., Van der Waals density functionals applied to solids. *Physical Review B* **2011,** *83* (19).

8. Huang, Y., *Adsorption of Chiral Molecules on Naturally Chiral Surfaces and Chirally Templated Surfaces*. Carnegie Mellon University: 2008.

9. Bhatia, B.; Sholl, D. S., Characterization of enantiospecific chemisorption on chiral Cu surfaces vicinal to Cu(111) and Cu(100) using density functional theory. *The Journal of Chemical Physics* **2008,** *128* (14), 144709.

10. McNellis, E. R.; Meyer, J.; Reuter, K., Azobenzene at coinage metal surfaces: Role of dispersive van der Waals interactions. *Physical Review B* **2009,** *80* (20), 205414.

11. Fosser, K.; Nuzzo, R.; Bagus, P.; Woll, C., The Adsorption of Cyclopropane and Cyclohexane on Cu(111) : An Experimental and Theoretical Investigation on the Nature of the CH-Metal Interaction. *Angewandte Chemie International Edition* **2002,** *41* (10), 1735-1737.

12. Xi, M.; Yang, M. X.; Jo, S. K.; Bent, B. E.; Stevens, P., Benzene adsorption on Cu(111): Formation of a stable bilayer. *The Journal of Chemical Physics* **1994,** *101* (10), 9122-9131.

13. Kresse, G.; Hafner, J., Ab initio molecular-dynamics for liquid-metals. *Physical Review B* **1993,** *47* (1), 558-561.

14. Kresse, G.; Hafner, J., Ab initio molecular-dynamics simulation of the liquid-metal–amorphous-semiconductor transition in germanium. *Physical Review B* **1994,** *49* (20), 14251-14269.

15. Kresse, G.; Furthmuller, J., Efficiency of ab-initio total energy calculations for metals and semiconductors using a plane-wave basis set. *Comput. Mater. Sci.* **1996,** *6* (1), 15-50.

16. Kresse, G.; Furthmuller, J., Efficient iterative schemes for ab initio total-energy calculations using a plane-wave basis set. *Physical Review B* **1996,** *54* (16), 11169-11186.

17. Perdew, J. P.; Burke, K.; Wang, Y., Generalized gradient approximation for the exchange-correlation hole of a many-electron system. *Physical Review B* **1996,** *54* (23), 16533-16539.

18. Perdew, J. P.; Burke, K.; Ernzerhof, M., Generalized gradient approximation made simple. *Physical Review Letters* **1997,** *78* (7), 1396-1396.

19. Blochl, P. E., Projector Augmented-Wave Method. *Physical Review B* **1994,** *50* (24), 17953-17979.

20. Kresse, G.; Joubert, D., From ultrasoft pseudopotentials to the projector augmented-wave method. *Physical Review B* **1999,** *59* (3), 1758-1775.

21. Adams, D. L.; Nielsen, H. B.; Van Hove, M. A.; Ignatiev, A., LEED study of the Pt(110)-(1 $\times$2) surface. *Surf Sci* **1981,** *104* (1), 47-62.

22. Niehus, H., Analysis of the Pt(110)-(1 $\times$2) surface reconstruction. *Surf Sci* **1984,** *145* (2–3), 407-418.

23. Blakely, D. W.; Somorjai, G. A., The stability and structure of high miller index platinum crystal surfaces in vacuum and in the presence of adsorbed carbon and oxygen. *Surf Sci* **1977,** *65* (2), 419-442.

24. Horvath, J.; Koritnik, A.; Kamakoti, P.; Sholl, D.; Gellman, A. J., Enantioselective Separation on a Naturally Chiral Surface. *Journal of American Chemical Society* **2004,** *126*, 14988-14994.

25. Huang, Y.; Gellman, A. J., Enantiospecific Adsorption of (R)-3-Methylcyclohexanone on Naturally Chiral Cu(531) R&S Surfaces. *Catalysis Letters* **2008,** *125* (3-4), 177-182.

26. Horvath, J.; Gellman, A. J., Enantiospecific desorption of chiral compounds from chiral Cu(643) and achiral Cu(111) surfaces. *Journal of American Chemical Society* **2001,** *124* (10), 2384-2392.

27. Huang, Y.; Gellman, A., Enantiospecific Adsorption of (R)-3-Methylcyclohexanone on Naturally Chiral Surfaces Vicinal to Cu(110). *Topics in Catalysis* **2011,** *54* (19), 1403-1413.

28. Gellman, A. J.; Horvath, J. D.; Buelow, M. T., Chiral single crystal surface chemistry. *Journal of Molecular Catalysis A: Chemical* **2001,** *167* (1–2), 3-11.

29. Horvath, J.; Gellman, A., Naturally Chiral Surfaces. *Topics in Catalysis* **2003,** *25* (1-4), 9-15.

30. Horvath, J. D.; Gellman, A. J., Enantiospecific Desorption of Chiral Compounds from Chiral Cu(643) and Achiral Cu(111) Surfaces. *Journal of the American Chemical Society* **2002,** *124* (10), 2384-2392.

31. Jenkins, S. J.; Pratt, S. J., Beyond the surface atlas: A roadmap and gazetteer for surface symmetry and structure. *Surface Science Reports* **2007,** *62* (10), 373-429.

32. Van Hove, M. A.; Somorjai, G. A., A new microfacet notation for high-Miller-index surfaces of cubic materials with terrace, step and kink structures. *Surf Sci* **1980,** *92* (2–3), 489-518.

33. Redhead, P. A., Thermal desorption of gases. *Vacuum* **1962,** *12* (4), 203-211.

34. Lei, R. Z.; Gellman, A. J.; Koel, B. E., Desorption energies of linear and cyclic alkanes on surfaces: anomalous scaling with length. *Surf Sci* **2004,** *554* (2–3), 125-140.

35. Horvath, J.; Baker, L.; Gellman, A. J., Enantiospecific Orientation of R-3-Methycyclohexanone on the Chiral $Cu(643)^{R/S}$ Surfaces. *J. Phys. Chem. C* **2008,** *112* (20), 7.

36. Grimme, S.; Antony, J.; Ehrlich, S.; Krieg, H., A consistent and accurate ab initio parametrization of density functional dispersion correction (DFT-D) for the 94 elements H-Pu. *The Journal of Chemical Physics* **2010,** *132* (15), 154104.

37. Witte, G.; Lukas, S.; Bagus, P. S.; Wöll, C., Vacuum level alignment at organic/metal junctions: “Cushion” effect and the interface dipole. *Applied Physics Letters* **2005,** *87* (263502), 1-3.

38. Zhao, X.; Perry, S. S.; Horvath, J.; Gellman, A. J., Adsorbate induced kink formation in straight step edges on Cu(533) and Cu(221). *Surf Sci* **2004,** *563* (1-3), 217-224.

39. Raval, R.; Haq, S.; Harrison, M. A.; Blyholder, G.; King, D. A., Molecular adsorbate-induced surface reconstruction: CO/Pd{110}. *Chem. Phys. Lett.* **1990,** *167* (5), 391-398.

CHAPTER 5

INSIGHT INTO THE IMPACT OF HETEROATOMS ON METHANOL SYNTHESIS OVER STEPPED AND KINKED COPPER SURFACES

5.1 Introduction

Methanol is a highly sought after commodity chemical with applications in transportation and chemical feedstocks. Its global demand exceeds 80 million tons/year.[1] Industrially, methanol is synthesized using mixtures of H_2, CO_2, and CO at elevated temperature (400 – 600 K) and pressure (50 – 100 atm) with a Cu/ZnO/Al_2O_3 catalyst.[2-5] With the advancement in carbon capture technology and demand for greenhouse gas mitigation, there has been growing interest in using captured CO_2 as a potential feed for methanol synthesis.[3, 5-10] This, in part, drives a demand for developing a strategy for the rational design of heterogeneous catalysts for methanol synthesis.

One major roadblock towards this strategy lies in the complexity of catalyst's surface structures and its impact on reaction mechanisms. While metallic Cu is generally accepted to be a structure sensitive catalyst, the exact mechanism and impact are uncertain. Several recent studies have begun to examine these effects.[3-5, 11] Behrens et al. proposed that small amounts of a Cu surface, activated by the presence of Zn heteroatoms, generate the majority of catalytic activity during methanol synthesis.[5]

Furthermore, their study has shown that the catalyst surface under relevant experimental conditions may be modelled as clean surface slabs.

Methanol synthesis on Cu has been studied under various experimental conditions with varying level of computational details.[2-5, 9-10, 12-20] While earlier computational studies examined the impact of surface structures[4, 9, 21] and heteroatoms[22-23], few studies have examined the combined impact of heteroatoms and Cu surface structures. There are numerous proposed mechanisms for the synthesis of methanol from CO_2.[4] Among the various proposed methanol synthesis pathway, this chapter will focus on the hydrogenation of formaldehyde to methanol via methoxide. Earlier studies have indicated these hydrogenation processes to be the rate limiting steps.[4, 13] An improved understanding of surface structure and heteroatom impact on these particular reactions may assist in the rational design of future catalysts.

Expanding upon the work of Behrens et al.,[5] we present a computational study of the impact of Zn and Zr promoters and surface structures of Cu on methanol synthesis under a typical methanol synthesis temperature of 400 – 600 K.[2-5] This study utilizes DFT to determine the positions and behaviors of Zn and Zr atoms on Cu surfaces and investigate the impact of these heteroatoms on the adsorption energy of MeOH synthesis intermediates and the reaction barrier for key reaction steps.

5.2 Methodology

Periodic DFT calculations were conducted with the Vienna *ab initio* simulation package.[24-28] The electron-election exchange and correlation interactions were described with the PW91-GGA functional.[29-30] Core-electron interactions were described with the projector augmented-wave (PAW) potential.[31-32] All calculations used a plane wave expansion cutoff of 500 eV. Structural optimization was performed by a conjugate gradient algorithm with a force stopping criterion of 0.03 eV/Å.

Surfaces were modeled as three equivalent Cu(111) layers with the bottommost layer immobilized. The Cu(111) surface was made up of a $p(5\times5)$ surface unit cell. The Cu(221) and Cu(211) were made up of a $p(2\times6)$ surface unit cell. The $Cu(643)^R$ was made up of a single surface unit cell. All four surfaces were examined using $3\times3\times1$ k-points. All surfaces had a vacuum spacing of at least 10 Å. Molecules were only adsorbed on one side of the slab. The reference molecule was placed in a $20\times20\times20$ Å cell and was sampled only at the Γ point. The surface adsorption energy was defined as,

$$E_{ads} = E_{total} - E_{\text{adsorbate,ref}} - E_{Surface} \quad (5.1)$$

where E_{total}, $E_{\text{adsorbate,ref}}$, $E_{Surface}$ are the total energy of the relaxed adsorption structure, the energy of the isolated reference molecule, and the clean surface energy, respectively.

Initial reaction pathways were optimized with a set of eight intermediate geometries, obtained by linear interpolation with a mixed internal and cartesian coordinate system using the approach implemented in the Opt'nPath suite.[33-34] The optimized geometries obtained by Opt'nPath suite were used as the initial geometries for nudged elastic band (NEB) calculation in VASP.[35-36]

5.3 Results and Discussion

5.3.1 Stability of Zinc and Zirconium Heteroatoms on Copper surface

The adsorption of methanol synthesis intermediates and the reaction pathways are sensitive to surface structure.[2-5, 9-10, 12-23] In this section we first investigate the behavior of an isolated heteroatoms on Cu steps to determine the most likely surface structures.

We then expanded our calculations to examine heteroatom behavior under likely experimental conditions and the possibility of cluster formation.

Figure 5.1 illustrates the preferred locations of individual Zn and Zr heteroatoms within the straight steps of Cu(221) and Cu(211). The energies were referenced to the most preferred structure for each heteroatom-surface combination. The empty circle indicates the energy cost if the heteroatom is adsorbed instead of substituted in the surface. On Cu(221), the Zn heteroatom was found to be most favorable when replacing the Cu on the top of the step while the Zr heteroatom preferred to embed in the sublayer below the top of the step. A similar behavior was observed on Cu(211) and Cu(643). The behavior of Zn heteroatom was consistent with the model assumed by Behren et al.[5]

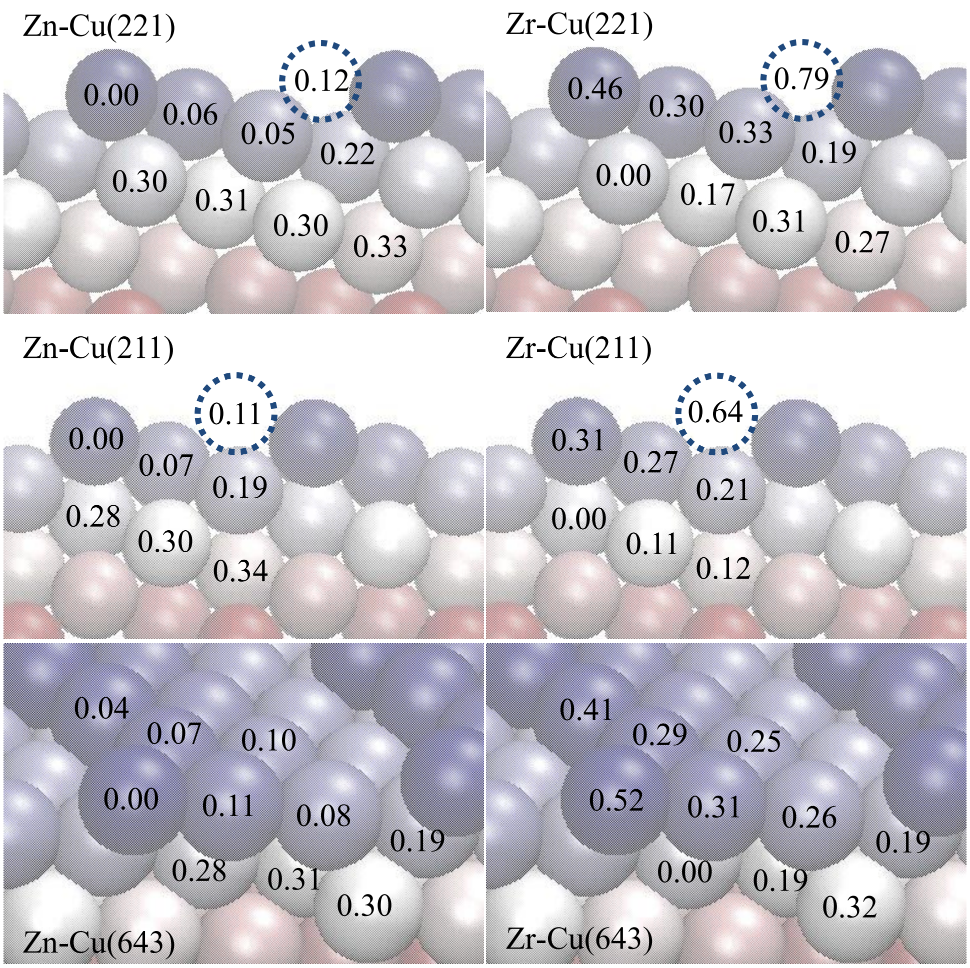

Figure 5.1: Relative energy cost of Zn or Zr replacement modification on Cu(221) and Cu(211). All energies are reported in eV and are referenced to the most stable heteroatom position modification. The blue dashed circle indicated the relative energy cost of an adsorbed Zn or Zr.

It was also noted that all reported energies for Zr with the exception of adsorbed Zr were more favorable than Zr embedded within the bulk Cu metal. This observation is supported by previous work. While both Ruban et al.[37] and Nilekar et al.[38] reported a strong segregation between Zr and Cu on low-index surfaces, Han et al. was uncertain if Zr and Cu favored segregation or antisegregation on the stepped edges.[39] Our calculations here implied a limited segregation between Zr and Cu on the step edge where Zr is segregated to a near-surface location but not directly on the exposed surface. The preferred embedded position for Zr, in order, is the sublayer below the top surface, the exposed top surface, and the bulk material been the least favorable position. Since Zr was known to bind strongly with oxygen atoms and hydroxyl groups that are likely to be present under experimental conditions, we investigated whether the presence of hydroxyl group impacted the preferred location of Zr on Cu steps. We calculated the relative adsorption energy of hydroxyl with Zr replacing different surface Cu atoms. As shown in Figure 5.2, the most favorable geometry was obtained when Zr was placed on the top of the step. This suggested that while an isolated Zr heteroatom will preferentially embedded in the sublayer, the Zr-O interaction was thermodynamically favorable enough to overcome the energy needed to pull the Zr heteroatom to the top of the step edge. Since oxygen atoms and hydroxyl groups are abundant under experimental conditions, all subsequent calculations assumed that the Zr heteroatom resided on the top of the step. It was noted that the adsorption energies of hydroxyl group on Cu(211) and Cu(221) differs by more than 1 eV. This was due to the differences in reference state. When Zr heteroatom was embedded at the most stable position on Cu(211), the large size of the Zr heteroatom made it partially expose to the surface. This had allowed the hydroxyl group to partially interact with the exposed Zr heteroatom. However, on the Cu(221), the Zr heteroatom was entirely covered by surface Cu atoms, and the hydroxyl group was only able to interact with the surface Cu atoms. Thus, the large energy differences between hydroxyl adsorption on Cu(211) and Cu(221) was due to the hydroxyl in the Cu(211) reference state been able to interact with Zr atom. A similar calculation was carried out for Zn heteroatom. As expected, the Zn heteroatom remained most favorable at the top of the stepped edge in the presence of hydroxyl groups.

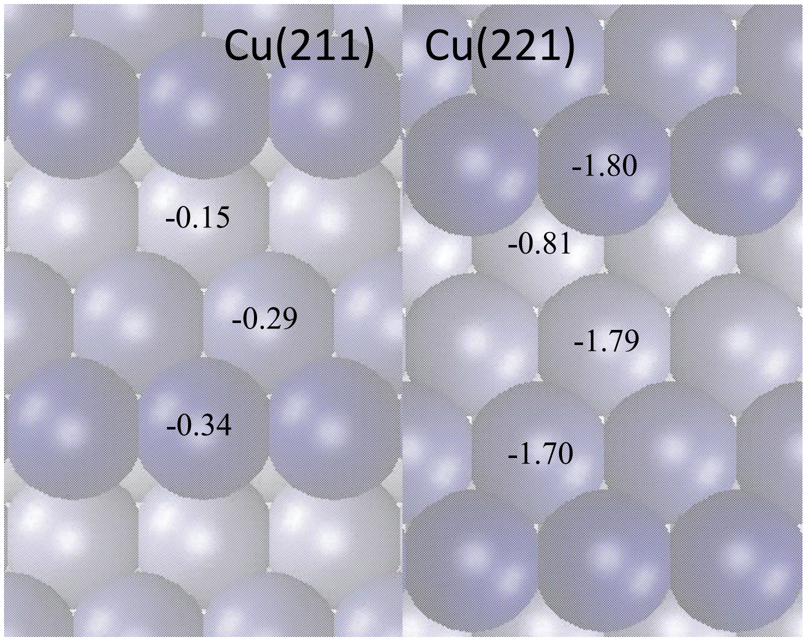

Figure 5.2: Most favorable hydroxyl adsorption energies with Zr replacing different surface Cu atoms. All energies are reported in eV. The values are referenced to the most favorable hydroxyl adsorption energies with Zr embedded in the most favorable position identified in Figure 5.1.

Since the surface coverage of heteroatoms was known to influence the overall activity of a catalyst and the highest turnover frequency for methanol formation was achieved with a surface Zn coverage around 0.2,[15, 40] we studied the likelihood of heteroatom clustering on the Cu surfaces. We considered a cluster of two heteroatoms embedded next to each other. The position of the first heteroatom was determined from the earlier calculation as the most preferred substitution location under experimental condition. For both Zn and Zr, this was determined to be at the top of the stepped or kinked position. The secondary heteroatom may take the position of any Cu atom adjacent to the first heteroatom. The cluster energy, reported in Table 5.1, was then calculated as the energy difference between a cluster of two heteroatoms and two separated heteroatom both embedded in the most preferred location. A negative energy indicated a preference towards cluster formation. Several clustering geometries was examined, and only the energy for most favorable cluster was reported.

Table 5.1: Energy cost of two heteroatoms clustered on the surface. The energies are referenced to two isolated promoter within the most preferred replacement location.

Heteroatom	Surface	Cluster Energy (eV)
Zn	Cu(211)	0.06
	Cu(221)	0.20
	Cu(643)	0.05
Zr	Cu(211)	0.17
	Cu(221)	0.08
	Cu(643)	-0.01

The reported cluster energy for Zn heteroatoms indicated that Zn preferred to be isolated from each other. However, it should be noted that these cluster energy was obtained at 0 K. If we assumed a Boltzmann probability distribution of,

$$\frac{F(Clustered)}{F(Individual)} = exp\left(\frac{\Delta E}{kT}\right) \tag{5.2}$$

where k is the Boltzmann constant and $\boldsymbol{\Delta E}$ is the cluster energy. Using this probability distribution, the small energy differences of 0.06 eV on Cu(211) suggested that as much as 25% of the steps may contained clustered Zn heteroatoms under typical methanol synthesis temperature of 400-600 K. Based on the cluster energy, it is more likely to observe Zn clusters on Cu(643) and Cu(211) than Cu(221). The differences between step has been observed on other surfaces.[41] A similar behavior was observed for Zr on Cu(211) and Cu(221), although Zr cluster was more likely to form on Cu(221) instead of on Cu(211). It was important to note that without the presence of an additional hydroxyl group, the second Zr atom preferred to substitute in the sublayer instead of the step. The opposite also held true where the presence of a secondary hydroxyl group made it more favorable for the second Zr heteroatom to substitute at the top of the step. Since hydroxyl groups are readily available under experimental conditions, only the latter scenario was considered in our calculations. The cluster energy for Zr on Cu(643) was interesting in that it resulted in a 0.01 eV preference towards clustering of Zr heteroatoms. An energy difference of 0.01 eV is small under the typical methanol synthesis temperature of 400-600 K. As such, it was only reasonable to conclude that it is likely to observe both isolated and clustered Zr on Cu(643).

5.3.2 Adsorption and hydrogenation of formaldehyde and methoxide on Cu stepped edges

We investigated the reaction pathway for the hydrogenation of formaldehyde and methoxide. We first focused on the impact of single **M** heteroatom substitution in the Cu step edge, where a single **M** atom modified Cu(*hkl*) surface is denoted as MCu(hkl). For each surfaces, the adsorption geometries for formaldehyde, methoxide, and methanol were obtained through a systematic examination of all likely surface adsorption geometries. Additional attention was given to adsorption geometries around the heteroatoms. Multiple NEB pathways and transition states (TS) were examined with the Opt'nPath suite.[33-34] To facilitate the NEB calculations, the surfaces were immobilized during the calculations. The final TS were converged with NEB. Only the most favorable pathways and TS are reported here. The reaction pathways on all the surfaces are illustrated in Figure 5.3.

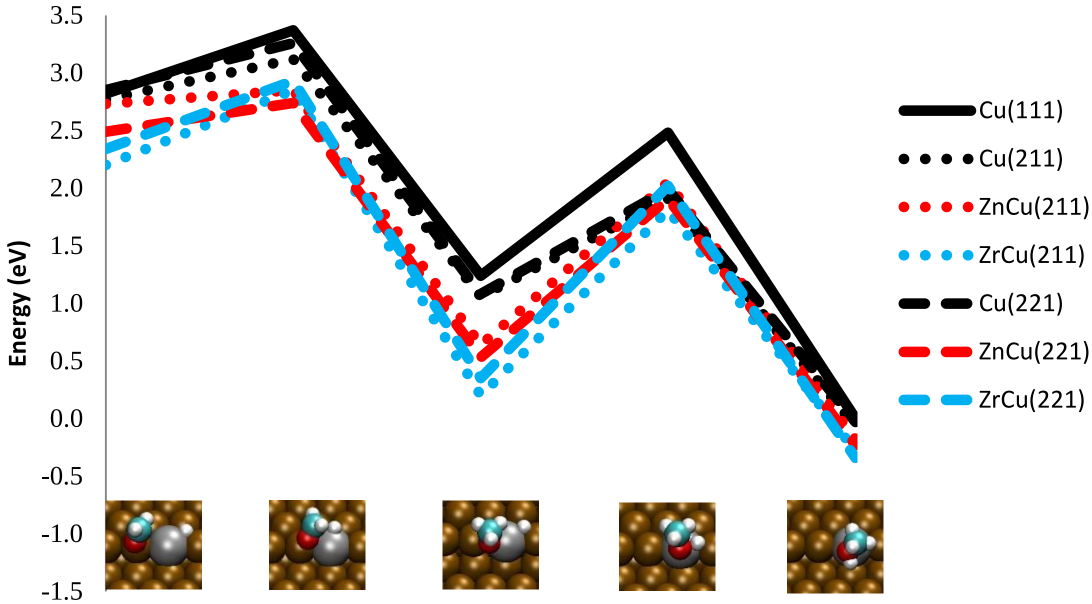

Figure 5.3: Energy diagram for the hydrogenation of formaldehyde and methoxide on Cu(111), Cu(211), Cu(221), and the heteroatom modified stepped edge. All energies are referenced to methanol on Cu(111). The inset pictures illustrated each step of the reaction for Zn promoted Cu(211).

Three particulars were immediately noticeable. One, the presence of a Zn or Zr heteroatom significantly increased the binding energy of formaldehyde and methoxide. These increases are directly attributed to the binding of formaldehyde and methoxide to the Zn and Zr heteroatom which were stronger than the binding of formaldehyde and methoxide to Cu atoms. Two, the Zn modified Cu surfaces had lower activation barrier for the hydrogenation of formaldehyde than the clean and Zr modified Cu surfaces. Three, there were noticeable differences between the reaction on Cu(221) and Cu(211) steps. From a qualitative perspective, our results were in agreement with results obtained by Behrens et al.[5] The usage of different functional between their calculations and ours contributed to the observed differences between the two set of results. We noted that while the presence of heteroatoms increases the adsorption energy of formaldehyde and methoxide, it did not change the overall shape of the energy diagram. The adsorption of formaldehyde was still significantly weaker than methoxide, and the reaction barrier for the hydrogenation of formaldehyde was lower than the hydrogenation of methoxide. These general features have been reported before.[4-5, 21] The adsorption energy of all surface species and the reaction barriers are tabulated in Table 5.2. All relative reaction ratios were relative to reaction on Cu(111). The instantaneous reaction energetic compared the ratio between reaction rates and desorption rates can be estimated by,

$$r \approx \exp\left(\frac{-E_A - E_{ads}}{kT}\right) \tag{5.3}$$

where, E_A is the activation energy and E_{ads} is the adsorption energy. We assumed a typical methanol synthesis temperature of 500 K.[2-5] A value of r above one means the mechanism favors the reaction pathway over the desorption pathway. The reaction rates among the different surfaces were then further compared through a relative reaction ratio,

$$R_X = \frac{r_X}{r_{Cu(111)}} = \exp\left(\frac{-\Delta E_{X,ads} - \Delta E_{X,A}}{kT}\right) \tag{5.4}$$

where R_X is the relative reaction rate on surface X to reaction rate on Cu(111), $\Delta E_{X,ads}$ is the adsorption energy difference between the adsorbate on surface X and on Cu(111), and $\Delta E_{X,A}$ is the difference between the activation barriers for the reaction on surface X and Cu(111). We assumed the reverse reaction of hydrogenation of formaldehyde and methoxide were negligible. For the latter reaction, the hydrogenation of methoxide produces methanol which readily desorb from the surface. Since these reactions were carried out in sequence, the total selectivity, r_{tot}, and combined relative reaction ratio, $R_{X,tot}$, were the product of the selectivity and relative reaction ratio of the two reaction steps.

Table 5.2: Calculated adsorption energy, activation energy, and estimated reaction rate information for the hydrogenation of formaldehyde and methoxide on clean and modified Cu surfaces. All energies are given in eV. Adsorption energies are referenced to isolated adsorbate and H_2 in vacuum.

	Cu(111)	Cu(211)	Zn-Cu(211)	Zr-Cu(211)	Cu(221)	Zn-Cu(221)	Zr-Cu(221)
H_2CO + 2H	-0.20	-0.25	-0.29	-0.82	-0.17	-0.53	-0.68
Barrier H-H_2CO + H	0.55	0.35	0.12	0.71	0.41	0.25	0.64
H_3CO + H	-0.31	-0.49	-0.91	-1.35	-0.47	-1.02	-1.20
Barrier H_3CO-H	1.24	0.85	1.41	1.61	0.91	1.38	1.67
H_3COH	-0.22	-0.29	-0.40	-0.50	-0.25	-0.45	-0.56
r_{tot}	4.7E-13	3.7E-05	6.6E-04	3.6E-02	2.8E-07	1.7E-01	2.2E-04
$R_{x,tot}$	-	7.9E07	1.4E09	7.7E10	6.0E05	3.6E11	1.5E08

One main difference between Table 5.2 and Figure 5.3 was the change of reference state. Instead of referencing all adsorption energies to methanol on Cu(111), the adsorption energies reported in Table 5.2 were references to an isolated adsorbate and H_2. Using the Cu(211) as an example, the formaldehyde desorption energy, $E_{desorption} = -E_{adsorption}$, was 0.10 eV lower than the activation energy. This immediately suggested that formaldehyde was likely to desorb before reaction could take place. A similar prospect can be observed for the hydrogenation of methoxide to methanol. The desorption energy of methoxide was 0.36 eV lower than the activation barrier. Since desorption energies for both reactants were lower than the activation barriers, there is a strong preference towards desorption. However, if we considered the relative properties of Cu(211) and Cu(111), the relative reaction ratio, $R_{x,tot}$, of 7.9×10^7 suggested that it is far more favorable for the reaction to proceed on Cu(211) as opposed to on Cu(111).

Based on our calculations, the presence of heteroatoms has a significant impact on the adsorption energy and the activation barrier. On Cu(211), the presence of a single Zn heteroatom decreased the adsorption energy of formaldehyde and methoxide by 0.04 eV and 0.42 eV, respectively. On the other hand, it changed the activation energy by -0.23 eV and 0.56 eV, respectively. This led to a relative reaction ratio several orders of magnitude higher than the clean Cu surface – implying that the reactions were more likely to take place at the heteroatom modified steps. For the Zr modified surfaces, the Zr atom bonded very strongly with the O atom within formaldehyde and methoxide. This resulted in adsorption energies that were more than 0.5 eV stronger than the clean Cu surfaces. At the same time, the strong bond between the Zr and the adsorbate produced significantly higher activation barriers. Despite these increases in activation barriers, the Zr modified surfaces had the highest relative reaction ratios. This suggested that the increases in adsorption energies were the key contributor to the increased activity on heteroatom modified Cu surfaces.

While a similar trend between clean and heteroatom substituted stepped surface was observed on Cu(221), there were a noticeable differences in the reaction energetic. Both formaldehyde and methoxide adsorbed slightly weaker on Cu(221) than on Cu(211). At the same time, both hydrogenation steps required higher activation energies. The overall relative reaction ratio on Cu(221) was two orders of magnitude lower than that of Cu(211). This pointed to a clear activity differences between the two clean surfaces, and it suggested that heteroatoms may impact the steps differently. Similar differences in chemical properties between different step orientations were also reported for other FCC metals.[41-42] The presence of a Zn heteroatom on Cu(221) increased the binding energy of formaldehyde by 0.36 eV and methoxide by 0.55 eV. This was an increase of 0.34 eV and 0.09 eV relative to Zn modified Cu(211). The Zn heteroatom on Cu(221) also lowered the activation barrier of formaldehyde and methoxide by 0.16 eV and -0.47 eV, compared to 0.23 eV and -0.56 eV on Cu(211). Thus, the relative reaction ratio on Zn modified Cu(221) was two orders of magnitude higher than on Zn modified Cu(211). Thus, even though Cu(211) was more active than Cu(221), Zn heteroatoms have a greater impact on Cu(221), and Zn modified Cu(221) was more reactive than Zn modified Cu(211). The Zr heteroatom did not appear to have similar effect on Cu(221) as a Zn heteroatom. While Zr modified Cu(221) showed a lower activation energy and adsorption energy, the overall impact on Cu(221) was similar to its impact on Cu(211), and Zr modified Cu(221) shown lower activity than Zr modified Cu(211).

While adsorption behaviors and reaction energetics can be estimated by NEB calculations, the calculations were resource intensive. The examination of reaction energetics by NEB also required significant human input on likely TS and pathways. This made it difficult to examine large quantity of potential surface structures. It would be desirable if an estimation of the reaction energetics can be obtained without utilizing the NEB calculation. The Bell-Evans-Polanyi (BEP) principle was a promising candidate for this task.[43] BEP relationship has been show to predict simple elementary reaction step with reasonable accuracy.[44-46] Our calculations explored the possibility of using BEP relationship as a possible predictor of reaction energetics. The BEP relationship for the hydrogenation of formaldehyde and methoxide on the earlier surfaces is shown in Figure

5.4. The two dashed line designated the one standard error, 0.21 eV, of the activation energy. This was calculated using the differences between the calculated activation energy of each data point and the regression line predicted activation energy. Since one standard error of 0.21 eV was able to capture majority of the data point, it illustrated a strong fit of the regression line to the data point. The linear regression indicated a strong positive relationship, r = 0.8527, between the activation energy and ΔH, the differences between the energy of the product and the reactant. The reported r = 0.8527 was similar to values reported by Vojvodic et al. for adsorption on transitional metal oxide.[46] This implied that BEP relationship may be use as a reasonable approximation for the hydrogenation of formaldehyde and methoxide on stepped Cu surfaces.

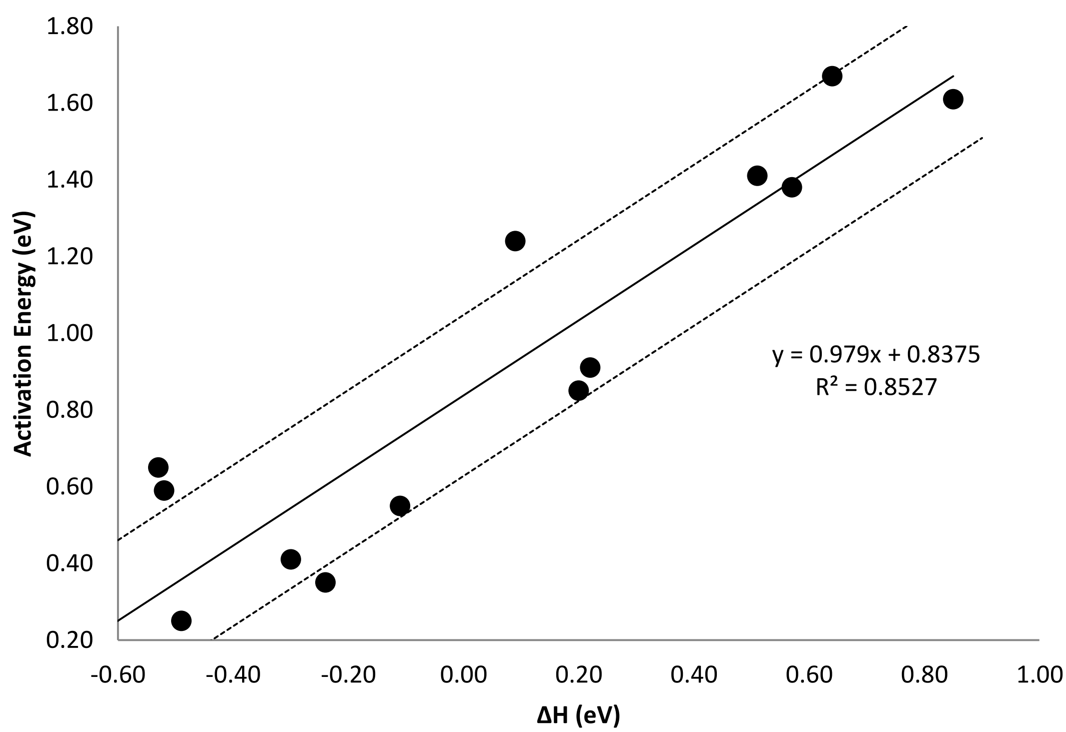

Figure 5.4: Calculated linear relationship between activation energy and ΔH for hydrogenation of formaldehyde and methoxide on the surfaces reported in Table 5.2. The dashed lines indicated the standard error in the activation energy.

Since our earlier surface calculations suggested a likely surface clustering of Zn heteroatom and other computational and experimental studies had indicated an impact of Zn coverage on rate of methanol synthesis,[14, 39] we carried out a similar examination of the impact of clustered Zn atom on the reaction energetics. The calculation used clustered Zn heteroatoms in which two Zn atoms are embedded next to each other along the stepped edge. This was identified by our earlier calculation as the most favorable Zn clustered and was identical to the model used by Behrens et al..[5] The adsorption energies of the surface species are listed in Table 5.3.

Table 5.3: Adsorption energies and activation barriers of formaldehyde, methoxide, and methanol on clustered Zn heteroatom on Cu(211). All energies are reported in eV. Adsorption energies were references to isolated adsorbates and H_2 in vacuum. The barriers were estimated using the BEP relationship.

	H_2CO+2H	Barrier H-H_2CO+H	H_3CO+H	Barrier H_3CO-H	H_3COH
Clustered ZnCu(211)	-0.68	0.72	-1.01	1.17	-0.41

Comparing to isolated Zn on the Cu(211) stepped edge, the clustered Zn structure increased the adsorption energy of formaldehyde and methoxide by 0.39 eV and 0.10 eV, respectively. With our current observation of a positive correlation between adsorption energy and relative reaction ratio, the increased in adsorption energies alone should indicated a likely increase in the relative reaction ratio. For this clustered Zn structure, the BEP relationship indicated an increase of 0.60 eV and -0.24 eV in the activation of formaldehyde and methoxide, respectively. The increase of 0.60 eV in the activation energy of formaldehyde was slightly unfavorable to the reaction ratio. Unlike the isolated Zn heteroatom, this increase meant the activation energy of formaldehyde was 0.04 eV higher than the desorption energy. While unfavorable, the gap is not large. The decreases of 0.24 eV in methoxide activation energy, however, proved to be instrumental in the expected increase in the reaction energetic. This decrease in activation energy lowered the energy differences between methoxide activation and desorption from 0.50 eV to 0.16 eV. The overall benefit was demonstrated in the calculated relative reaction ratio of 2.5×10^{10}, which was an order of magnitude higher than the isolated Zn heteroatom embedded surface. This suggests the Zn clusters could play a key role in the net activity of the catalysts, even though they are present in small numbers. Additional investigation into the impact of heteroatom cluster sizes and shapes in the future would provide further insight into adsorbate behavior on catalyst surfaces.

5.3.2 Adsorption and hydrogenation of formaldehyde and methoxide on kinked Cu edges

The conventional catalyst behavior noted that the kinked surface have higher reaction activity than the stepped surface. Since it is possible that a significant amount of reaction take places on kinked step sites, an examination of methanol synthesis on Cu would be incomplete without investigating the impact of heteroatoms on kinked surface. Our early calculations indicated that under experimental conditions, a single isolated heteroatom preferred to substitute the exposed kinked Cu atom. While earlier calculations also indicated a potential for clustering of Zr atoms on the kinked site, we first focused on the isolated heteroatom substitution of the exposed kinked Cu atom. Using this surface model, the DFT calculated adsorption energies and BEP estimated barrier can be found in Table 5.4.

Table 5.4: Adsorption energies and activation barriers of formaldehyde, methoxide, and methanol on clean and heteroatom substituted Cu(643). All energies are reported in eV. Adsorption energies were references to isolated adsorbates and H_2 in vacuum. The barriers were estimated using the BEP relationship.

	H_2CO+2H	Barrier H-H_2CO+H	H_3CO+H	Barrier H_3CO-H	H_3COH
Cu(643)	-0.51	-0.60	-1.98	2.51	-0.27
ZnCu(643)	-0.83	-0.50	-2.20	2.39	-0.61
ZrCu(643)	-0.92	-0.58	-2.37	2.49	-0.68

The adsorption energies for methoxide on these three surfaces were unexpected. While both formaldehyde and methanol shown slightly stronger adsorption than the stepped edge, the adsorption of methoxide on Cu(643) was more than 1 eV stronger than the stepped edge. Adsorption energy of ~2 eV suggested that methoxide formed a chemical bond with the surface. While it may be possible that methoxide formed a chemical bond between the O atom and the less coordinated kinked atom, it is difficult to explain why this was not also observed on the straight step edges examined above. The large methoxide adsorption energies also led to a negative BEP-estimated activation barrier for formaldehyde and a huge activation barrier for methoxide. More importantly, the negative activation energy indicated that formaldehyde will spontaneously react with surface H atom to form methoxide. The complexity of the reaction pathway on Cu(643) made it difficult to converge on a reasonable NEB pathway, so our calculations to date with this method cannot confirm whether a activation barrier exists for the hydrogenation of formaldehyde on Cu(643). However, it was noted that in several geometric relaxation calculations for formaldehyde, one of the neighboring adsorbed H atom formed a bond with the C atom, and a methoxide was formed in the final relaxed state. If we assumed a negative activation barrier for formaldehyde, then the hydrogenation of methoxide was the sole rate limiting steps. This appears to be consistent with experimental observations.[3,11] Ignoring the hydrogenation of formaldehyde, the relative reaction ratio for the hydrogenation of methoxide, Table 5.5, indicated that significant amount of reaction will take place on the kinked surface.

Table 5.5: Relative reaction ratio for the hydrogenation of methoxide on clean and single heteroatom substituted Cu stepped and kinked surfaces. All ratio were relative to reaction on Cu(111).

$R_{x,methoxide}$	Cu(211)	Cu(221)	Cu(643)
Clean	3.10E+05	5.26E+04	2.62E+07
Zn	1.39E+04	3.10E+05	6.89E+04
Zr	2.85E+06	2.70E+04	1.23E+07

These results, however, relied on activation barrier estimated by the BEP relationship. One possible complication was that the hydrogenation of formaldehyde to methoxide on the kinked surface was not an elementary step, and BEP was not suitable on the kinked site. Due to the ambiguity that was presented with a single embedded heteroatom, we did not consider the impact of cluster heteroatoms on Cu kinked edge. Additional detailed investigation into how heteroatom impacted the methanol synthesis pathway on kinked Cu surfaces in the future would be useful to shed light into this situation and helped gain better understanding of Cu catalyst behavior.

5.4 Conclusions

This chapter had examined the behavior of Zn and Zr heteroatom on Cu surfaces and their impacts on the hydrogenation of formaldehyde and methoxide. The model had determined that the Zn heteroatom preferential embedded at the top of the copper stepped edge while Zr heteroatom preferred to embed in the sublayer; however, the presence of hydroxyl group made it highly favorable for Zr heteroatom to embed at the top of the copper stepped edge as well. The presence of the Zn or Zr heteroatom increased the binding energy of reaction intermediates due to the adsorbates' preferences towards binding with these heteroatoms instead of the Cu atoms. The increased binding energy meant that the reactants were more likely to react towards the product rather than simply desorb from the surface. This accounts for the majority of the increase in overall observed reaction rates. While heteroatoms were less likely to cluster on the surface, the clustered Zn heteroatoms bind the intermediate much stronger than a single isolated Zn heteroatom. For Zn clustered step, this resulted in several order of magnitude increases in relative reaction ratio; thus, despite the fewer number of clustered site, significant amount of the reactions still take place on these surface structures. Different Cu step orientations produced slightly different surface structures and clustering probability. These structure differences led to a noticeable difference in the hydrogenation of formaldehyde and methoxide. Our calculations also showed that BEP can be used as an approximation for the hydrogenation of formaldehyde and methoxide on Cu stepped edge.

The calculated results for the hydrogenation of formaldehyde and methoxide on Cu kinked sites proved to be unexpected. The calculations indicated chemisorption of the reaction intermediates and a barrier-less hydrogenation of formaldehyde to methoxide. Further detailed investigation into adsorption and reaction energetic of methanol synthesis on Cu kinked site may provide insight into the unexpected behavior observed in this study.

5.5 References

1. Methanol Basics. http://www.methanol.org/Methanol-Basics.aspx.

2. Waugh, K. C., Methanol Synthesis. *Catalysis Today* **1992,** *15* (1), 51-75.

3. Rasmussen, P. B.; Holmblad, P. M.; Askgaard, T.; Ovesen, C. V.; Stoltze, P.; Nørskov, J. K.; Chorkendorff, I., Methanol synthesis on Cu(100) from a binary gas mixture of CO_2 and H_2. *Catalysis Letters* **1994,** *26* (3-4), 373-381.

4. Grabow, L. C.; Mavrikakis, M., Mechanism of Methanol Synthesis on Cu through CO_2 and CO Hydrogenation. *ACS Catalysis* **2011,** *1* (4), 365-384.

5. Behrens, M.; Studt, F.; Kasatkin, I.; Kühl, S.; Hävecker, M.; Abild-Pedersen, F.; Zander, S.; Girgsdies, F.; Kurr, P.; Kniep, B.-L.; Tovar, M.; Fischer, R. W.; Nørskov, J. K.; Schlögl, R., The Active Site of Methanol Synthesis over Cu/ZnO/Al_2O_3 Industrial Catalysts. *Science* **2012,** *336* (6083), 893-897.

6. Pan, W.; Song, C., In-Situ Study of Carbon Deposition during CO_2 Reforming of Methane for Synthesis Gas Production, Using the Tapered Element Oscillation Microbalance. In *Carbon Dioxide as Chemical Feedstock*, Wiley-VCH Verlag GmbH & Co. KGaA: 2010; pp 249-266.

7. Ballivet-Tkatchenko, D.; Dibenedetto, A., Synthesis of Linear and Cyclic Carbonates. In *Carbon Dioxide as Chemical Feedstock*, Wiley-VCH Verlag GmbH & Co. KGaA: 2010; pp 169-212.

8. Aresta, M., Carbon Dioxide: Utilization Options to Reduce its Accumulation in the Atmosphere. In *Carbon Dioxide as Chemical Feedstock*, Wiley-VCH Verlag GmbH & Co. KGaA: 2010; pp 1-13.

9. Yang, Y.; Evans, J.; Rodriguez, J. A.; White, M. G.; Liu, P., Fundamental studies of methanol synthesis from CO2 hydrogenation on Cu(111), Cu clusters, and Cu/ZnO(0001). *Physical Chemistry Chemical Physics* **2010,** *12* (33), 9909.

10. Yoshihara, J.; Campbell, C. T., Methanol synthesis and reverse water-gas shift kinetics over Cu(110) model catalysts: Structural sensitivity. *Journal of Catalysis* **1996,** *161* (2), 776-782.

11. Greeley, J.; Mavrikakis, M., Methanol Decomposition on Cu(111): A DFT Study. *Journal of Catalysis* **2002,** *208* (2), 291-300.

12. Klier, K., Methanol Synthesis. In *Advances in Catalysis*, D.D. Eley, H. P.; Paul, B. W., Eds. Academic Press: 1982; Vol. Volume 31, pp 243-313.

13. Edwards, J. F.; Schrader, G. L., Insitu fourer-transform infared study of methanol synthesis on mixed metal-oxide catalysts. *Journal of Catalysis* **1985,** *94* (1), 175-186.

14. Rasmussen, P. B.; Kazuta, M.; Chorkendorff, I., Synthesis of methanol from a mixture of H_2 and CO_2 on Cu(100). *Surf Sci* **1994,** *318* (3), 267-380.

15. Fujitani, T.; Nakamura, I.; Uchijima, T.; Nakamura, J., The kinetics and mechanism of methanol synthesis by hydrogenation of CO_2 over a Zn-deposited Cu(111) surface. *Surf Sci* **1997,** *383* (2-3), 285-298.

16. Nerlov, J.; Chorkendorff, I., Methanol Synthesis from CO_2, CO, and H_2 over Cu(100) and Ni/Cu(100). *Journal of Catalysis* **1999,** *181* (2), 271-279.

17. Nerlov, J.; Sckerl, S.; Wambach, J.; Chorkendorff, I., Methanol synthesis from CO_2, CO and H_2 over Cu(100) and Cu(100) modified by Ni and Co. *Applied Catalysis A: General* **2000,** *191* (1–2), 97-109.

18. Tsai, Y. T.; Mo, X. H.; Goodwin, J. G., Synergy of Components in CuZnO and CuZnO/Al_2O_3 on Methanol Synthesis: Analysis at the Site Level by SSITKA. *Topics in Catalysis* **2012,** *55* (11-13), 757-770.

19. Frenzel, J.; Kiss, J.; Nair, N. N.; Meyer, B.; Marx, D., Methanol synthesis on ZnO from molecular dynamics. *Phys. Status Solidi B-Basic Solid State Phys.* **2013,** *250* (6), 1174-1190.

20. Graciani, J.; Mudiyanselage, K.; Xu, F.; Baber, A. E.; Evans, J.; Senanayake, S. D.; Stacchiola, D. J.; Liu, P.; Hrbek, J.; Sanz, J. F.; Rodriguez, J. A., Highly active copper-ceria and copper-ceria-titania catalysts for methanol synthesis from CO_2. *Science* **2014,** *345* (6196), 546-550.

21. Zhao, Y.-F.; Yang, Y.; Mims, C.; Peden, C. H. F.; Li, J.; Mei, D., Insight into methanol synthesis from CO_2 hydrogenation on Cu(111): Complex reaction network and the effects of H_2O. *Journal of Catalysis* **2011,** *281* (2), 199-211.

22. Sahibzada, M., Pd-Promoted Cu/ZnO Catalyst Systems for Methanol Synthesis From CO_2/H_2. *Chemical Engineering Research and Design* **2000,** *78* (7), 943-946.

23. Morikawa, Y.; Iwata, K.; Terakura, K., Theoretical study of hydrogenation process of formate on clean and Zn deposited Cu(111) surfaces. *Applied Surface Science* **2001,** *169–170* (0), 11-15.

24. Kresse, G.; Hafner, J., Ab initio molecular-dynamics for liquid-metals. *Physical Review B* **1993,** *47* (1), 558-561.

25. Kresse, G.; Hafner, J., Ab initio molecular-dynamics simulation of the liquid-metal–amorphous-semiconductor transition in germanium. *Physical Review B* **1994,** *49* (20), 14251-14269.

26. Kresse, G.; Furthmuller, J., Efficiency of ab-initio total energy calculations for metals and semiconductors using a plane-wave basis set. *Comput. Mater. Sci.* **1996,** *6* (1), 15-50.

27. Kresse, G.; Furthmuller, J., Efficient iterative schemes for ab initio total-energy calculations using a plane-wave basis set. *Physical Review B* **1996,** *54* (16), 11169-11186.

28. Sholl, D.; Steckel, J., *Density functional theory : a practical introduction*. John Wiley & Sons: Hoboken, 2009.

29. Perdew, J. P.; Chevary, J. A.; Vosko, S. H.; Jackson, K. A.; Pederson, M. R.; Singh, D. J.; Fiolhais, C., Atoms, molecules, solids, and surfaces: Applications of the generalized gradient approximation for exchange and correlation. *Physical Review B* **1992,** *46* (11), 6671-6687.

30. Perdew, J. P.; Chevary, J. A.; Vosko, S. H.; Jackson, K. A.; Pederson, M. R.; Singh, D. J.; Fiolhais, C., Erratum: Atoms, molecules, solids, and surfaces: Applications of the generalized gradient approximation for exchange and correlation. *Physical Review B* **1993,** *48* (7), 4978-4978.

31. Blochl, P. E., Projector Augmented-Wave Method. *Physical Review B* **1994,** *50* (24), 17953-17979.

32. Kresse, G.; Joubert, D., From ultrasoft pseudopotentials to the projector augmented-wave method. *Physical Review B* **1999,** *59* (3), 1758-1775.

33. Weinan, E.; Ren, W. Q.; Vanden-Eijnden, E., String method for the study of rare events. *Physical Review B* **2002,** *66* (5).

34. Dayal, P.; Fleurat-Lessard, P. A chemist view on reaction path determination. http://perso.ens-lyon.fr/paul.fleurat-lessard/ReactionPath.html.

35. Jónsson, H.; Mills, G.; Jacobsen, K. W., Nudged elastic band method for finding minimum energy paths of transition. In *Classical and quantum dynamics in condensed phase simulations*, World Scientific: 1998; pp 385-404.

36. Mills, G.; Jónsson, H.; Schenter, G. K., Reversible work transition state theory: application to dissociative adsorption of hydrogen. *Surf Sci* **1995,** *324* (2–3), 305-337.

37. Ruban, A. V.; Skriver, H. L.; Nørskov, J. K., Surface segregation energies in transition-metal alloys. *Physical Review B* **1999,** *59* (24), 15990-16000.

38. Nilekar, A. U.; Ruban, A. V.; Mavrikakis, M., Surface segregation energies in low-index open surfaces of bimetallic transition metal alloys. *Surf Sci* **2009,** *603* (1), 91-96.

39. Han, J. W.; Kitchin, J. R.; Sholl, D. S., Step decoration of chiral metal surfaces. *J. Chem. Phys.* **2009,** *130* (12).

40. Nakamura, J.; Nakamura, I.; Uchijima, T.; Kanai, Y.; Watanabe, T.; Saito, M.; Fujitani, T., A Surface Science Investigation of Methanol Synthesis over a Zn-Deposited Polycrystalline Cu Surface. *Journal of Catalysis* **1996,** *160* (1), 65-75.

41. Liu, Z.-P.; Hu, P.; Alavi, A., Catalytic Role of Gold in Gold-Based Catalysts: A Density Functional Theory Study on the CO Oxidation on Gold. *Journal of the American Chemical Society* **2002,** *124* (49), 14770-14779.

42. Zhu, Z.; Barroo, C.; Lichtenstein, L.; Eren, B.; Wu, C. H.; Mao, B.; Visart de Bocarmé, T.; Liu, Z.; Kruse, N.; Salmeron, M.; Somorjai, G. A., Influence of Step Geometry on the Reconstruction of Stepped Platinum Surfaces under Coadsorption of Ethylene and CO. *The Journal of Physical Chemistry Letters* **2014,** *5* (15), 2626-2631.

43. Bronsted, J. N.; Pedersen, K., The catalytic disintegration of nitramide and its physical-chemical relevance. *Zeitschrift Fur Physikalische Chemie--Stochiometrie Und Verwandtschaftslehre* **1924,** *108* (3/4), 185-235.

44. Bligaard, T.; Nørskov, J. K.; Dahl, S.; Matthiesen, J.; Christensen, C. H.; Sehested, J., The Brønsted–Evans–Polanyi relation and the volcano curve in heterogeneous catalysis. *Journal of Catalysis* **2004,** *224* (1), 206-217.

45. Munter, T. R.; Bligaard, T.; Christensen, C. H.; Norskov, J. K., BEP relations for N_2 dissociation over stepped transition metal and alloy surfaces. *Physical Chemistry Chemical Physics* **2008,** *10* (34), 5202-5206.

46. Vojvodic, A.; Calle-Vallejo, F.; Guo, W.; Wang, S.; Toftelund, A.; Studt, F.; Martinez, J. I.; Shen, J.; Man, I. C.; Rossmeisl, J.; Bligaard, T.; Norskov, J. K.; Abild-Pedersen, F., On the behavior of Bronsted-Evans-Polanyi relations for transition metal oxides. *J. Chem. Phys.* **2011,** *134* (24).

CHAPTER 6

CONCLUSION

The biochemical and pharmaceutical communities has pushed for development in enantioselective chemical processes. Chiral surfaces have been shown to possess enantioselective properties. An improved understanding on how adsorbates interact on and with these chiral surfaces will provide valuable information towards the rational design of better heterogeneous catalyst. This thesis presents theoretical calculations for the adsorption of glycine, alanine, and R-3-methycyclohexanone on copper surfaces and the hydrogenation of formaldehyde and methoxide on heteroatom promoted copper surfaces. While many of these systems have been studied extensively experimentally, sheer system complexity and difficulty in directly observing adsorbate behavior limited our understanding of the system.. Using a theoretical approach, this thesis applied DFT calculations to model these surface-adsorbate interactions to examine these complex systems on an atomic scale. Our results provide useful insights into the behavior of chemisorbed and physisorbed species on copper surfaces. Additionally, we have shown that the application of dispersion corrected methods which were made possible by recent advancement in computational power were instrumental in the modeling of surface adsorption of both chemisorbed and physisorbed molecules. Notably, although van der Waals forces do not dominate the chemisorption of glycine or alanine on copper surfaces, the inclusion and consideration of van der Waals is necessary to address the discrepancy between the coexistence of homochiral and heterochiral glycine domains observed in experimental studies.

In Chapter 3, we re-examined the chemisorption of glycine and alanine on Cu(110) and Cu(3,1,17) using dispersion corrected methods. Our calculation predicts that the racemate alanine domain on Cu(110) does not thermodynamically preferred to segregate into enantiopure D- and L-alanine domains. For glycine on Cu(110), there was an apparent experimental discrepancy between LEED, STM, and XPS in the earlier works[1-3] where LEED and STM indicated the coexistence of two glycine domains while XPS indicated the existence of only one domains. Our calculations show that heterochiral and homochiral glycine domains coexist on Cu(110). Finally, the lack of agreement between experimental results and DFT calculated adsorption energies of D- and L-alanine adlayers on Cu(3,1,17) indicates that accurate predictions of minute enantiospecificity using computational simulations remain a challenge. The desires and the benefits that come with the capability to accurately model these systems have pushed for the continuous development of better functionals which seeks to address these challenges.

In Chapter 4, we investigated the physisorption of R-3-methycyclohexanone (R-3MCHO) on copper surfaces using dispersion corrected DFT and temperature programmed desorption (TPD). Compared to TPD, our study indicates a strong overbinding of R-3MCHO to the studied copper surfaces. These overbindings are systematic and correlated to the density of surface copper atoms. While these overbindings also mean DFT calculation do not achieve a quantitative agreement with the experimental TPD results, the DFT data using dispersion corrected methods show significantly better quantitative agreement with the experimental TPD data. Among the three dispersion corrected methods we implement in this work, PBE-B88 performs better than PBE-D2 and PBE-B86, but the differences in performance is relatively small. A qualitative agreement between PBE-D2 and TPD results is observed for adsorption energy differences between R-3MCHO adsorption on Cu(111), Cu(221), and Cu(643)^{R}. Finally, our DFT calculations predict a potential adsorbate-induced surface reconstruction on Cu(110). This finding is particularly interesting. While TPD results indicated a similarity between R-3MCHO adsorption on Cu(110) and on stepped Cu surfaces, no one suspected an adsorbate-induced surface reconstruction on Cu(110). It points to a clear value in computational study of surface-adsorbate interaction.

In Chapter 5, we utilized DFT to determine the impact of Zn and Zr heteroatoms on Cu surfaces and to investigate the impact of these heteroatoms on the adsorption energies of MeOH synthesis intermediates and the reaction barriers for key reaction steps. Our study finds that the presence of these heteroatoms greatly increases the binding energies of the studied reaction intermediates, the primary contributor to the increased reaction rates. While these heteroatoms are unlikely to cluster on the Cu surfaces, the rate of formaldehyde and methoxide hydrogenation of these cluster were orders of magnitude higher than the rate of hydrogenation of isolated heteroatom. Since thermal fluctuation under the typical experimental condition of 500 K resulted in 5-20% of the heteroatoms forming cluster on these stepped edges, a significant portion of the hydrogenation reaction takes places around these clusters. Furthermore, our calculations predict that the different orientations of Cu stepped edges produce noticeable differences in the adsorption of reaction intermediates and, consequently, reaction rates. Finally, we show that BEP serves as a reasonable approximation for the hydrogenation of formaldehyde and methoxide on Cu stepped edges. Finding the activation energies using NEB were computationally expensive and required significant amount of human input. Using the

BEP as an approximation, the models would only need to identify the surface geometries and adsorption energies of the reactant and the product. This allows for faster screening of reaction on heteroatom promoted Cu stepped edges.

In terms of future opportunities around the modeling of methanol synthesis, a more expansive study into the methanol synthesis on heteroatom promoted Cu surfaces is needed in order to fully understand the impact of heteroatom on other surface species and their impact on key reaction intermediates. The present model assumes the overall reaction takes place with all intermediates adsorbed in the most stable sites and geometries. In reality, however, the presence of other intermediates or surface species can significantly alter adsorption geometries or sites. A more detailed model that accounts for the presence of other major surface species or that shows the presence of currently ignored surface species may be valuable in understanding the overall reaction mechanism. Second, the present model assumes that the hydrogenations of formaldehyde and methoxide are the primary rate-limiting steps. While this has been shown to be true for this particular pathway,[4-5] several other potential pathways have been identified.[2-4, 10] A rigorous study of the impact of heteroatoms along all potential pathways would provide immense insight into the rational design of future catalysts for MeOH synthesis on Cu surfaces. Finally, the hydrogenation of formaldehyde was found to possess a negative activation energy on the heteroatom promoted Cu kinked edge, which points to either the formation of formaldehye or the hydrogenation of methoxide as the rate limiting step. Since this negative activation energy was based upon BEP estimation, a closer examination of the hydrogenation reaction at these sites should provide valuable information towards understanding the overall impact of heteroatom on Cu catalyst.

References

1. Toomes, R. L.; Kang, J. H.; Woodruff, D.; Polcik, M.; Kittel, M.; Hoeft, J. T., Can glycine form homochiral structural domains on low-index copper surfaces. *Surface Science Letters* **2003,** *522*, L9-L14.

2. Chen, Q.; Frankel, D. J.; Richardson, N. V., Chemisorption induced chirality: glycine on Cu{110}. *Surf Sci* **2002,** *497* (1-3), 37-46.

3. Rankin, R.; Sholl, D., Assessment of heterochiral and homochiral glycine adlayers on Cu(110) using density functional theory. *Surf Sci* **2004,** *548* (1-3), 301-308.

4. Edwards, J. F.; Schrader, G. L., Insitu fourer-transform infared study of methanol synthesis on mixed metal-oxide catalysts. *Journal of Catalysis* **1985,** *94* (1), 175-186.

5. Grabow, L. C.; Mavrikakis, M., Mechanism of Methanol Synthesis on Cu through CO_2 and CO Hydrogenation. *ACS Catalysis* **2011,** *1* (4), 365-384.

APPENDIX A

PBE-D2 CONVERGED STRUCTURES FOR DENSE ALANINE ON CU(3,1,17)^{S}

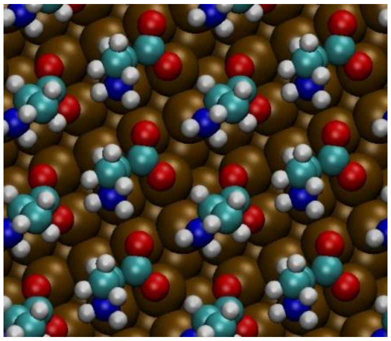
L_1_0_a

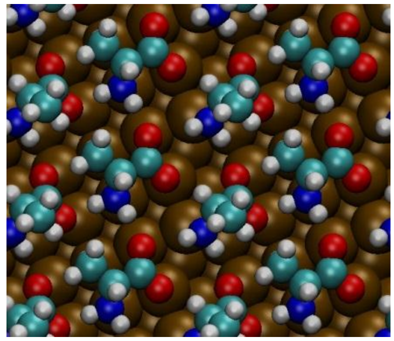
DL_1_0_a

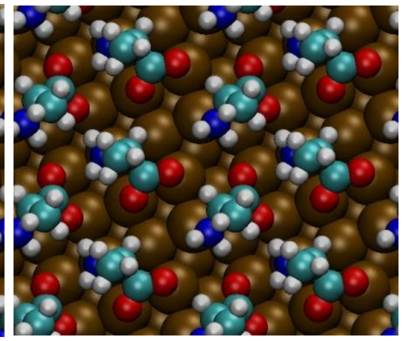
L_1_90_a

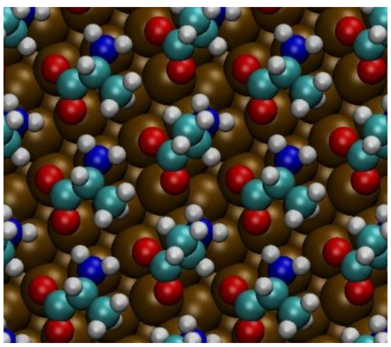
DL_2_180_a

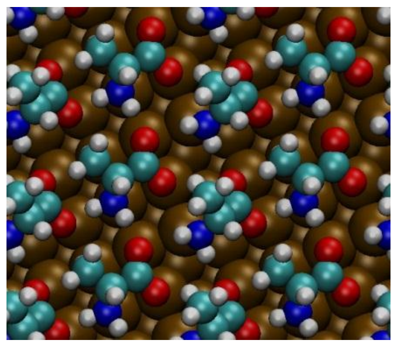
D_1_0_a

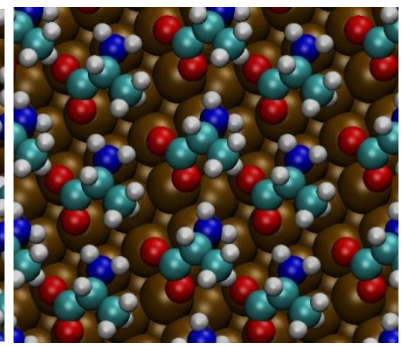
D_2_180_a

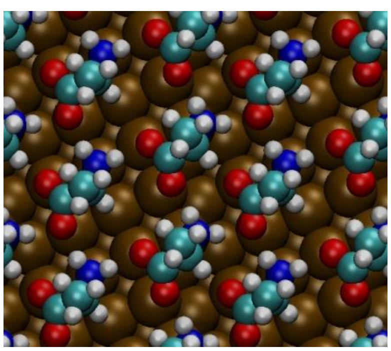
L_2_180_a

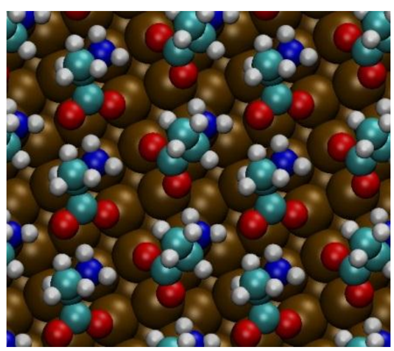
DL_2_90_b

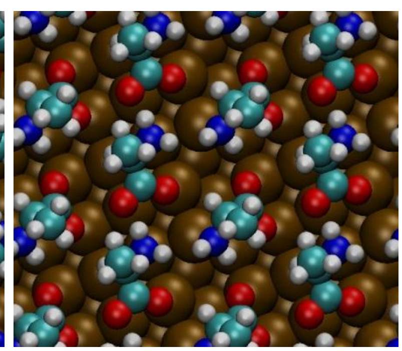
DL_1_90_b

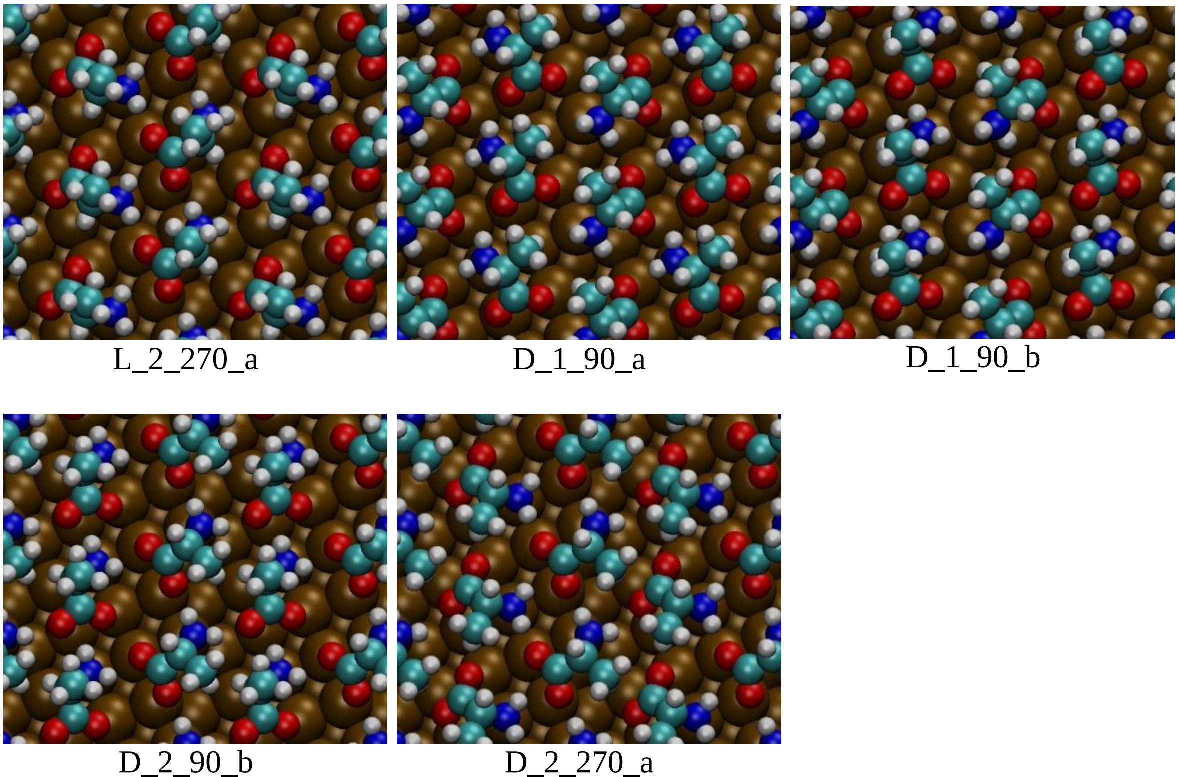

Figure A: Optimized dense adlayer of alanine on Cu(3,1,17)^S. Converged using PBE functional with DFT-D2 dispersion corrected method.

APPENDIX B

STRUCTURAL INFORMATION FOR THE OPTIMIZED ADSORPTION GEOMETRY OF DENSE GLYCINE AND ALANINE ADLAYER ON CU(110)

Table B.1: Unit cell vectors and fractional coordinates for the optimized adsorption geometry of homochiral domain dense glycine adlayer on Cu(110) as calculated by PBE. The unit cell vectors are given in Angstrom. Atomic positions are given in fraction of the unit cell vectors.

	Vector	x	y	z	No	Atom	a	b	c
	a	7.26	0.00	0.00	23	Cu	0.00	0.01	0.26
	b	0.00	7.70	0.00	24	Cu	0.00	0.33	0.00
	c	0.00	0.00	20.00	25	Cu	0.25	0.50	0.06
No	Atom	a	b	c	26	Cu	0.00	0.33	0.13
1	C	0.14	0.11	0.41	27	Cu	0.25	0.50	0.19
2	C	0.32	0.14	0.37	28	Cu	0.00	0.34	0.26
3	C	0.66	0.59	0.41	29	Cu	0.00	0.67	0.00
4	C	0.83	0.55	0.37	30	Cu	0.25	0.83	0.06
5	H	0.10	0.24	0.43	31	Cu	0.00	0.67	0.13
6	H	0.17	0.02	0.45	32	Cu	0.25	0.84	0.19
7	H	0.44	0.75	0.37	33	Cu	0.01	0.68	0.25
8	H	0.40	0.54	0.37	34	Cu	0.50	0.00	0.00
9	H	0.62	0.48	0.44	35	Cu	0.75	0.17	0.06
10	H	0.69	0.71	0.44	36	Cu	0.50	0.00	0.13
11	H	0.88	0.11	0.37	37	Cu	0.75	0.17	0.19
12	H	0.97	0.91	0.37	38	Cu	0.51	0.00	0.25
13	N	1.00	0.04	0.36	39	Cu	0.50	0.33	0.00
14	N	0.50	0.63	0.36	40	Cu	0.75	0.50	0.06
15	O	0.36	0.29	0.35	41	Cu	0.50	0.33	0.13
16	O	0.41	1.00	0.35	42	Cu	0.75	0.50	0.19
17	O	0.85	0.39	0.35	43	Cu	0.50	0.33	0.26
18	O	0.93	0.67	0.35	44	Cu	0.50	0.67	0.00
19	Cu	0.00	0.00	0.00	45	Cu	0.75	0.83	0.06
20	Cu	0.25	0.17	0.06	46	Cu	0.50	0.67	0.13
21	Cu	0.00	0.00	0.13	47	Cu	0.75	0.84	0.19
22	Cu	0.25	0.17	0.19	48	Cu	0.51	0.66	0.26

Table B.2: Unit cell vectors and fractional coordinates for the optimized adsorption geometry of homochiral domain dense glycine adlayer on Cu(110) as calculated by PBE-D2. The unit cell vectors are given in Angstrom. Atomic positions are given in fraction of the unit cell vectors.

	Vector	x	y	z	No	Atom	a	b	c
	a	7.13	0.00	0.00	23	Cu	0.00	0.01	0.25
	b	0.00	7.56	0.00	24	Cu	0.00	0.33	0.00
	c	0.00	0.00	20.00	25	Cu	0.25	0.50	0.06
No	Atom	a	b	c	26	Cu	0.00	0.33	0.13
1	C	0.12	0.11	0.40	27	Cu	0.25	0.50	0.19
2	C	0.30	0.14	0.36	28	Cu	-0.01	0.34	0.26
3	C	0.63	0.59	0.40	29	Cu	0.00	0.67	0.00
4	C	0.81	0.54	0.36	30	Cu	0.25	0.83	0.06
5	H	0.07	0.24	0.42	31	Cu	0.00	0.67	0.13
6	H	0.15	0.03	0.44	32	Cu	0.25	0.84	0.19
7	H	0.42	0.76	0.37	33	Cu	0.01	0.68	0.25
8	H	0.37	0.55	0.36	34	Cu	0.50	0.00	0.00
9	H	0.59	0.48	0.43	35	Cu	0.75	0.17	0.06
10	H	0.67	0.71	0.44	36	Cu	0.50	0.00	0.13
11	H	0.85	0.11	0.36	37	Cu	0.75	0.17	0.19
12	H	0.94	0.91	0.37	38	Cu	0.51	0.00	0.25
13	N	-0.03	0.04	0.36	39	Cu	0.50	0.33	0.00
14	N	0.48	0.64	0.36	40	Cu	0.75	0.50	0.06
15	O	0.34	0.30	0.34	41	Cu	0.50	0.33	0.13
16	O	0.40	0.00	0.35	42	Cu	0.75	0.50	0.19
17	O	0.83	0.39	0.34	43	Cu	0.50	0.33	0.26
18	O	0.92	0.67	0.35	44	Cu	0.50	0.67	0.00
19	Cu	0.00	0.00	0.00	45	Cu	0.75	0.83	0.06
20	Cu	0.25	0.17	0.06	46	Cu	0.50	0.67	0.13
21	Cu	0.00	0.00	0.13	47	Cu	0.75	0.83	0.19
22	Cu	0.25	0.17	0.19	48	Cu	0.50	0.66	0.25

Table B.3: Unit cell vectors and fractional coordinates for the optimized adsorption geometry of heterochiral domain dense glycine adlayer on Cu(110) as calculated by PBE. The unit cell vectors are given in Angstrom. Atomic positions are given in fraction of the unit cell vectors.

	Vector	x	y	z	No	Atom	a	b	c
	a	7.26	0.00	0.00	23	Cu	0.00	0.01	0.26
	b	0.00	7.70	0.00	24	Cu	0.00	0.33	0.00
	c	0.00	0.00	20.00	25	Cu	0.25	0.50	0.06
No	Atom	a	b	c	26	Cu	0.00	0.33	0.13
1	C	0.14	0.11	0.41	27	Cu	0.25	0.50	0.19
2	C	0.32	0.14	0.37	28	Cu	0.99	0.34	0.26
3	C	0.65	0.59	0.41	29	Cu	0.00	0.67	0.00
4	C	0.82	0.55	0.37	30	Cu	0.25	0.83	0.06
5	H	0.09	0.24	0.42	31	Cu	0.00	0.67	0.13
6	H	0.16	0.03	0.45	32	Cu	0.25	0.84	0.19
7	H	0.39	0.54	0.37	33	Cu	0.01	0.68	0.25
8	H	0.44	0.76	0.37	34	Cu	0.50	0.00	0.00
9	H	0.61	0.48	0.44	35	Cu	0.75	0.17	0.06
10	H	0.68	0.70	0.44	36	Cu	0.50	0.00	0.13
11	H	0.88	0.11	0.37	37	Cu	0.75	0.17	0.19
12	H	0.97	0.91	0.37	38	Cu	0.50	1.00	0.25
13	N	0.99	0.04	0.36	39	Cu	0.50	0.33	0.00
14	N	0.49	0.64	0.36	40	Cu	0.75	0.50	0.06
15	O	0.36	0.29	0.35	41	Cu	0.50	0.33	0.13
16	O	0.41	1.00	0.35	42	Cu	0.75	0.50	0.19
17	O	0.85	0.39	0.35	43	Cu	0.50	0.33	0.26
18	O	0.93	0.67	0.35	44	Cu	0.50	0.67	0.00
19	Cu	0.00	0.00	0.00	45	Cu	0.75	0.83	0.06
20	Cu	0.25	0.17	0.06	46	Cu	0.50	0.67	0.13
21	Cu	0.00	0.00	0.13	47	Cu	0.75	0.84	0.19
22	Cu	0.25	0.17	0.19	48	Cu	0.50	0.66	0.26

Table B.4: Unit cell vectors and fractional coordinates for the optimized adsorption geometry of heterochiral domain dense glycine adlayer on Cu(110) as calculated by PBE-D2. The unit cell vectors are given in Angstrom. Atomic positions are given in fraction of the unit cell vectors.

	Vector	x	y	z	No	Atom	a	b	c
	a	7.13	0.00	0.00	23	Cu	0.00	0.01	0.26
	b	0.00	7.56	0.00	24	Cu	0.00	0.33	0.00
	c	0.00	0.00	20.00	25	Cu	0.25	0.50	0.06
No	Atom	a	b	c	26	Cu	0.00	0.33	0.13
1	C	0.12	0.11	0.40	27	Cu	0.25	0.50	0.19
2	C	0.31	0.14	0.36	28	Cu	-0.01	0.34	0.26
3	C	0.64	0.59	0.40	29	Cu	0.00	0.67	0.00
4	C	0.81	0.54	0.36	30	Cu	0.25	0.83	0.06
5	H	0.07	0.24	0.42	31	Cu	0.00	0.67	0.13
6	H	0.15	0.03	0.44	32	Cu	0.25	0.84	0.19
7	H	0.37	0.55	0.36	33	Cu	0.01	0.68	0.25
8	H	0.43	0.77	0.37	34	Cu	0.50	0.00	0.00
9	H	0.59	0.48	0.43	35	Cu	0.75	0.17	0.06
10	H	0.67	0.70	0.44	36	Cu	0.50	0.00	0.13
11	H	0.86	0.11	0.36	37	Cu	0.75	0.17	0.19
12	H	0.95	0.91	0.37	38	Cu	0.51	0.00	0.25
13	N	-0.02	0.04	0.36	39	Cu	0.50	0.33	0.00
14	N	0.48	0.64	0.36	40	Cu	0.75	0.50	0.06
15	O	0.34	0.30	0.34	41	Cu	0.50	0.33	0.13
16	O	0.40	0.00	0.35	42	Cu	0.75	0.50	0.19
17	O	0.83	0.38	0.34	43	Cu	0.50	0.33	0.26
18	O	0.92	0.67	0.35	44	Cu	0.50	0.67	0.00
19	Cu	0.00	0.00	0.00	45	Cu	0.75	0.83	0.06
20	Cu	0.25	0.17	0.06	46	Cu	0.50	0.67	0.13
21	Cu	0.00	0.00	0.13	47	Cu	0.75	0.83	0.19
22	Cu	0.25	0.17	0.19	48	Cu	0.50	0.66	0.25

Table B.5: Unit cell vectors and fractional coordinates for the optimized adsorption geometry of enantiopure dense alanine adlayer on Cu(110) as calculated by PBE-D2. The unit cell vectors are given in Angstrom. Atomic positions are given in fraction of the unit cell vectors.

	Vector	x	y	z	No	Atom	a	b	c
	a	7.13	0.00	0.00	26	Cu	0.25	0.17	0.06
	b	0.00	7.56	0.00	27	Cu	1.00	0.00	0.13
	c	0.00	0.00	20.00	28	Cu	0.25	0.17	0.19
No	Atom	a	b	c	29	Cu	1.00	0.01	0.26
1	C	0.12	0.12	0.40	30	Cu	0.00	0.33	0.00
2	C	0.15	0.01	0.47	31	Cu	0.25	0.50	0.06
3	C	0.30	0.14	0.36	32	Cu	1.00	0.33	0.13
4	C	0.60	0.50	0.46	33	Cu	0.25	0.50	0.19
5	C	0.64	0.62	0.40	34	Cu	0.99	0.34	0.26
6	C	0.82	0.55	0.36	35	Cu	0.00	0.67	0.00
7	H	0.01	0.00	0.49	36	Cu	0.25	0.83	0.06
8	H	0.07	0.25	0.41	37	Cu	0.00	0.67	0.13
9	H	0.20	0.88	0.46	38	Cu	0.25	0.84	0.19
10	H	0.25	0.08	0.50	39	Cu	0.01	0.67	0.25
11	H	0.39	0.53	0.36	40	Cu	0.50	0.00	0.00
12	H	0.41	0.76	0.37	41	Cu	0.75	0.17	0.06
13	H	0.48	0.55	0.49	42	Cu	0.50	0.00	0.13
14	H	0.56	0.36	0.44	43	Cu	0.75	0.17	0.19
15	H	0.68	0.75	0.42	44	Cu	0.51	0.99	0.25
16	H	0.72	0.48	0.50	45	Cu	0.50	0.33	0.00
17	H	0.85	0.10	0.36	46	Cu	0.75	0.50	0.06
18	H	0.96	0.90	0.37	47	Cu	0.50	0.33	0.13
19	N	0.98	0.03	0.36	48	Cu	0.75	0.50	0.19
20	N	0.48	0.64	0.36	49	Cu	0.50	0.33	0.26
21	O	0.34	0.29	0.34	50	Cu	0.50	0.67	0.00
22	O	0.39	0.00	0.35	51	Cu	0.75	0.83	0.06
23	O	0.82	0.39	0.34	52	Cu	0.50	0.67	0.13
24	O	0.94	0.66	0.35	53	Cu	0.75	0.83	0.19
25	Cu	0.00	0.00	0.00	54	Cu	0.50	0.66	0.26

Table B.6: Unit cell vectors and fractional coordinates for the optimized adsorption geometry of enantiopure dense alanine adlayer on Cu(110) as calculated by PBE-D2. The unit cell vectors are given in Angstrom. Atomic positions are given in fraction of the unit cell vectors.

	Vector	x	y	z	No	Atom	a	b	c
	a	7.13	0.00	0.00	26	Cu	0.25	0.17	0.06
	b	0.00	7.56	0.00	27	Cu	1.00	1.00	0.13
	c	0.00	0.00	20.00	28	Cu	0.25	0.17	0.19
No	Atom	a	b	c	29	Cu	0.00	0.01	0.26
1	C	0.12	0.11	0.40	30	Cu	0.00	0.33	0.00
2	C	0.16	0.99	0.46	31	Cu	0.25	0.50	0.06
3	C	0.30	0.14	0.36	32	Cu	1.00	0.33	0.13
4	C	0.62	0.56	0.40	33	Cu	0.25	0.50	0.19
5	C	0.66	0.69	0.46	34	Cu	0.99	0.34	0.26
6	C	0.80	0.53	0.36	35	Cu	0.00	0.67	0.00
7	H	0.95	0.90	0.37	36	Cu	0.25	0.83	0.06
8	H	0.03	0.97	0.49	37	Cu	1.00	0.67	0.13
9	H	0.07	0.24	0.42	38	Cu	0.25	0.83	0.19
10	H	0.21	0.86	0.45	39	Cu	0.01	0.67	0.25
11	H	0.26	0.05	0.50	40	Cu	0.50	0.00	0.00
12	H	0.36	0.56	0.36	41	Cu	0.75	0.17	0.06
13	H	0.44	0.77	0.37	42	Cu	0.50	0.00	0.13
14	H	0.53	0.71	0.49	43	Cu	0.75	0.17	0.19
15	H	0.57	0.44	0.42	44	Cu	0.51	0.99	0.25
16	H	0.70	0.82	0.45	45	Cu	0.50	0.33	0.00
17	H	0.76	0.63	0.50	46	Cu	0.75	0.50	0.06
18	H	0.86	0.11	0.36	47	Cu	0.50	0.33	0.13
19	N	0.98	0.03	0.36	48	Cu	0.75	0.50	0.19
20	N	0.48	0.64	0.36	49	Cu	0.50	0.33	0.26
21	O	0.33	0.29	0.34	50	Cu	0.50	0.67	0.00
22	O	0.40	0.00	0.35	51	Cu	0.75	0.83	0.06
23	O	0.83	0.38	0.34	52	Cu	0.50	0.67	0.13
24	O	0.91	0.66	0.35	53	Cu	0.75	0.83	0.19
25	Cu	0.00	0.00	0.00	54	Cu	0.50	0.66	0.26

APPENDIX C

STRUCTURAL INFORMATION FOR THE OPTIMIZED ADSORPTION GEOMETRY OF DENSE ALANINE ADLAYER ON CU(3,1,17)^S

Table C.1: Unit cell vectors and fractional coordinates for the optimized adsorption geometry of dense alanine adlayer L_1_0_a on Cu(3,1,17)^S as calculated by PBE-D2. The unit cell vectors are given in Angstrom. Atomic positions are given in fraction of the unit cell vectors.

	Vector	x	y	z	No	Atom	a	b	c
	a	9.75	0.56	0.00	29	Cu	0.54	0.65	0.97
	b	0.00	5.63	0.00	30	Cu	0.43	0.05	0.96
	c	0.00	0.00	20.00	31	Cu	0.31	0.48	0.96
No	Atom	a	b	c	32	Cu	0.20	0.88	0.94
1	C	0.16	0.14	0.13	33	Cu	0.09	0.29	0.93
2	C	0.23	0.07	0.20	34	Cu	0.97	0.70	0.92
3	C	0.26	0.22	0.08	35	Cu	0.86	0.12	0.91
4	C	0.60	0.48	0.20	36	Cu	0.75	0.53	0.90
5	C	0.63	0.50	0.12	37	Cu	0.63	0.95	0.89
6	C	0.77	0.60	0.11	38	Cu	0.52	0.35	0.88
7	H	0.01	0.88	0.13	39	Cu	0.41	0.76	0.87
8	H	0.08	0.28	0.13	40	Cu	0.29	0.17	0.86
9	H	0.15	0.01	0.23	41	Cu	0.18	0.58	0.85
10	H	0.16	0.79	0.09	42	Cu	0.07	0.99	0.84
11	H	0.27	0.23	0.22	43	Cu	0.95	0.41	0.82
12	H	0.31	0.93	0.19	44	Cu	0.84	0.82	0.81
13	H	0.50	0.41	0.21	45	Cu	0.73	0.23	0.80
14	H	0.52	0.20	0.09	46	Cu	0.61	0.64	0.79
15	H	0.55	0.62	0.10	47	Cu	0.50	0.05	0.78
16	H	0.61	0.65	0.22	48	Cu	0.38	0.46	0.77
17	H	0.69	0.14	0.11	49	Cu	0.27	0.87	0.76
18	H	0.68	0.36	0.22	50	Cu	0.16	0.28	0.75
19	N	0.09	0.93	0.10	51	Cu	0.04	0.70	0.74
20	N	0.62	0.27	0.09	52	Cu	0.93	0.11	0.73
21	O	0.25	0.43	0.05	53	Cu	0.82	0.52	0.72
22	O	0.35	0.05	0.06	54	Cu	0.70	0.93	0.71
23	O	0.78	0.82	0.10	55	Cu	0.59	0.34	0.70
24	O	0.87	0.44	0.10	56	Cu	0.47	0.75	0.69
25	Cu	1.00	0.99	0.01	57	Cu	0.36	0.16	0.68
26	Cu	0.90	0.41	0.00	58	Cu	0.25	0.58	0.67
27	Cu	0.76	0.83	0.99	59	Cu	0.13	0.99	0.66
28	Cu	0.66	0.25	0.99	60	Cu	0.02	0.40	0.65

Table C.2: Unit cell vectors and fractional coordinates for the optimized adsorption geometry of dense alanine adlayer DL_1_0_a on Cu(3,1,17)^S as calculated by PBE-D2. The unit cell vectors are given in Angstrom. Atomic positions are given in fraction of the unit cell vectors.

	Vector	x	y	z	No	Atom	a	b	c
	a	9.75	0.56	0.00	29	Cu	0.54	0.65	0.97
	b	0.00	5.63	0.00	30	Cu	0.43	0.06	0.96
	c	0.00	0.00	20.00	31	Cu	0.31	0.48	0.96
No	Atom	a	b	c	32	Cu	0.20	0.88	0.94
1	C	0.15	0.14	0.13	33	Cu	0.09	0.29	0.93
2	C	0.23	0.08	0.19	34	Cu	0.98	0.70	0.92
3	C	0.25	0.22	0.08	35	Cu	0.86	0.12	0.91
4	C	0.51	0.63	0.13	36	Cu	0.75	0.53	0.90
5	C	0.64	0.46	0.13	37	Cu	0.63	0.95	0.89
6	C	0.77	0.57	0.11	38	Cu	0.52	0.35	0.88
7	H	0.01	0.88	0.13	39	Cu	0.41	0.76	0.87
8	H	0.07	0.28	0.14	40	Cu	0.30	0.17	0.86
9	H	0.15	0.02	0.23	41	Cu	0.18	0.58	0.85
10	H	0.15	0.79	0.09	42	Cu	0.07	0.99	0.84
11	H	0.27	0.23	0.22	43	Cu	0.95	0.41	0.82
12	H	0.31	0.93	0.19	44	Cu	0.84	0.82	0.81
13	H	0.42	0.54	0.15	45	Cu	0.73	0.23	0.80
14	H	0.49	0.69	0.08	46	Cu	0.61	0.64	0.79
15	H	0.52	0.19	0.09	47	Cu	0.50	0.05	0.78
16	H	0.53	0.78	0.16	48	Cu	0.38	0.46	0.77
17	H	0.65	0.40	0.19	49	Cu	0.27	0.87	0.76
18	H	0.68	0.10	0.11	50	Cu	0.16	0.28	0.75
19	N	0.09	0.93	0.10	51	Cu	0.04	0.70	0.74
20	N	0.62	0.24	0.09	52	Cu	0.93	0.11	0.73
21	O	0.24	0.43	0.05	53	Cu	0.82	0.52	0.72
22	O	0.35	0.06	0.06	54	Cu	0.70	0.93	0.71
23	O	0.77	0.79	0.10	55	Cu	0.59	0.34	0.70
24	O	0.87	0.43	0.10	56	Cu	0.47	0.75	0.69
25	Cu	1.00	0.99	0.01	57	Cu	0.36	0.16	0.68
26	Cu	0.90	0.41	0.00	58	Cu	0.25	0.58	0.67
27	Cu	0.76	0.83	0.99	59	Cu	0.13	0.99	0.66
28	Cu	0.65	0.25	0.99	60	Cu	0.02	0.40	0.65

Table C.3: Unit cell vectors and fractional coordinates for the optimized adsorption geometry of dense alanine adlayer L_1_90_a on Cu(3,1,17)^S as calculated by PBE-D2. The unit cell vectors are given in Angstrom. Atomic positions are given in fraction of the unit cell vectors.

	Vector	x	y	z	No	Atom	a	b	c
	a	9.75	0.56	0.00	29	Cu	0.54	0.65	0.98
	b	0.00	5.63	0.00	30	Cu	0.43	0.06	0.96
	c	0.00	0.00	20.00	31	Cu	0.31	0.48	0.96
No	Atom	a	b	c	32	Cu	0.20	0.88	0.94
1	C	0.14	0.14	0.13	33	Cu	0.09	0.29	0.93
2	C	0.21	0.08	0.20	34	Cu	0.98	0.70	0.92
3	C	0.25	0.22	0.08	35	Cu	0.86	0.12	0.91
4	C	0.58	0.62	0.20	36	Cu	0.75	0.52	0.90
5	C	0.62	0.65	0.12	37	Cu	0.63	0.94	0.89
6	C	0.73	0.44	0.10	38	Cu	0.52	0.35	0.88
7	H	0.00	0.87	0.13	39	Cu	0.41	0.76	0.87
8	H	0.06	0.28	0.13	40	Cu	0.30	0.17	0.86
9	H	0.14	0.02	0.23	41	Cu	0.18	0.58	0.85
10	H	0.15	0.79	0.09	42	Cu	0.07	0.99	0.83
11	H	0.26	0.24	0.22	43	Cu	0.95	0.41	0.82
12	H	0.29	0.94	0.19	44	Cu	0.84	0.82	0.81
13	H	0.46	0.49	0.08	45	Cu	0.73	0.23	0.80
14	H	0.44	0.79	0.09	46	Cu	0.61	0.64	0.79
15	H	0.51	0.77	0.21	47	Cu	0.50	0.05	0.78
16	H	0.53	0.45	0.20	48	Cu	0.38	0.46	0.77
17	H	0.67	0.62	0.23	49	Cu	0.27	0.87	0.76
18	H	0.67	0.82	0.12	50	Cu	0.16	0.28	0.75
19	N	0.08	0.93	0.10	51	Cu	0.04	0.70	0.74
20	N	0.51	0.65	0.08	52	Cu	0.93	0.11	0.73
21	O	0.24	0.43	0.05	53	Cu	0.82	0.52	0.72
22	O	0.34	0.06	0.06	54	Cu	0.70	0.93	0.71
23	O	0.67	0.24	0.09	55	Cu	0.59	0.34	0.70
24	O	0.85	0.48	0.10	56	Cu	0.47	0.75	0.69
25	Cu	0.99	0.99	0.01	57	Cu	0.36	0.16	0.68
26	Cu	0.90	0.43	0.00	58	Cu	0.25	0.58	0.67
27	Cu	0.77	0.82	0.99	59	Cu	0.13	0.99	0.66
28	Cu	0.66	0.22	0.98	60	Cu	0.02	0.40	0.65

Table C.4: Unit cell vectors and fractional coordinates for the optimized adsorption geometry of dense alanine adlayer DL_2_180_a on Cu(3,1,17)^{S} as calculated by PBE-D2. The unit cell vectors are given in Angstrom. Atomic positions are given in fraction of the unit cell vectors.

	Vector	x	y	z	No	Atom	a	b	c
	a	9.75	0.56	0.00	29	Cu	0.55	0.64	0.98
	b	0.00	5.63	0.00	30	Cu	0.43	0.05	0.96
	c	0.00	0.00	20.00	31	Cu	0.30	0.48	0.95
No	Atom	a	b	c	32	Cu	0.20	0.89	0.94
1	C	0.92	0.70	0.11	33	Cu	0.09	0.30	0.93
2	C	0.99	0.93	0.21	34	Cu	0.98	0.70	0.92
3	C	0.04	0.82	0.15	35	Cu	0.86	0.11	0.91
4	C	0.37	0.34	0.08	36	Cu	0.75	0.53	0.90
5	C	0.49	0.45	0.12	37	Cu	0.63	0.93	0.89
6	C	0.61	0.28	0.14	38	Cu	0.52	0.35	0.88
7	H	0.91	0.06	0.21	39	Cu	0.41	0.76	0.87
8	H	0.96	0.80	0.25	40	Cu	0.30	0.17	0.86
9	H	0.05	0.18	0.11	41	Cu	0.18	0.58	0.85
10	H	0.08	0.02	0.24	42	Cu	0.07	0.99	0.84
11	H	0.12	0.69	0.15	43	Cu	0.95	0.41	0.82
12	H	0.19	0.00	0.10	44	Cu	0.84	0.82	0.81
13	H	0.44	0.52	0.17	45	Cu	0.73	0.23	0.80
14	H	0.47	0.81	0.09	46	Cu	0.61	0.64	0.79
15	H	0.58	0.13	0.17	47	Cu	0.50	0.05	0.78
16	H	0.63	0.70	0.10	48	Cu	0.38	0.46	0.77
17	H	0.66	0.21	0.09	49	Cu	0.27	0.87	0.76
18	H	0.69	0.37	0.17	50	Cu	0.16	0.28	0.75
19	N	0.08	0.01	0.10	51	Cu	0.04	0.70	0.74
20	N	0.53	0.66	0.08	52	Cu	0.93	0.11	0.73
21	O	0.81	0.83	0.10	53	Cu	0.82	0.52	0.72
22	O	0.94	0.48	0.10	54	Cu	0.70	0.93	0.71
23	O	0.28	0.48	0.06	55	Cu	0.59	0.34	0.70
24	O	0.38	0.11	0.07	56	Cu	0.47	0.75	0.69
25	Cu	0.01	1.00	0.01	57	Cu	0.36	0.16	0.68
26	Cu	0.88	0.41	0.00	58	Cu	0.25	0.58	0.67
27	Cu	0.77	0.83	0.99	59	Cu	0.13	0.99	0.66
28	Cu	0.66	0.23	0.98	60	Cu	0.02	0.40	0.65

Table C.5: Unit cell vectors and fractional coordinates for the optimized adsorption geometry of dense alanine adlayer D_1_0_a on Cu(3,1,17)^S as calculated by PBE-D2. The unit cell vectors are given in Angstrom. Atomic positions are given in fraction of the unit cell vectors.

	Vector	x	y	z	No	Atom	a	b	c
	a	9.75	0.56	0.00	29	Cu	0.54	0.65	0.97
	b	0.00	5.63	0.00	30	Cu	0.43	0.06	0.96
	c	0.00	0.00	20.00	31	Cu	0.31	0.48	0.96
No	Atom	a	b	c	32	Cu	0.20	0.88	0.94
1	C	0.18	0.10	0.14	33	Cu	0.09	0.29	0.93
2	C	0.11	0.29	0.18	34	Cu	0.98	0.70	0.92
3	C	0.26	0.20	0.08	35	Cu	0.86	0.12	0.91
4	C	0.50	0.62	0.13	36	Cu	0.75	0.53	0.90
5	C	0.63	0.45	0.13	37	Cu	0.63	0.95	0.89
6	C	0.76	0.57	0.11	38	Cu	0.52	0.35	0.88
7	H	-0.01	0.94	0.13	39	Cu	0.41	0.76	0.87
8	H	0.25	-0.02	0.16	40	Cu	0.29	0.17	0.86
9	H	0.06	0.20	0.22	41	Cu	0.18	0.58	0.85
10	H	0.12	0.77	0.10	42	Cu	0.07	0.99	0.84
11	H	0.19	0.38	0.20	43	Cu	0.95	0.41	0.82
12	H	0.04	0.41	0.15	44	Cu	0.84	0.82	0.81
13	H	0.41	0.53	0.15	45	Cu	0.73	0.23	0.80
14	H	0.48	0.67	0.08	46	Cu	0.61	0.64	0.79
15	H	0.52	0.19	0.09	47	Cu	0.50	0.05	0.78
16	H	0.52	0.78	0.16	48	Cu	0.38	0.46	0.77
17	H	0.65	0.39	0.19	49	Cu	0.27	0.87	0.76
18	H	0.68	0.10	0.10	50	Cu	0.16	0.28	0.75
19	N	0.07	0.94	0.10	51	Cu	0.04	0.70	0.74
20	N	0.61	0.24	0.09	52	Cu	0.93	0.11	0.73
21	O	0.23	0.41	0.06	53	Cu	0.82	0.52	0.72
22	O	0.35	0.05	0.05	54	Cu	0.70	0.93	0.71
23	O	0.76	0.79	0.10	55	Cu	0.59	0.34	0.70
24	O	0.86	0.42	0.10	56	Cu	0.47	0.75	0.69
25	Cu	0.00	-0.01	0.01	57	Cu	0.36	0.16	0.68
26	Cu	0.90	0.41	0.00	58	Cu	0.25	0.58	0.67
27	Cu	0.76	0.83	0.99	59	Cu	0.13	0.99	0.66
28	Cu	0.65	0.25	0.99	60	Cu	0.02	0.40	0.65

Table C.6: Unit cell vectors and fractional coordinates for the optimized adsorption geometry of dense alanine adlayer D_2_180_a on Cu(3,1,17)^S as calculated by PBE-D2. The unit cell vectors are given in Angstrom. Atomic positions are given in fraction of the unit cell vectors.

	Vector	x	y	z	No	Atom	a	b	c
	a	9.75	0.56	0.00	29	Cu	0.55	0.64	0.98
	b	0.00	5.63	0.00	30	Cu	0.43	0.05	0.96
	c	0.00	0.00	20.00	31	Cu	0.31	0.48	0.95
No	Atom	a	b	c	32	Cu	0.20	0.89	0.94
1	C	0.91	0.70	0.11	33	Cu	0.09	0.29	0.93
2	C	0.13	0.69	0.19	34	Cu	0.98	0.70	0.92
3	C	0.02	0.84	0.15	35	Cu	0.86	0.11	0.91
4	C	0.38	0.32	0.08	36	Cu	0.75	0.53	0.90
5	C	0.49	0.44	0.12	37	Cu	0.63	0.93	0.89
6	C	0.61	0.27	0.14	38	Cu	0.52	0.35	0.88
7	H	0.19	0.59	0.15	39	Cu	0.41	0.76	0.87
8	H	0.09	0.57	0.22	40	Cu	0.30	0.17	0.86
9	H	0.06	0.18	0.11	41	Cu	0.18	0.58	0.85
10	H	0.20	0.80	0.22	42	Cu	0.07	0.99	0.84
11	H	0.96	0.96	0.19	43	Cu	0.95	0.41	0.82
12	H	0.18	0.98	0.10	44	Cu	0.84	0.82	0.81
13	H	0.44	0.50	0.17	45	Cu	0.73	0.23	0.80
14	H	0.47	0.80	0.09	46	Cu	0.61	0.64	0.79
15	H	0.58	0.11	0.16	47	Cu	0.50	0.05	0.78
16	H	0.63	0.69	0.10	48	Cu	0.38	0.46	0.77
17	H	0.66	0.21	0.09	49	Cu	0.27	0.87	0.76
18	H	0.68	0.36	0.17	50	Cu	0.16	0.28	0.75
19	N	0.08	0.01	0.10	51	Cu	0.04	0.70	0.74
20	N	0.53	0.65	0.08	52	Cu	0.93	0.11	0.73
21	O	0.80	0.82	0.10	53	Cu	0.82	0.52	0.72
22	O	0.95	0.49	0.10	54	Cu	0.70	0.93	0.71
23	O	0.28	0.47	0.05	55	Cu	0.59	0.34	0.70
24	O	0.38	0.10	0.07	56	Cu	0.47	0.75	0.69
25	Cu	0.01	1.00	0.01	57	Cu	0.36	0.16	0.68
26	Cu	0.88	0.41	0.00	58	Cu	0.25	0.58	0.67
27	Cu	0.77	0.83	0.99	59	Cu	0.13	0.99	0.66
28	Cu	0.66	0.23	0.98	60	Cu	0.02	0.40	0.65

Table C.7: Unit cell vectors and fractional coordinates for the optimized adsorption geometry of dense alanine adlayer L_2_180_a on Cu(3,1,17)^S as calculated by PBE-D2. The unit cell vectors are given in Angstrom. Atomic positions are given in fraction of the unit cell vectors.

	Vector	x	y	z	No	Atom	a	b	c
	a	9.75	0.56	0.00	29	Cu	0.55	0.64	0.98
	b	0.00	5.63	0.00	30	Cu	0.43	0.05	0.96
	c	0.00	0.00	20.00	31	Cu	0.31	0.48	0.95
No	Atom	a	b	c	32	Cu	0.20	0.89	0.94
1	C	0.91	0.70	0.11	33	Cu	0.09	0.30	0.93
2	C	1.00	0.92	0.22	34	Cu	0.98	0.70	0.92
3	C	0.04	0.82	0.15	35	Cu	0.86	0.11	0.91
4	C	0.38	0.32	0.08	36	Cu	0.75	0.53	0.90
5	C	0.47	0.44	0.19	37	Cu	0.63	0.93	0.89
6	C	0.50	0.41	0.11	38	Cu	0.52	0.35	0.88
7	H	0.91	0.06	0.21	39	Cu	0.41	0.76	0.87
8	H	0.97	0.78	0.25	40	Cu	0.30	0.17	0.86
9	H	0.04	0.18	0.12	41	Cu	0.18	0.58	0.85
10	H	0.08	0.01	0.24	42	Cu	0.07	0.99	0.84
11	H	0.12	0.69	0.15	43	Cu	0.95	0.41	0.82
12	H	0.18	0.01	0.10	44	Cu	0.84	0.82	0.81
13	H	0.39	0.57	0.20	45	Cu	0.73	0.23	0.80
14	H	0.45	0.27	0.21	46	Cu	0.61	0.64	0.79
15	H	0.46	0.77	0.09	47	Cu	0.50	0.05	0.78
16	H	0.57	0.51	0.21	48	Cu	0.38	0.46	0.77
17	H	0.59	0.29	0.10	49	Cu	0.27	0.87	0.76
18	H	0.63	0.69	0.10	50	Cu	0.16	0.28	0.75
19	N	0.08	0.01	0.10	51	Cu	0.04	0.70	0.74
20	N	0.53	0.64	0.08	52	Cu	0.93	0.11	0.73
21	O	0.81	0.83	0.10	53	Cu	0.82	0.52	0.72
22	O	0.93	0.48	0.10	54	Cu	0.70	0.93	0.71
23	O	0.28	0.47	0.06	55	Cu	0.59	0.34	0.70
24	O	0.37	0.09	0.07	56	Cu	0.47	0.75	0.69
25	Cu	0.01	1.00	0.01	57	Cu	0.36	0.16	0.68
26	Cu	0.88	0.41	0.00	58	Cu	0.25	0.58	0.67
27	Cu	0.77	0.84	0.99	59	Cu	0.13	0.99	0.66
28	Cu	0.66	0.23	0.98	60	Cu	0.02	0.40	0.65

Table C.8: Unit cell vectors and fractional coordinates for the optimized adsorption geometry of dense alanine adlayer DL_2_90_b on Cu(3,1,17)^{S} as calculated by PBE-D2. The unit cell vectors are given in Angstrom. Atomic positions are given in fraction of the unit cell vectors.

	Vector	x	y	z	No	Atom	a	b	c
	a	9.75	0.56	0.00	29	Cu	0.53	0.65	0.98
	b	0.00	5.63	0.00	30	Cu	0.42	0.06	0.96
	c	0.00	0.00	20.00	31	Cu	0.31	0.47	0.95
No	Atom	a	b	c	32	Cu	0.21	0.88	0.94
1	C	0.92	0.70	0.11	33	Cu	0.09	0.29	0.93
2	C	0.97	0.94	0.22	34	Cu	0.98	0.70	0.92
3	C	0.03	0.83	0.15	35	Cu	0.86	0.11	0.91
4	C	0.40	0.57	0.18	36	Cu	0.75	0.53	0.90
5	C	0.41	0.52	0.11	37	Cu	0.64	0.94	0.89
6	C	0.46	0.26	0.10	38	Cu	0.52	0.35	0.88
7	H	0.88	0.06	0.20	39	Cu	0.41	0.76	0.87
8	H	0.94	0.80	0.25	40	Cu	0.29	0.17	0.86
9	H	0.03	0.18	0.12	41	Cu	0.18	0.58	0.85
10	H	0.05	0.04	0.24	42	Cu	0.06	0.99	0.84
11	H	0.12	0.70	0.16	43	Cu	0.95	0.41	0.82
12	H	0.18	0.03	0.11	44	Cu	0.84	0.82	0.81
13	H	0.32	0.56	0.08	45	Cu	0.73	0.23	0.80
14	H	0.32	0.46	0.20	46	Cu	0.61	0.64	0.79
15	H	0.37	0.76	0.19	47	Cu	0.50	0.05	0.78
16	H	0.48	0.85	0.09	48	Cu	0.38	0.46	0.77
17	H	0.50	0.54	0.21	49	Cu	0.27	0.87	0.76
18	H	0.61	0.64	0.10	50	Cu	0.16	0.28	0.75
19	N	0.08	0.02	0.11	51	Cu	0.04	0.70	0.74
20	N	0.51	0.68	0.08	52	Cu	0.93	0.11	0.73
21	O	0.81	0.82	0.10	53	Cu	0.82	0.52	0.72
22	O	0.95	0.49	0.09	54	Cu	0.70	0.93	0.71
23	O	0.37	0.11	0.11	55	Cu	0.59	0.34	0.70
24	O	0.58	0.21	0.08	56	Cu	0.47	0.75	0.69
25	Cu	0.02	1.00	0.01	57	Cu	0.36	0.16	0.68
26	Cu	0.89	0.40	0.00	58	Cu	0.25	0.58	0.67
27	Cu	0.77	0.83	0.99	59	Cu	0.13	0.99	0.66
28	Cu	0.65	0.24	0.99	60	Cu	0.02	0.40	0.65

Table C.9: Unit cell vectors and fractional coordinates for the optimized adsorption geometry of dense alanine adlayer DL_1_90_b on Cu(3,1,17)^S as calculated by PBE-D2. The unit cell vectors are given in Angstrom. Atomic positions are given in fraction of the unit cell vectors.

	Vector	x	y	z	No	Atom	a	b	c
	a	9.75	0.56	0.00	29	Cu	0.54	0.64	0.97
	b	0.00	5.63	0.00	30	Cu	0.43	0.05	0.96
	c	0.00	0.00	20.00	31	Cu	0.31	0.48	0.96
No	Atom	a	b	c	32	Cu	0.20	0.89	0.94
1	C	0.17	0.15	0.13	33	Cu	0.09	0.29	0.93
2	C	0.24	0.10	0.19	34	Cu	0.97	0.70	0.92
3	C	0.27	0.22	0.07	35	Cu	0.86	0.11	0.91
4	C	0.63	0.75	0.20	36	Cu	0.75	0.53	0.90
5	C	0.65	0.69	0.13	37	Cu	0.63	0.94	0.89
6	C	0.70	0.44	0.12	38	Cu	0.52	0.35	0.88
7	H	0.04	0.87	0.14	39	Cu	0.40	0.76	0.87
8	H	0.09	0.29	0.13	40	Cu	0.29	0.18	0.86
9	H	0.17	0.04	0.23	41	Cu	0.18	0.58	0.85
10	H	0.18	0.80	0.09	42	Cu	0.07	0.99	0.84
11	H	0.29	0.25	0.21	43	Cu	0.95	0.41	0.82
12	H	0.32	0.95	0.19	44	Cu	0.84	0.82	0.81
13	H	0.55	0.71	0.10	45	Cu	0.73	0.23	0.80
14	H	0.55	0.63	0.22	46	Cu	0.61	0.64	0.79
15	H	0.58	0.94	0.21	47	Cu	0.50	0.05	0.78
16	H	0.71	0.03	0.11	48	Cu	0.38	0.46	0.77
17	H	0.72	0.73	0.23	49	Cu	0.27	0.87	0.76
18	H	0.84	0.82	0.11	50	Cu	0.16	0.28	0.75
19	N	0.10	0.93	0.10	51	Cu	0.04	0.70	0.74
20	N	0.74	0.86	0.09	52	Cu	0.93	0.11	0.73
21	O	0.26	0.43	0.05	53	Cu	0.82	0.52	0.72
22	O	0.35	0.06	0.05	54	Cu	0.70	0.93	0.71
23	O	0.62	0.28	0.13	55	Cu	0.59	0.34	0.70
24	O	0.83	0.40	0.10	56	Cu	0.47	0.75	0.69
25	Cu	0.00	0.99	0.01	57	Cu	0.36	0.16	0.68
26	Cu	0.88	0.41	0.01	58	Cu	0.25	0.58	0.67
27	Cu	0.76	0.83	0.99	59	Cu	0.13	0.99	0.66
28	Cu	0.65	0.24	0.98	60	Cu	0.02	0.40	0.65

Table C.10: Unit cell vectors and fractional coordinates for the optimized adsorption geometry of dense alanine adlayer L_2_270_a on Cu(3,1,17)^{S} as calculated by PBE-D2. The unit cell vectors are given in Angstrom. Atomic positions are given in fraction of the unit cell vectors.

	Vector	x	y	z	No	Atom	a	b	c
	a	9.75	0.56	0.00	29	Cu	0.54	0.67	0.98
	b	0.00	5.63	0.00	30	Cu	0.43	0.07	0.96
	c	0.00	0.00	20.00	31	Cu	0.30	0.48	0.95
No	Atom	a	b	c	32	Cu	0.20	0.88	0.94
1	C	0.93	0.69	0.11	33	Cu	0.09	0.29	0.93
2	C	0.04	0.88	0.21	34	Cu	0.98	0.70	0.92
3	C	0.06	0.80	0.14	35	Cu	0.86	0.11	0.91
4	C	0.43	0.42	0.08	36	Cu	0.75	0.53	0.90
5	C	0.52	0.26	0.12	37	Cu	0.63	0.94	0.89
6	C	0.53	0.35	0.20	38	Cu	0.52	0.35	0.88
7	H	0.96	0.02	0.22	39	Cu	0.41	0.76	0.87
8	H	0.02	0.73	0.25	40	Cu	0.30	0.17	0.86
9	H	0.05	0.17	0.12	41	Cu	0.18	0.58	0.85
10	H	0.14	0.96	0.23	42	Cu	0.07	0.99	0.83
11	H	0.15	0.67	0.14	43	Cu	0.95	0.41	0.82
12	H	0.20	0.02	0.09	44	Cu	0.84	0.82	0.81
13	H	0.43	0.34	0.22	45	Cu	0.73	0.23	0.80
14	H	0.49	0.07	0.12	46	Cu	0.61	0.64	0.79
15	H	0.56	0.53	0.20	47	Cu	0.50	0.05	0.78
16	H	0.60	0.24	0.23	48	Cu	0.38	0.46	0.77
17	H	0.70	0.42	0.10	49	Cu	0.27	0.87	0.76
18	H	0.73	0.12	0.11	50	Cu	0.16	0.28	0.75
19	N	0.09	0.01	0.10	51	Cu	0.04	0.70	0.74
20	N	0.66	0.26	0.09	52	Cu	0.93	0.11	0.73
21	O	0.83	0.82	0.10	53	Cu	0.82	0.52	0.72
22	O	0.95	0.47	0.10	54	Cu	0.70	0.93	0.71
23	O	0.34	0.32	0.05	55	Cu	0.59	0.34	0.70
24	O	0.46	0.63	0.07	56	Cu	0.47	0.75	0.69
25	Cu	0.01	1.00	0.01	57	Cu	0.36	0.16	0.68
26	Cu	0.89	0.41	0.00	58	Cu	0.25	0.58	0.67
27	Cu	0.77	0.82	0.99	59	Cu	0.13	0.99	0.66
28	Cu	0.66	0.24	0.99	60	Cu	0.02	0.40	0.65

Table C.11: Unit cell vectors and fractional coordinates for the optimized adsorption geometry of dense alanine adlayer D_1_90_a on Cu(3,1,17)^{S} as calculated by PBE-D2. The unit cell vectors are given in Angstrom. Atomic positions are given in fraction of the unit cell vectors.

	Vector	x	y	z	No	Atom	a	b	c
	a	9.75	0.56	0.00	29	Cu	0.55	0.65	0.98
	b	0.00	5.63	0.00	30	Cu	0.42	0.06	0.96
	c	0.00	0.00	20.00	31	Cu	0.31	0.49	0.96
No	Atom	a	b	c	32	Cu	0.20	0.89	0.94
1	C	0.17	0.16	0.13	33	Cu	0.09	0.30	0.93
2	C	0.09	0.36	0.17	34	Cu	0.98	0.70	0.92
3	C	0.26	0.23	0.08	35	Cu	0.86	0.12	0.91
4	C	0.73	0.79	0.15	36	Cu	0.75	0.52	0.90
5	C	0.62	0.61	0.13	37	Cu	0.63	0.94	0.89
6	C	0.69	0.38	0.10	38	Cu	0.52	0.35	0.88
7	H	0.00	0.94	0.14	39	Cu	0.41	0.76	0.87
8	H	0.24	0.07	0.17	40	Cu	0.29	0.17	0.86
9	H	0.02	0.30	0.20	41	Cu	0.18	0.58	0.85
10	H	0.14	0.81	0.10	42	Cu	0.07	0.99	0.84
11	H	0.16	0.48	0.19	43	Cu	0.95	0.41	0.82
12	H	0.03	0.46	0.13	44	Cu	0.84	0.82	0.81
13	H	0.43	0.63	0.09	45	Cu	0.73	0.23	0.80
14	H	0.51	0.89	0.09	46	Cu	0.61	0.64	0.79
15	H	0.67	0.94	0.18	47	Cu	0.50	0.05	0.78
16	H	0.78	0.85	0.11	48	Cu	0.38	0.46	0.77
17	H	0.80	0.70	0.19	49	Cu	0.27	0.87	0.76
18	H	0.56	0.56	0.18	50	Cu	0.16	0.28	0.75
19	N	0.08	0.97	0.11	51	Cu	0.04	0.70	0.74
20	N	0.52	0.71	0.08	52	Cu	0.93	0.11	0.73
21	O	0.26	0.44	0.06	53	Cu	0.82	0.52	0.72
22	O	0.33	0.05	0.05	54	Cu	0.70	0.93	0.71
23	O	0.61	0.23	0.08	55	Cu	0.59	0.34	0.70
24	O	0.82	0.36	0.10	56	Cu	0.47	0.75	0.69
25	Cu	1.00	0.00	0.01	57	Cu	0.36	0.16	0.68
26	Cu	0.89	0.42	0.00	58	Cu	0.25	0.58	0.67
27	Cu	0.78	0.82	0.99	59	Cu	0.13	0.99	0.66
28	Cu	0.65	0.22	0.98	60	Cu	0.02	0.40	0.65

Table C.12: Unit cell vectors and fractional coordinates for the optimized adsorption geometry of dense alanine adlayer D_1_90_b on Cu(3,1,17)^{S} as calculated by PBE-D2. The unit cell vectors are given in Angstrom. Atomic positions are given in fraction of the unit cell vectors.

	Vector	x	y	z	No	Atom	a	b	c
	a	9.75	0.56	0.00	29	Cu	0.54	0.64	0.97
	b	0.00	5.63	0.00	30	Cu	0.43	0.05	0.96
	c	0.00	0.00	20.00	31	Cu	0.31	0.48	0.96
No	Atom	a	b	c	32	Cu	0.20	0.89	0.94
1	C	0.19	0.13	0.13	33	Cu	0.08	0.30	0.93
2	C	0.10	0.33	0.16	34	Cu	0.97	0.70	0.92
3	C	0.28	0.21	0.08	35	Cu	0.86	0.11	0.91
4	C	0.61	0.76	0.20	36	Cu	0.75	0.53	0.90
5	C	0.63	0.71	0.13	37	Cu	0.63	0.94	0.89
6	C	0.68	0.45	0.12	38	Cu	0.52	0.35	0.88
7	H	0.04	0.89	0.14	39	Cu	0.40	0.76	0.87
8	H	0.26	0.05	0.17	40	Cu	0.29	0.18	0.86
9	H	0.03	0.26	0.20	41	Cu	0.18	0.58	0.85
10	H	0.17	0.80	0.09	42	Cu	0.06	0.99	0.84
11	H	0.16	0.46	0.19	43	Cu	0.95	0.41	0.82
12	H	0.03	0.42	0.13	44	Cu	0.84	0.82	0.81
13	H	0.53	0.74	0.10	45	Cu	0.73	0.23	0.80
14	H	0.54	0.64	0.22	46	Cu	0.61	0.64	0.79
15	H	0.58	0.94	0.21	47	Cu	0.50	0.05	0.78
16	H	0.69	0.04	0.11	48	Cu	0.38	0.46	0.77
17	H	0.71	0.73	0.23	49	Cu	0.27	0.87	0.76
18	H	0.82	0.84	0.12	50	Cu	0.16	0.28	0.75
19	N	0.10	0.94	0.10	51	Cu	0.04	0.70	0.74
20	N	0.73	0.87	0.09	52	Cu	0.93	0.11	0.73
21	O	0.26	0.42	0.05	53	Cu	0.82	0.52	0.72
22	O	0.36	0.04	0.05	54	Cu	0.70	0.93	0.71
23	O	0.59	0.29	0.13	55	Cu	0.59	0.34	0.70
24	O	0.81	0.40	0.10	56	Cu	0.47	0.75	0.69
25	Cu	0.00	0.00	0.01	57	Cu	0.36	0.16	0.68
26	Cu	0.88	0.41	0.01	58	Cu	0.25	0.58	0.67
27	Cu	0.76	0.83	0.99	59	Cu	0.13	0.99	0.66
28	Cu	0.65	0.24	0.98	60	Cu	0.02	0.40	0.65

Table C.13: Unit cell vectors and fractional coordinates for the optimized adsorption geometry of dense alanine adlayer D_2_90_b on Cu(3,1,17)^S as calculated by PBE-D2. The unit cell vectors are given in Angstrom. Atomic positions are given in fraction of the unit cell vectors.

	Vector	x	y	z	No	Atom	a	b	c
	a	9.75	0.56	0.00	29	Cu	0.53	0.65	0.97
	b	0.00	5.63	0.00	30	Cu	0.42	0.06	0.96
	c	0.00	0.00	20.00	31	Cu	0.31	0.47	0.95
No	Atom	a	b	c	32	Cu	0.21	0.88	0.94
1	C	0.91	0.70	0.11	33	Cu	0.09	0.29	0.93
2	C	0.11	0.68	0.19	34	Cu	0.98	0.70	0.92
3	C	0.00	0.84	0.16	35	Cu	0.86	0.11	0.91
4	C	0.45	0.56	0.19	36	Cu	0.75	0.52	0.90
5	C	0.43	0.52	0.11	37	Cu	0.63	0.94	0.89
6	C	0.46	0.26	0.10	38	Cu	0.52	0.35	0.88
7	H	0.16	0.56	0.16	39	Cu	0.41	0.76	0.87
8	H	0.06	0.58	0.23	40	Cu	0.29	0.17	0.86
9	H	0.03	0.18	0.12	41	Cu	0.18	0.58	0.85
10	H	0.19	0.79	0.22	42	Cu	0.06	0.99	0.84
11	H	0.94	0.95	0.19	43	Cu	0.95	0.41	0.82
12	H	0.17	0.01	0.11	44	Cu	0.84	0.82	0.81
13	H	0.33	0.58	0.10	45	Cu	0.73	0.23	0.80
14	H	0.37	0.46	0.22	46	Cu	0.61	0.64	0.79
15	H	0.43	0.75	0.20	47	Cu	0.50	0.05	0.78
16	H	0.50	0.84	0.09	48	Cu	0.38	0.46	0.77
17	H	0.55	0.51	0.20	49	Cu	0.27	0.87	0.76
18	H	0.62	0.63	0.09	50	Cu	0.16	0.28	0.75
19	N	0.07	0.01	0.11	51	Cu	0.04	0.70	0.74
20	N	0.52	0.67	0.07	52	Cu	0.93	0.11	0.73
21	O	0.80	0.82	0.09	53	Cu	0.82	0.52	0.72
22	O	0.94	0.49	0.10	54	Cu	0.70	0.93	0.71
23	O	0.36	0.12	0.11	55	Cu	0.59	0.34	0.70
24	O	0.58	0.19	0.08	56	Cu	0.47	0.75	0.69
25	Cu	0.01	0.99	0.01	57	Cu	0.36	0.16	0.68
26	Cu	0.89	0.40	0.00	58	Cu	0.25	0.58	0.67
27	Cu	0.77	0.82	0.99	59	Cu	0.13	0.99	0.66
28	Cu	0.65	0.24	0.98	60	Cu	0.02	0.40	0.65

Table C.14: Unit cell vectors and fractional coordinates for the optimized adsorption geometry of dense alanine adlayer D_2_270_a on Cu(3,1,17)^S as calculated by PBE-D2. The unit cell vectors are given in Angstrom. Atomic positions are given in fraction of the unit cell vectors.

	Vector	x	y	z	No	Atom	a	b	c
	a	9.75	0.56	0.00	29	Cu	0.54	0.66	0.97
	b	0.00	5.63	0.00	30	Cu	0.43	0.06	0.96
	c	0.00	0.00	20.00	31	Cu	0.30	0.47	0.95
No	Atom	a	b	c	32	Cu	0.20	0.88	0.94
1	C	0.91	0.68	0.12	33	Cu	0.09	0.29	0.93
2	C	0.16	0.63	0.16	34	Cu	0.98	0.70	0.92
3	C	0.04	0.80	0.15	35	Cu	0.86	0.11	0.91
4	C	0.43	0.41	0.08	36	Cu	0.75	0.52	0.90
5	C	0.52	0.29	0.13	37	Cu	0.63	0.94	0.89
6	C	0.47	0.06	0.16	38	Cu	0.52	0.35	0.88
7	H	0.19	0.56	0.11	39	Cu	0.41	0.76	0.87
8	H	0.14	0.49	0.19	40	Cu	0.29	0.17	0.86
9	H	0.03	0.16	0.12	41	Cu	0.18	0.58	0.85
10	H	0.25	0.72	0.18	42	Cu	0.07	0.99	0.84
11	H	0.00	0.88	0.20	43	Cu	0.95	0.41	0.82
12	H	0.17	0.02	0.10	44	Cu	0.84	0.82	0.81
13	H	0.38	0.10	0.19	45	Cu	0.73	0.23	0.80
14	H	0.54	0.42	0.17	46	Cu	0.61	0.64	0.79
15	H	0.46	0.93	0.12	47	Cu	0.50	0.05	0.78
16	H	0.55	0.99	0.20	48	Cu	0.38	0.46	0.77
17	H	0.72	0.39	0.10	49	Cu	0.27	0.87	0.76
18	H	0.71	0.10	0.11	50	Cu	0.16	0.28	0.75
19	N	0.07	0.00	0.10	51	Cu	0.04	0.70	0.74
20	N	0.66	0.25	0.09	52	Cu	0.93	0.11	0.73
21	O	0.81	0.81	0.10	53	Cu	0.82	0.52	0.72
22	O	0.93	0.46	0.10	54	Cu	0.70	0.93	0.71
23	O	0.34	0.28	0.05	55	Cu	0.59	0.34	0.70
24	O	0.45	0.62	0.06	56	Cu	0.47	0.75	0.69
25	Cu	0.01	0.99	0.01	57	Cu	0.36	0.16	0.68
26	Cu	0.89	0.41	1.00	58	Cu	0.25	0.58	0.67
27	Cu	0.77	0.82	0.99	59	Cu	0.13	0.99	0.66
28	Cu	0.66	0.23	0.99	60	Cu	0.02	0.40	0.65

APPENDIX D

STRUCTURAL INFORMATION FOR THE OPTIMIZED ADSORPTION GEOMETRY OF R-3MCHO ON COPPER SURFACES USING PBE-GGA

Table D.1: Unit cell vectors and fractional coordinates for the optimized adsorption geometry of R-3MCHO on unreconstructed Cu(100) as calculated by PBE-GGA. The unit cell vectors are given in Angstrom. Atomic positions are given in fraction of the unit cell vectors.

		x	y	z	No	Atom	a	b	c	No	Atom	a	b	c
	a	10.89	0.00	0.00	35	Cu	1.00	0.33	0.18	73	Cu	0.33	0.83	0.09
	b	0.00	10.89	0.00	36	Cu	0.17	0.50	0.18	74	Cu	0.50	0.67	0.09
	c	0.00	0.00	20.35	37	Cu	1.00	0.50	0.27	75	Cu	0.33	0.67	0.18
No	Atom	a	b	c	38	Cu	0.17	0.33	0.27	76	Cu	0.50	0.83	0.18
1	C	0.36	0.47	0.57	39	Cu	0.00	0.33	0.35	77	Cu	0.33	0.83	0.27
2	C	0.43	0.26	0.54	40	Cu	0.17	0.50	0.35	78	Cu	0.50	0.67	0.27
3	C	0.32	0.35	0.54	41	Cu	0.00	0.67	0.00	79	Cu	0.33	0.67	0.35
4	C	0.53	0.31	0.50	42	Cu	0.17	0.83	0.00	80	Cu	0.50	0.83	0.35
5	C	0.58	0.43	0.53	43	Cu	0.00	0.83	0.09	81	Cu	0.67	0.00	0.00
6	C	0.47	0.53	0.53	44	Cu	0.17	0.67	0.09	82	Cu	0.83	0.17	0.00
7	C	0.52	0.65	0.56	45	Cu	1.00	0.67	0.18	83	Cu	0.67	0.17	0.09
8	O	0.58	0.27	0.45	46	Cu	0.17	0.83	0.18	84	Cu	0.83	0.00	0.09
9	H	0.28	0.36	0.49	47	Cu	1.00	0.83	0.27	85	Cu	0.67	0.00	0.18
10	H	0.39	0.46	0.62	48	Cu	0.17	0.67	0.27	86	Cu	0.83	0.17	0.18
11	H	0.61	0.42	0.58	49	Cu	0.00	0.67	0.35	87	Cu	0.67	0.17	0.27
12	H	0.25	0.31	0.57	50	Cu	0.17	0.83	0.35	88	Cu	0.83	0.00	0.27
13	H	0.29	0.54	0.57	51	Cu	0.33	0.00	0.00	89	Cu	0.67	1.00	0.35
14	H	0.46	0.23	0.59	52	Cu	0.50	0.17	0.00	90	Cu	0.84	0.17	0.35
15	H	0.40	0.17	0.51	53	Cu	0.33	0.17	0.09	91	Cu	0.67	0.33	0.00
16	H	0.59	0.69	0.53	54	Cu	0.50	0.00	0.09	92	Cu	0.83	0.50	0.00
17	H	0.44	0.72	0.56	55	Cu	0.33	0.00	0.18	93	Cu	0.67	0.50	0.09
18	H	0.55	0.64	0.61	56	Cu	0.50	0.17	0.18	94	Cu	0.83	0.33	0.09
19	H	0.66	0.47	0.50	57	Cu	0.33	0.17	0.27	95	Cu	0.67	0.33	0.18
20	H	0.44	0.54	0.48	58	Cu	0.50	0.00	0.27	96	Cu	0.83	0.50	0.18
21	Cu	0.00	0.00	0.00	59	Cu	0.33	1.00	0.35	97	Cu	0.67	0.50	0.27
22	Cu	0.17	0.17	0.00	60	Cu	0.50	0.16	0.36	98	Cu	0.83	0.33	0.27
23	Cu	0.00	0.17	0.09	61	Cu	0.33	0.33	0.00	99	Cu	0.67	0.34	0.36
24	Cu	0.17	0.00	0.09	62	Cu	0.50	0.50	0.00	100	Cu	0.83	0.50	0.35
25	Cu	1.00	0.00	0.18	63	Cu	0.33	0.50	0.09	101	Cu	0.67	0.67	0.00
26	Cu	0.17	0.17	0.18	64	Cu	0.50	0.33	0.09	102	Cu	0.83	0.83	0.00
27	Cu	0.00	0.17	0.27	65	Cu	0.33	0.33	0.18	103	Cu	0.67	0.83	0.09
28	Cu	0.17	0.00	0.27	66	Cu	0.50	0.50	0.18	104	Cu	0.83	0.67	0.09
29	Cu	0.00	1.00	0.35	67	Cu	0.33	0.50	0.27	105	Cu	0.67	0.67	0.18
30	Cu	0.17	0.17	0.35	68	Cu	0.50	0.33	0.27	106	Cu	0.83	0.83	0.18
31	Cu	0.00	0.33	0.00	69	Cu	0.33	0.34	0.35	107	Cu	0.67	0.83	0.27
32	Cu	0.17	0.50	0.00	70	Cu	0.50	0.50	0.35	108	Cu	0.83	0.67	0.27
33	Cu	0.00	0.50	0.09	71	Cu	0.33	0.67	0.00	109	Cu	0.67	0.67	0.35
34	Cu	0.17	0.33	0.09	72	Cu	0.50	0.83	0.00	110	Cu	0.83	0.83	0.35

Table D.2: Unit cell vectors and fractional coordinates for the optimized adsorption geometry of R-3MCHO on unreconstructed Cu (110) as calculated by PBE-GGA. The unit cell vectors are given in Angstrom. Atomic positions are given in fraction of the unit cell vectors.

		x	y	z	No	Atom	a	b	c	No	Atom	a	b	c
	a	10.89	0.00	0.00	17	H	0.81	0.95	0.45	37	Cu	0.50	0.13	0.18
	b	0.00	10.26	0.00	18	H	0.68	0.92	0.50	38	Cu	0.50	0.38	0.19
	c	0.00	0.00	20.35	19	H	0.48	0.94	0.38	39	Cu	0.50	0.63	0.19
No	Atom	a	b	c	20	H	0.68	0.07	0.37	40	Cu	0.50	0.88	0.19
1	C	0.36	0.13	0.34	21	Cu	0.67	0.00	0.25	41	Cu	0.17	0.13	0.19
2	C	0.67	0.18	0.45	22	Cu	0.67	0.25	0.25	42	Cu	0.17	0.37	0.19
3	C	0.46	0.28	0.41	23	Cu	0.67	0.50	0.25	43	Cu	0.17	0.63	0.19
4	C	0.60	0.30	0.42	24	Cu	0.67	0.75	0.25	44	Cu	0.17	0.88	0.19
5	C	0.44	0.15	0.38	25	Cu	0.33	1.00	0.25	45	Cu	0.67	0.00	0.13
6	C	0.50	0.03	0.41	26	Cu	0.33	0.25	0.25	46	Cu	0.67	0.25	0.13
7	C	0.64	0.05	0.42	27	Cu	0.33	0.50	0.25	47	Cu	0.67	0.50	0.13
8	O	0.71	0.94	0.45	28	Cu	0.33	0.75	0.25	48	Cu	0.67	0.75	0.13
9	H	0.64	0.31	0.37	29	Cu	0.00	0.00	0.25	49	Cu	0.33	0.00	0.13
10	H	0.64	0.17	0.50	30	Cu	0.00	0.25	0.25	50	Cu	0.33	0.25	0.13
11	H	0.47	0.01	0.46	31	Cu	0.00	0.50	0.25	51	Cu	0.33	0.50	0.13
12	H	0.62	0.39	0.45	32	Cu	0.00	0.75	0.25	52	Cu	0.33	0.75	0.13
13	H	0.77	0.20	0.45	33	Cu	0.83	0.13	0.19	53	Cu	0.00	0.00	0.13
14	H	0.42	0.28	0.46	34	Cu	0.83	0.38	0.19	54	Cu	0.00	0.25	0.13
15	H	0.42	0.35	0.38	35	Cu	0.83	0.63	0.19	55	Cu	0.00	0.50	0.13
16	H	0.69	0.85	0.42	36	Cu	0.83	0.88	0.19	56	Cu	0.00	0.75	0.13

Table D.3: Unit cell vectors and fractional coordinates for the optimized adsorption geometry of R-3MCHO on unreconstructed Cu (111) as calculated by PBE-GGA. The unit cell vectors are given in Angstrom. Atomic positions are given in fraction of the unit cell vectors.

		x	y	z	No	Atom	a	b	c	No	Atom	a	b	c
	a	10.26	0.00	0.00	21	Cu	0.67	0.17	0.33	45	Cu	1.00	0.50	0.25
	b	5.13	8.89	0.00	22	Cu	0.41	0.17	0.33	46	Cu	0.75	0.50	0.25
	c	0.00	0.00	25.44	23	Cu	0.92	0.17	0.33	47	Cu	0.25	0.75	0.25
No	Atom	a	b	c	24	Cu	0.17	0.17	0.33	48	Cu	1.00	0.75	0.25
1	C	0.37	0.31	0.48	25	Cu	0.92	0.42	0.33	49	Cu	0.50	0.75	0.25
2	C	0.27	0.48	0.48	26	Cu	0.17	0.92	0.33	50	Cu	0.75	0.75	0.25
3	C	0.51	0.27	0.45	27	Cu	0.67	0.67	0.33	51	Cu	0.25	0.50	0.25
4	C	0.36	0.55	0.51	28	Cu	0.92	0.92	0.33	52	Cu	0.50	0.50	0.25
5	C	0.60	0.34	0.47	29	Cu	0.92	0.67	0.33	53	Cu	0.09	0.33	0.16
6	C	0.50	0.51	0.47	30	Cu	0.42	0.92	0.33	54	Cu	0.09	0.83	0.16
7	C	0.59	0.58	0.49	31	Cu	0.17	0.42	0.33	55	Cu	0.33	0.09	0.16
8	O	0.56	0.18	0.41	32	Cu	0.17	0.67	0.33	56	Cu	0.33	0.33	0.16
9	H	0.23	0.53	0.44	33	Cu	0.67	0.42	0.33	57	Cu	0.33	0.59	0.16
10	H	0.39	0.51	0.55	34	Cu	0.42	0.67	0.33	58	Cu	0.33	0.83	0.16
11	H	0.65	0.29	0.51	35	Cu	0.67	0.91	0.33	59	Cu	0.59	0.33	0.16
12	H	0.17	0.51	0.51	36	Cu	0.41	0.42	0.33	60	Cu	0.59	0.83	0.16
13	H	0.29	0.67	0.51	37	Cu	0.75	0.25	0.25	61	Cu	0.83	0.09	0.16
14	H	0.40	0.26	0.52	38	Cu	0.50	0.25	0.25	62	Cu	0.83	0.33	0.16
15	H	0.31	0.26	0.45	39	Cu	0.75	0.00	0.25	63	Cu	0.83	0.59	0.16
16	H	0.69	0.56	0.47	40	Cu	0.25	0.25	0.25	64	Cu	0.83	0.83	0.16
17	H	0.52	0.71	0.50	41	Cu	0.50	0.00	0.25	65	Cu	0.08	0.08	0.16
18	H	0.64	0.54	0.53	42	Cu	1.00	0.00	0.25	66	Cu	0.08	0.58	0.16
19	H	0.69	0.31	0.44	43	Cu	1.00	0.25	0.25	67	Cu	0.58	0.08	0.16
20	H	0.46	0.56	0.43	44	Cu	0.25	0.00	0.25	68	Cu	0.58	0.58	0.16

Table D.4: Unit cell vectors and fractional coordinates for the optimized adsorption geometry of R-3MCHO on unreconstructed Cu (221) as calculated by PBE-GGA. The unit cell vectors are given in Angstrom. Atomic positions are given in fraction of the unit cell vectors.

		x	y	z	No	Atom	a	b	c	No	Atom	a	b	c
	a	15.40	0.00	0.00	35	Cu	0.86	0.63	0.30	72	Cu	0.17	0.75	0.17
	b	0.00	10.26	0.00	36	Cu	0.86	0.88	0.30	73	Cu	0.67	0.00	0.17
	c	0.00	0.00	21.77	37	Cu	0.23	0.00	0.28	74	Cu	0.67	0.25	0.17
No	Atom	a	b	c	38	Cu	0.23	0.25	0.28	75	Cu	0.67	0.50	0.17
1	C	0.65	0.50	0.47	39	Cu	0.23	0.50	0.28	76	Cu	0.67	0.75	0.17
2	C	0.75	0.51	0.47	40	Cu	0.23	0.75	0.28	77	Cu	0.03	0.12	0.14
3	C	0.62	0.38	0.44	41	Cu	0.73	0.00	0.28	78	Cu	0.03	0.37	0.14
4	C	0.79	0.39	0.50	42	Cu	0.73	0.25	0.28	79	Cu	0.03	0.62	0.14
5	C	0.66	0.26	0.46	43	Cu	0.73	0.50	0.28	80	Cu	0.03	0.87	0.14
6	C	0.76	0.27	0.46	44	Cu	0.73	0.75	0.28	81	Cu	0.53	0.12	0.14
7	C	0.80	0.14	0.49	45	Cu	0.09	0.13	0.25	82	Cu	0.53	0.37	0.14
8	O	0.55	0.37	0.41	46	Cu	0.09	0.38	0.25	83	Cu	0.53	0.62	0.14
9	H	0.77	0.52	0.42	47	Cu	0.09	0.62	0.25	84	Cu	0.53	0.87	0.14
10	H	0.78	0.38	0.55	48	Cu	0.09	0.88	0.25	85	Cu	0.39	0.00	0.11
11	H	0.64	0.24	0.51	49	Cu	0.59	0.13	0.25	86	Cu	0.39	0.25	0.11
12	H	0.77	0.60	0.49	50	Cu	0.59	0.38	0.25	87	Cu	0.39	0.50	0.11
13	H	0.86	0.40	0.49	51	Cu	0.59	0.62	0.25	88	Cu	0.39	0.75	0.11
14	H	0.63	0.51	0.52	52	Cu	0.59	0.88	0.25	89	Cu	0.89	0.00	0.11
15	H	0.62	0.59	0.44	53	Cu	0.45	1.00	0.22	90	Cu	0.89	0.25	0.11
16	H	0.78	0.05	0.47	54	Cu	0.45	0.25	0.22	91	Cu	0.89	0.50	0.11
17	H	0.87	0.15	0.49	55	Cu	0.45	0.50	0.22	92	Cu	0.89	0.75	0.11
18	H	0.79	0.13	0.54	56	Cu	0.45	0.75	0.22	93	Cu	0.25	0.12	0.08
19	H	0.64	0.17	0.44	57	Cu	0.95	1.00	0.22	94	Cu	0.25	0.37	0.08
20	H	0.78	0.27	0.41	58	Cu	0.95	0.25	0.22	95	Cu	0.25	0.62	0.08
21	Cu	1.00	0.00	0.33	59	Cu	0.95	0.50	0.22	96	Cu	0.25	0.87	0.08
22	Cu	1.00	0.25	0.33	60	Cu	0.95	0.75	0.22	97	Cu	0.75	0.12	0.08
23	Cu	1.00	0.50	0.33	61	Cu	0.31	0.13	0.19	98	Cu	0.75	0.37	0.08
24	Cu	1.00	0.75	0.33	62	Cu	0.31	0.38	0.19	99	Cu	0.75	0.62	0.08
25	Cu	0.50	1.00	0.33	63	Cu	0.31	0.62	0.19	100	Cu	0.75	0.87	0.08
26	Cu	0.50	0.25	0.33	64	Cu	0.31	0.88	0.19	101	Cu	0.11	0.00	0.06
27	Cu	0.50	0.50	0.33	65	Cu	0.81	0.12	0.19	102	Cu	0.11	0.25	0.06
28	Cu	0.50	0.75	0.33	66	Cu	0.81	0.38	0.19	103	Cu	0.11	0.50	0.06
29	Cu	0.36	0.13	0.30	67	Cu	0.81	0.63	0.19	104	Cu	0.11	0.75	0.06
30	Cu	0.36	0.38	0.30	68	Cu	0.81	0.88	0.19	105	Cu	0.61	0.00	0.06
31	Cu	0.36	0.62	0.30	69	Cu	0.17	0.00	0.17	106	Cu	0.61	0.25	0.06
32	Cu	0.36	0.88	0.30	70	Cu	0.17	0.25	0.17	107	Cu	0.61	0.50	0.06
33	Cu	0.86	0.12	0.30	71	Cu	0.17	0.50	0.17	108	Cu	0.61	0.75	0.06
34	Cu	0.86	0.38	0.30										

Table D.5: Unit cell vectors and fractional coordinates for the optimized adsorption geometry of R-3MCHO on unreconstructed Cu $(643)^R$ as calculated by PBE-GGA. The unit cell vectors are given in Angstrom. Atomic positions are given in fraction of the unit cell vectors.

		x	y	z	No	Atom	a	b	c	No	Atom	a	b	c
	a	6.34	2.43	0.00	16	H	0.24	0.05	0.52	35	Cu	0.36	0.49	0.18
	b	0.00	8.11	0.00	17	H	0.24	0.84	0.55	36	Cu	0.68	0.59	0.17
	c	0.00	0.00	21.72	18	H	0.40	0.94	0.58	37	Cu	0.99	0.70	0.16
No	Atom	a	b	c	19	H	0.57	0.06	0.46	38	Cu	0.30	0.81	0.15
1	C	0.97	0.65	0.45	20	H	0.45	0.81	0.45	39	Cu	0.61	0.91	0.14
2	C	0.82	0.55	0.47	21	Cu	0.00	0.00	0.33	40	Cu	0.92	0.02	0.13
3	C	0.86	0.85	0.45	22	Cu	0.31	0.11	0.32	41	Cu	0.23	0.13	0.12
4	C	0.65	0.64	0.51	23	Cu	0.62	0.21	0.31	42	Cu	0.54	0.24	0.10
5	C	0.66	0.94	0.48	24	Cu	0.94	0.31	0.30	43	Cu	0.86	0.35	0.09
6	C	0.52	0.82	0.49	25	Cu	0.25	0.42	0.29	44	Cu	0.16	0.45	0.09
7	C	0.34	0.92	0.54	26	Cu	0.56	0.52	0.28	45	Cu	0.48	0.56	0.07
8	O	0.93	0.94	0.42	27	Cu	0.88	0.63	0.27	46	Cu	0.79	0.66	0.06
9	H	0.75	0.53	0.42	28	Cu	0.19	0.74	0.26	47	Cu	0.10	0.77	0.05
10	H	0.73	0.65	0.56	29	Cu	0.50	0.84	0.25	48	Cu	0.41	0.88	0.04
11	H	0.70	-0.03	0.53	30	Cu	0.81	0.95	0.24	49	Cu	0.72	0.98	0.03
12	H	0.92	0.41	0.48	31	Cu	0.12	0.05	0.23	50	Cu	0.03	0.09	0.02
13	H	0.55	0.56	0.52	32	Cu	0.43	0.16	0.21	51	Cu	0.34	0.20	0.01
14	H	0.08	0.64	0.49	33	Cu	0.74	0.27	0.20	52	Cu	0.66	0.30	0.00
15	H	0.07	0.60	0.41	34	Cu	0.05	0.38	0.19					

Table D.6: Unit cell vectors and fractional coordinates for the optimized adsorption geometry of R-3MCHO on unreconstructed Cu (322) as calculated by PBE-GGA. The unit cell vectors are given in Angstrom. Atomic positions are given in fraction of the unit cell vectors.

		x	y	z	No	Atom	a	b	c	No	Atom	a	b	c
	a	8.30	6.04	0.00	25	Cu	0.18	0.21	0.27	53	Cu	0.16	0.65	0.13
	b	-8.30	7.05	0.00	26	Cu	0.68	0.20	0.27	54	Cu	0.66	0.65	0.13
	c	0.00	0.00	20.68	27	Cu	0.43	0.21	0.27	55	Cu	0.41	0.65	0.13
No	Atom	a	b	c	28	Cu	0.93	0.21	0.27	56	Cu	0.91	0.65	0.13
1	C	0.87	0.84	0.44	29	Cu	0.10	0.41	0.25	57	Cu	0.09	0.85	0.10
2	C	0.92	0.72	0.43	30	Cu	0.60	0.41	0.25	58	Cu	0.59	0.85	0.10
3	C	0.73	0.82	0.42	31	Cu	0.35	0.41	0.25	59	Cu	0.34	0.85	0.10
4	C	0.83	0.60	0.46	32	Cu	0.85	0.41	0.25	60	Cu	0.84	0.85	0.10
5	C	0.63	0.70	0.44	33	Cu	0.03	0.61	0.23	61	Cu	0.01	0.06	0.09
6	C	0.69	0.58	0.43	34	Cu	0.53	0.61	0.23	62	Cu	0.51	0.06	0.09
7	C	0.59	0.47	0.46	35	Cu	0.28	0.61	0.23	63	Cu	0.26	0.06	0.09
8	O	0.69	0.89	0.38	36	Cu	0.78	0.61	0.23	64	Cu	0.76	0.06	0.09
9	H	0.94	0.70	0.38	37	Cu	0.46	0.82	0.21	65	Cu	0.44	0.26	0.06
10	H	0.82	0.62	0.52	38	Cu	0.21	0.82	0.21	66	Cu	0.19	0.26	0.06
11	H	0.62	0.72	0.49	39	Cu	0.96	0.82	0.21	67	Cu	0.94	0.26	0.06
12	H	0.02	0.73	0.46	40	Cu	0.71	0.82	0.21	68	Cu	0.69	0.26	0.06
13	H	0.86	0.52	0.46	41	Cu	0.38	0.02	0.19	69	Cu	0.12	0.47	0.04
14	H	0.88	0.87	0.49	42	Cu	0.13	0.02	0.19	70	Cu	0.37	0.47	0.04
15	H	0.94	0.92	0.41	43	Cu	0.88	0.02	0.19	71	Cu	0.87	0.47	0.04
16	H	0.49	0.45	0.44	44	Cu	0.63	0.02	0.19	72	Cu	0.62	0.47	0.04
17	H	0.62	0.38	0.45	45	Cu	0.31	0.23	0.17	73	Cu	0.04	0.68	0.02
18	H	0.57	0.48	0.51	46	Cu	0.06	0.23	0.17	74	Cu	0.29	0.68	0.02
19	H	0.53	0.70	0.42	47	Cu	0.81	0.23	0.17	75	Cu	0.79	0.68	0.02
20	H	0.70	0.57	0.38	48	Cu	0.56	0.23	0.17	76	Cu	0.54	0.68	0.02
21	Cu	0.25	0.01	0.29	49	Cu	0.24	0.44	0.15	77	Cu	0.22	0.88	0.00
22	Cu	0.01	0.01	0.29	50	Cu	0.74	0.44	0.15	78	Cu	0.72	0.88	0.00
23	Cu	0.75	1.00	0.30	51	Cu	0.49	0.44	0.15	79	Cu	0.47	0.88	0.00
24	Cu	0.50	0.01	0.29	52	Cu	0.99	0.44	0.15	80	Cu	0.97	0.88	0.00

APPENDIX E

STRUCTURAL INFORMATION FOR THE OPTIMIZED ADSORPTION GEOMETRY OF R-3MCHO ON COPPER SURFACES USING PBE-D2

Table E.1: Unit cell vectors and fractional coordinates for the optimized adsorption geometry of R-3MCHO on unreconstructed Cu(100) as calculated by PBE-D2. The unit cell vectors are given in Angstrom. Atomic positions are given in fraction of the unit cell vectors.

		x	y	z	No	Atom	a	b	c	No	Atom	a	b	c
	a	10.70	0.00	0.00	23	Cu	0.84	0.50	0.36	49	Cu	0.17	0.00	0.27
	b	0.00	10.70	0.00	24	Cu	0.33	1.00	0.36	50	Cu	1.00	0.50	0.27
	c	0.00	0.00	20.00	25	Cu	0.50	0.83	0.36	51	Cu	0.33	0.83	0.27
No	Atom	a	b	c	26	Cu	0.00	0.33	0.36	52	Cu	1.00	0.83	0.27
1	C	0.34	0.50	0.54	27	Cu	0.83	0.83	0.36	53	Cu	0.16	0.33	0.27
2	C	0.40	0.27	0.53	28	Cu	0.67	0.67	0.36	54	Cu	0.50	0.67	0.27
3	C	0.30	0.38	0.52	29	Cu	0.00	1.00	0.36	55	Cu	0.17	0.67	0.27
4	C	0.52	0.32	0.50	30	Cu	0.17	0.17	0.36	56	Cu	0.33	0.50	0.27
5	C	0.57	0.45	0.52	31	Cu	0.67	1.00	0.36	57	Cu	0.00	0.00	0.18
6	C	0.46	0.54	0.51	32	Cu	0.84	0.17	0.36	58	Cu	0.00	0.33	0.18
7	C	0.51	0.68	0.52	33	Cu	0.00	0.67	0.36	59	Cu	0.00	0.67	0.18
8	O	0.57	0.26	0.45	34	Cu	0.17	0.83	0.36	60	Cu	0.17	0.17	0.18
9	H	0.27	0.38	0.47	35	Cu	0.17	0.50	0.36	61	Cu	0.17	0.50	0.18
10	H	0.36	0.51	0.60	36	Cu	0.33	0.67	0.36	62	Cu	0.17	0.83	0.18
11	H	0.59	0.44	0.57	37	Cu	0.33	0.34	0.36	63	Cu	0.33	0.00	0.18
12	H	0.22	0.34	0.55	38	Cu	0.50	0.50	0.35	64	Cu	0.33	0.33	0.18
13	H	0.27	0.57	0.53	39	Cu	0.67	0.17	0.27	65	Cu	0.33	0.67	0.18
14	H	0.42	0.26	0.58	40	Cu	0.83	0.33	0.27	66	Cu	0.50	0.17	0.18
15	H	0.37	0.19	0.50	41	Cu	0.50	0.33	0.27	67	Cu	0.50	0.50	0.18
16	H	0.59	0.70	0.50	42	Cu	0.50	0.00	0.27	68	Cu	0.50	0.83	0.18
17	H	0.43	0.74	0.51	43	Cu	0.67	0.50	0.27	69	Cu	0.67	0.00	0.18
18	H	0.53	0.68	0.58	44	Cu	0.33	0.17	0.27	70	Cu	0.67	0.33	0.18
19	H	0.65	0.47	0.49	45	Cu	0.83	0.00	0.27	71	Cu	0.67	0.67	0.18
20	H	0.44	0.54	0.45	46	Cu	0.67	0.83	0.27	72	Cu	0.83	0.17	0.18
21	Cu	0.67	0.34	0.36	47	Cu	0.00	0.17	0.27	73	Cu	0.83	0.50	0.18
22	Cu	0.49	0.16	0.36	48	Cu	0.83	0.67	0.27	74	Cu	0.83	0.83	0.18

Table E 2: Unit cell vectors and fractional coordinates for the optimized adsorption geometry of R-3MCHO on unreconstructed Cu (110) as calculated by PBE-D2. The unit cell vectors are given in Angstrom. Atomic positions are given in fraction of the unit cell vectors.

		x	y	z	No	Atom	a	b	c	No	Atom	a	b	c
	a	10.79	0.00	0.00	17	H	0.82	0.94	0.43	37	Cu	0.50	0.13	0.18
	b	0.00	10.18	0.00	18	H	0.69	0.91	0.49	38	Cu	0.50	0.37	0.19
	c	0.00	0.00	20.00	19	H	0.48	0.93	0.38	39	Cu	0.50	0.62	0.19
No	Atom	a	b	c	20	H	0.68	0.06	0.36	40	Cu	0.50	0.88	0.19
1	C	0.67	0.17	0.45	21	Cu	0.67	0.00	0.25	41	Cu	0.17	0.12	0.19
2	C	0.47	0.27	0.41	22	Cu	0.67	0.25	0.25	42	Cu	0.17	0.38	0.19
3	C	0.61	0.29	0.41	23	Cu	0.67	0.50	0.25	43	Cu	0.17	0.63	0.19
4	C	0.44	0.14	0.38	24	Cu	0.67	0.75	0.25	44	Cu	0.17	0.88	0.19
5	C	0.50	0.02	0.41	25	Cu	0.33	1.00	0.25	45	Cu	0.67	0.00	0.13
6	C	0.65	0.04	0.41	26	Cu	0.33	0.25	0.25	46	Cu	0.67	0.25	0.13
7	C	0.71	0.93	0.44	27	Cu	0.33	0.50	0.25	47	Cu	0.67	0.50	0.13
8	O	0.36	0.13	0.33	28	Cu	0.33	0.75	0.25	48	Cu	0.67	0.75	0.13
9	H	0.64	0.31	0.36	29	Cu	0.00	0.00	0.25	49	Cu	0.33	0.00	0.13
10	H	0.65	0.16	0.50	30	Cu	0.00	0.25	0.25	50	Cu	0.33	0.25	0.13
11	H	0.47	0.00	0.46	31	Cu	0.00	0.50	0.25	51	Cu	0.33	0.50	0.13
12	H	0.62	0.38	0.44	32	Cu	0.00	0.75	0.25	52	Cu	0.33	0.75	0.13
13	H	0.77	0.19	0.44	33	Cu	0.83	0.13	0.19	53	Cu	0.00	0.00	0.13
14	H	0.43	0.27	0.46	34	Cu	0.83	0.38	0.19	54	Cu	0.00	0.25	0.13
15	H	0.42	0.34	0.38	35	Cu	0.83	0.63	0.19	55	Cu	0.00	0.50	0.13
16	H	0.69	0.84	0.41	36	Cu	0.83	0.88	0.19	56	Cu	0.00	0.75	0.13

Table E.3: Unit cell vectors and fractional coordinates for the optimized adsorption geometry of R-3MCHO on unreconstructed Cu (111) as calculated by PBE-D2. The unit cell vectors are given in Angstrom. Atomic positions are given in fraction of the unit cell vectors.

		x	y	z	No	Atom	a	b	c	No	Atom	a	b	c
	a	10.09	0.00	0.00	21	Cu	0.67	0.17	0.33	45	Cu	1.00	0.50	0.24
	b	5.04	8.73	0.00	22	Cu	0.41	0.17	0.33	46	Cu	0.75	0.50	0.24
	c	0.00	0.00	25.00	23	Cu	0.92	0.17	0.33	47	Cu	0.25	0.75	0.25
No	Atom	a	b	c	24	Cu	0.16	0.17	0.33	48	Cu	1.00	0.75	0.24
1	C	0.54	0.19	0.40	25	Cu	0.92	0.42	0.33	49	Cu	0.50	0.75	0.24
2	C	0.35	0.32	0.47	26	Cu	0.17	0.92	0.33	50	Cu	0.75	0.75	0.25
3	C	0.26	0.50	0.46	27	Cu	0.67	0.67	0.33	51	Cu	0.25	0.50	0.24
4	C	0.50	0.27	0.44	28	Cu	0.92	0.92	0.33	52	Cu	0.50	0.50	0.24
5	C	0.34	0.58	0.48	29	Cu	0.92	0.67	0.33	53	Cu	0.09	0.33	0.16
6	C	0.59	0.34	0.46	30	Cu	0.42	0.92	0.33	54	Cu	0.09	0.83	0.16
7	C	0.49	0.52	0.45	31	Cu	0.16	0.42	0.33	55	Cu	0.33	0.09	0.16
8	O	0.58	0.60	0.47	32	Cu	0.16	0.67	0.33	56	Cu	0.33	0.33	0.16
9	H	0.22	0.53	0.42	33	Cu	0.67	0.42	0.33	57	Cu	0.33	0.59	0.16
10	H	0.36	0.57	0.52	34	Cu	0.42	0.67	0.33	58	Cu	0.33	0.83	0.16
11	H	0.63	0.32	0.50	35	Cu	0.67	0.91	0.32	59	Cu	0.59	0.33	0.16
12	H	0.15	0.54	0.49	36	Cu	0.41	0.42	0.32	60	Cu	0.59	0.83	0.16
13	H	0.27	0.71	0.47	37	Cu	0.75	0.25	0.25	61	Cu	0.83	0.09	0.16
14	H	0.38	0.29	0.51	38	Cu	0.50	0.25	0.25	62	Cu	0.83	0.33	0.16
15	H	0.30	0.27	0.45	39	Cu	0.75	0.00	0.25	63	Cu	0.83	0.59	0.16
16	H	0.69	0.56	0.45	40	Cu	0.25	0.25	0.25	64	Cu	0.83	0.83	0.16
17	H	0.51	0.72	0.46	41	Cu	0.50	0.00	0.25	65	Cu	0.08	0.08	0.16
18	H	0.61	0.58	0.51	42	Cu	1.00	0.00	0.25	66	Cu	0.08	0.58	0.16
19	H	0.70	0.30	0.43	43	Cu	1.00	0.25	0.25	67	Cu	0.58	0.08	0.16
20	H	0.47	0.54	0.41	44	Cu	0.25	0.00	0.25	68	Cu	0.58	0.58	0.16

Table E.4: Unit cell vectors and fractional coordinates for the optimized adsorption geometry of R-3MCHO on unreconstructed Cu (221) as calculated by PBE-D2. The unit cell vectors are given in Angstrom. Atomic positions are given in fraction of the unit cell vectors.

		x	y	z	No	Atom	a	b	c	No	Atom	a	b	c
	a	15.13	0.00	0.00	35	Cu	0.86	0.63	0.31	72	Cu	0.17	0.75	0.17
	b	0.00	10.09	0.00	36	Cu	0.86	0.87	0.31	73	Cu	0.67	0.00	0.17
	c	0.00	0.00	21.39	37	Cu	0.23	0.00	0.28	74	Cu	0.67	0.25	0.17
No	Atom	a	b	c	38	Cu	0.23	0.25	0.28	75	Cu	0.67	0.50	0.17
1	C	0.68	0.51	0.44	39	Cu	0.22	0.50	0.28	76	Cu	0.67	0.75	0.17
2	C	0.78	0.52	0.45	40	Cu	0.23	0.75	0.28	77	Cu	0.03	0.12	0.14
3	C	0.64	0.38	0.42	41	Cu	0.72	0.00	0.28	78	Cu	0.03	0.37	0.14
4	C	0.82	0.39	0.48	42	Cu	0.73	0.25	0.28	79	Cu	0.03	0.62	0.14
5	C	0.69	0.26	0.44	43	Cu	0.73	0.50	0.28	80	Cu	0.03	0.87	0.14
6	C	0.79	0.27	0.44	44	Cu	0.72	0.75	0.28	81	Cu	0.53	0.12	0.14
7	C	0.83	0.14	0.46	45	Cu	0.09	0.12	0.25	82	Cu	0.53	0.37	0.14
8	O	0.56	0.38	0.40	46	Cu	0.09	0.38	0.25	83	Cu	0.53	0.62	0.14
9	H	0.81	0.53	0.40	47	Cu	0.09	0.63	0.25	84	Cu	0.53	0.87	0.14
10	H	0.79	0.38	0.53	48	Cu	0.09	0.88	0.25	85	Cu	0.39	0.00	0.11
11	H	0.66	0.22	0.48	49	Cu	0.59	0.13	0.25	86	Cu	0.39	0.25	0.11
12	H	0.80	0.61	0.47	50	Cu	0.59	0.38	0.25	87	Cu	0.39	0.50	0.11
13	H	0.89	0.40	0.48	51	Cu	0.59	0.62	0.25	88	Cu	0.39	0.75	0.11
14	H	0.65	0.54	0.48	52	Cu	0.59	0.88	0.25	89	Cu	0.89	0.00	0.11
15	H	0.66	0.59	0.41	53	Cu	0.45	1.00	0.22	90	Cu	0.89	0.25	0.11
16	H	0.82	0.06	0.43	54	Cu	0.45	0.25	0.22	91	Cu	0.89	0.50	0.11
17	H	0.91	0.15	0.46	55	Cu	0.45	0.50	0.22	92	Cu	0.89	0.75	0.11
18	H	0.81	0.12	0.51	56	Cu	0.45	0.75	0.22	93	Cu	0.25	0.12	0.08
19	H	0.67	0.18	0.40	57	Cu	0.95	1.00	0.22	94	Cu	0.25	0.37	0.08
20	H	0.82	0.29	0.39	58	Cu	0.95	0.25	0.22	95	Cu	0.25	0.62	0.08
21	Cu	0.00	0.00	0.33	59	Cu	0.95	0.50	0.22	96	Cu	0.25	0.87	0.08
22	Cu	0.00	0.25	0.33	60	Cu	0.95	0.75	0.22	97	Cu	0.75	0.12	0.08
23	Cu	0.00	0.50	0.33	61	Cu	0.31	0.13	0.20	98	Cu	0.75	0.37	0.08
24	Cu	0.00	0.75	0.33	62	Cu	0.31	0.37	0.20	99	Cu	0.75	0.62	0.08
25	Cu	0.50	1.00	0.33	63	Cu	0.31	0.62	0.20	100	Cu	0.75	0.87	0.08
26	Cu	0.51	0.25	0.33	64	Cu	0.31	0.88	0.20	101	Cu	0.11	0.00	0.06
27	Cu	0.51	0.50	0.33	65	Cu	0.81	0.12	0.20	102	Cu	0.11	0.25	0.06
28	Cu	0.50	0.75	0.33	66	Cu	0.81	0.38	0.20	103	Cu	0.11	0.50	0.06
29	Cu	0.37	0.13	0.31	67	Cu	0.81	0.63	0.20	104	Cu	0.11	0.75	0.06
30	Cu	0.36	0.37	0.31	68	Cu	0.81	0.87	0.20	105	Cu	0.61	0.00	0.06
31	Cu	0.37	0.63	0.31	69	Cu	0.17	0.00	0.17	106	Cu	0.61	0.25	0.06
32	Cu	0.36	0.88	0.31	70	Cu	0.17	0.25	0.17	107	Cu	0.61	0.50	0.06
33	Cu	0.86	0.12	0.31	71	Cu	0.17	0.50	0.17	108	Cu	0.61	0.75	0.06
34	Cu	0.86	0.38	0.31										

Table E.5: Unit cell vectors and fractional coordinates for the optimized adsorption geometry of R-3MCHO on unreconstructed Cu $(643)^R$ as calculated by PBE-D2. The unit cell vectors are given in Angstrom. Atomic positions are given in fraction of the unit cell vectors.

		x	y	z	No	Atom	a	b	c	No	Atom	a	b	c
	a	6.23	2.39	0.00	16	H	0.13	0.97	0.49	35	Cu	0.37	0.49	0.18
	b	0.00	7.97	0.00	17	H	0.18	0.75	0.52	36	Cu	0.68	0.59	0.17
	c	0.00	0.00	21.34	18	H	0.32	0.89	0.55	37	Cu	0.99	0.70	0.16
No	Atom	a	b	c	19	H	0.46	0.99	0.41	38	Cu	0.30	0.80	0.15
1	C	0.91	0.64	0.42	20	H	0.38	0.73	0.42	39	Cu	0.61	0.91	0.14
2	C	0.79	0.51	0.44	21	Cu	0.01	0.98	0.33	40	Cu	0.92	0.02	0.13
3	C	0.78	0.84	0.43	22	Cu	0.32	0.10	0.32	41	Cu	0.23	0.13	0.12
4	C	0.61	0.60	0.49	23	Cu	0.63	0.20	0.31	42	Cu	0.54	0.24	0.11
5	C	0.54	0.91	0.45	24	Cu	0.94	0.31	0.30	43	Cu	0.86	0.35	0.09
6	C	0.44	0.77	0.46	25	Cu	0.25	0.42	0.29	44	Cu	0.16	0.45	0.09
7	C	0.26	0.85	0.51	26	Cu	0.57	0.52	0.28	45	Cu	0.48	0.56	0.07
8	O	0.86	0.95	0.41	27	Cu	0.88	0.63	0.27	46	Cu	0.79	0.66	0.06
9	H	0.72	0.48	0.40	28	Cu	0.19	0.73	0.26	47	Cu	0.10	0.77	0.05
10	H	0.68	0.63	0.53	29	Cu	0.50	0.84	0.25	48	Cu	0.41	0.88	0.04
11	H	0.53	0.00	0.48	30	Cu	0.81	0.94	0.24	49	Cu	0.72	0.98	0.03
12	H	0.91	0.39	0.46	31	Cu	0.12	0.05	0.23	50	Cu	0.03	0.09	0.02
13	H	0.54	0.50	0.50	32	Cu	0.43	0.16	0.21	51	Cu	0.34	0.20	0.01
14	H	0.05	0.62	0.45	33	Cu	0.74	0.27	0.20	52	Cu	0.66	0.30	0.00
15	H	0.96	0.62	0.37	34	Cu	0.06	0.38	0.19					

Table E.6: Unit cell vectors and fractional coordinates for the optimized adsorption geometry of R-3MCHO on reconstructed Cu (110) as calculated by PBE-D2. The unit cell vectors are given in Angstrom. Atomic positions are given in fraction of the unit cell vectors.

		x	y	z	No	Atom	a	b	c	No	Atom	a	b	c
	a	14.26	0.00	0.00	24	Cu	0.01	0.75	0.24	51	Cu	0.25	0.50	0.13
	b	0.00	10.09	0.00	25	Cu	0.53	1.00	0.24	52	Cu	0.25	0.75	0.13
	c	0.00	0.00	20.00	26	Cu	0.53	0.25	0.24	53	Cu	0.50	0.00	0.12
No	Atom	a	b	c	27	Cu	0.53	0.50	0.24	54	Cu	0.50	0.25	0.12
1	C	0.37	0.50	0.41	28	Cu	0.53	0.75	0.24	55	Cu	0.50	0.50	0.12
2	C	0.30	0.27	0.38	29	Cu	0.15	0.13	0.21	56	Cu	0.50	0.75	0.12
3	C	0.29	0.43	0.37	30	Cu	0.16	0.37	0.21	57	Cu	0.75	1.00	0.12
4	C	0.39	0.23	0.36	31	Cu	0.15	0.62	0.21	58	Cu	0.75	0.25	0.12
5	C	0.47	0.29	0.39	32	Cu	0.16	0.88	0.21	59	Cu	0.75	0.50	0.12
6	C	0.47	0.45	0.38	33	Cu	0.33	0.12	0.22	60	Cu	0.75	0.75	0.12
7	C	0.55	0.52	0.41	34	Cu	0.38	0.37	0.19	61	Cu	0.13	0.13	0.06
8	O	0.40	0.15	0.31	35	Cu	0.37	0.62	0.20	62	Cu	0.13	0.38	0.06
9	H	0.29	0.45	0.32	36	Cu	0.38	0.88	0.19	63	Cu	0.13	0.63	0.06
10	H	0.37	0.48	0.46	37	Cu	0.68	0.12	0.22	64	Cu	0.13	0.88	0.06
11	H	0.47	0.27	0.45	38	Cu	0.68	0.37	0.22	65	Cu	0.38	0.13	0.06
12	H	0.22	0.46	0.39	39	Cu	0.68	0.62	0.22	66	Cu	0.38	0.38	0.06
13	H	0.37	0.60	0.40	40	Cu	0.68	0.87	0.22	67	Cu	0.38	0.63	0.06
14	H	0.29	0.25	0.43	41	Cu	0.86	0.13	0.20	68	Cu	0.38	0.88	0.06
15	H	0.24	0.22	0.35	42	Cu	0.86	0.38	0.21	69	Cu	0.63	0.13	0.06
16	H	0.62	0.48	0.39	43	Cu	0.86	0.63	0.20	70	Cu	0.63	0.38	0.06
17	H	0.55	0.62	0.41	44	Cu	0.86	0.87	0.21	71	Cu	0.63	0.63	0.06
18	H	0.55	0.50	0.47	45	Cu	0.00	0.00	0.12	72	Cu	0.63	0.88	0.06
19	H	0.54	0.25	0.37	46	Cu	0.00	0.25	0.12	73	Cu	0.88	0.13	0.06
20	H	0.47	0.46	0.33	47	Cu	0.00	0.50	0.12	74	Cu	0.88	0.38	0.06
21	Cu	0.01	1.00	0.24	48	Cu	0.00	0.75	0.12	75	Cu	0.88	0.63	0.06
22	Cu	0.01	0.25	0.24	49	Cu	0.25	0.00	0.13	76	Cu	0.88	0.88	0.06
23	Cu	0.01	0.50	0.24	50	Cu	0.25	0.25	0.13					

Table E.7: Unit cell vectors and fractional coordinates for the optimized adsorption geometry of R-3MCHO on Cu (322) as calculated by PBE-D2. The unit cell vectors are given in Angstrom. Atomic positions are given in fraction of the unit cell vectors.

		x	y	z	No	Atom	a	b	c	No	Atom	a	b	c
	a	8.16	5.93	0.00	25	Cu	0.18	0.20	0.28	53	Cu	0.16	0.65	0.13
	b	-8.16	6.92	0.00	26	Cu	0.68	0.20	0.28	54	Cu	0.66	0.65	0.13
	c	0.00	0.00	20.32	27	Cu	0.43	0.20	0.28	55	Cu	0.41	0.64	0.13
No	Atom	a	b	c	28	Cu	0.93	0.20	0.28	56	Cu	0.91	0.65	0.13
1	C	0.61	0.90	0.36	29	Cu	0.10	0.41	0.26	57	Cu	0.09	0.85	0.11
2	C	0.72	0.75	0.41	30	Cu	0.60	0.41	0.26	58	Cu	0.59	0.85	0.11
3	C	0.71	0.60	0.41	31	Cu	0.35	0.40	0.25	59	Cu	0.34	0.85	0.11
4	C	0.60	0.79	0.39	32	Cu	0.85	0.41	0.26	60	Cu	0.84	0.85	0.11
5	C	0.57	0.53	0.44	33	Cu	0.03	0.61	0.24	61	Cu	0.01	0.06	0.09
6	C	0.46	0.71	0.40	34	Cu	0.53	0.61	0.24	62	Cu	0.51	0.06	0.09
7	C	0.45	0.56	0.40	35	Cu	0.28	0.61	0.24	63	Cu	0.26	0.06	0.09
8	O	0.32	0.48	0.42	36	Cu	0.78	0.61	0.24	64	Cu	0.76	0.06	0.09
9	H	0.72	0.57	0.36	37	Cu	0.45	0.82	0.21	65	Cu	0.44	0.26	0.06
10	H	0.57	0.56	0.49	38	Cu	0.20	0.82	0.22	66	Cu	0.19	0.26	0.06
11	H	0.43	0.73	0.45	39	Cu	0.95	0.82	0.22	67	Cu	0.94	0.26	0.06
12	H	0.80	0.58	0.44	40	Cu	0.70	0.82	0.21	68	Cu	0.69	0.26	0.06
13	H	0.57	0.43	0.44	41	Cu	0.38	0.02	0.19	69	Cu	0.12	0.47	0.04
14	H	0.75	0.79	0.46	42	Cu	0.13	0.02	0.19	70	Cu	0.37	0.47	0.04
15	H	0.81	0.80	0.37	43	Cu	0.88	0.02	0.19	71	Cu	0.87	0.47	0.04
16	H	0.23	0.50	0.39	44	Cu	0.63	0.02	0.19	72	Cu	0.62	0.47	0.04
17	H	0.31	0.38	0.41	45	Cu	0.31	0.23	0.17	73	Cu	0.04	0.68	0.02
18	H	0.29	0.50	0.47	46	Cu	0.06	0.23	0.17	74	Cu	0.29	0.68	0.02
19	H	0.39	0.73	0.36	47	Cu	0.81	0.23	0.17	75	Cu	0.79	0.68	0.02
20	H	0.47	0.54	0.35	48	Cu	0.56	0.23	0.17	76	Cu	0.54	0.68	0.02
21	Cu	0.25	1.00	0.30	49	Cu	0.23	0.44	0.15	77	Cu	0.22	0.88	0.00
22	Cu	0.00	1.00	0.30	50	Cu	0.73	0.44	0.15	78	Cu	0.72	0.88	0.00
23	Cu	0.76	1.00	0.30	51	Cu	0.48	0.44	0.15	79	Cu	0.47	0.88	0.00
24	Cu	0.49	0.99	0.30	52	Cu	0.98	0.44	0.15	80	Cu	0.97	0.88	0.00

APPENDIX F

STRUCTURAL INFORMATION FOR THE OPTIMIZED ADSORPTION GEOMETRY OF R-3MCHO ON COPPER SURFACES USING PBE-B86b

Table F.1: Unit cell vectors and fractional coordinates for the optimized adsorption geometry of R-3MCHO on unreconstructed Cu(100) as calculated by PBE-B86b. The unit cell vectors are given in Angstrom. Atomic positions are given in fraction of the unit cell vectors.

		x	y	z	No	Atom	a	b	c	No	Atom	a	b	c
	a	10.79	0.00	0.00	23	Cu	0.84	0.50	0.35	49	Cu	0.17	0.00	0.27
	b	0.00	10.79	0.00	24	Cu	0.33	1.00	0.35	50	Cu	1.00	0.50	0.27
	c	0.00	0.00	20.18	25	Cu	0.50	0.83	0.35	51	Cu	0.33	0.83	0.27
No	Atom	a	b	c	26	Cu	0.00	0.33	0.35	52	Cu	1.00	0.83	0.27
1	C	0.35	0.50	0.54	27	Cu	0.83	0.83	0.35	53	Cu	0.16	0.33	0.27
2	C	0.41	0.27	0.52	28	Cu	0.67	0.67	0.35	54	Cu	0.50	0.67	0.26
3	C	0.31	0.37	0.52	29	Cu	0.00	1.00	0.35	55	Cu	0.17	0.67	0.27
4	C	0.53	0.32	0.49	30	Cu	0.17	0.17	0.35	56	Cu	0.33	0.50	0.26
5	C	0.57	0.44	0.51	31	Cu	0.67	1.00	0.35	57	Cu	0.00	0.00	0.18
6	C	0.47	0.54	0.50	32	Cu	0.84	0.17	0.35	58	Cu	0.00	0.33	0.18
7	C	0.51	0.67	0.53	33	Cu	0.00	0.67	0.35	59	Cu	0.00	0.67	0.18
8	O	0.57	0.27	0.44	34	Cu	0.17	0.83	0.35	60	Cu	0.17	0.17	0.18
9	H	0.28	0.38	0.46	35	Cu	0.17	0.50	0.35	61	Cu	0.17	0.50	0.18
10	H	0.36	0.50	0.59	36	Cu	0.33	0.67	0.35	62	Cu	0.17	0.83	0.18
11	H	0.60	0.44	0.57	37	Cu	0.33	0.34	0.35	63	Cu	0.33	0.00	0.18
12	H	0.23	0.34	0.54	38	Cu	0.50	0.50	0.35	64	Cu	0.33	0.33	0.18
13	H	0.27	0.57	0.53	39	Cu	0.67	0.17	0.27	65	Cu	0.33	0.67	0.18
14	H	0.43	0.26	0.58	40	Cu	0.83	0.33	0.27	66	Cu	0.50	0.17	0.18
15	H	0.38	0.18	0.50	41	Cu	0.50	0.33	0.27	67	Cu	0.50	0.50	0.18
16	H	0.59	0.70	0.50	42	Cu	0.50	0.00	0.27	68	Cu	0.50	0.83	0.18
17	H	0.44	0.74	0.52	43	Cu	0.67	0.50	0.27	69	Cu	0.67	0.00	0.18
18	H	0.53	0.67	0.58	44	Cu	0.33	0.17	0.27	70	Cu	0.67	0.33	0.18
19	H	0.66	0.47	0.49	45	Cu	0.83	0.00	0.27	71	Cu	0.67	0.67	0.18
20	H	0.45	0.55	0.45	46	Cu	0.67	0.83	0.27	72	Cu	0.83	0.17	0.18
21	Cu	0.67	0.34	0.36	47	Cu	0.00	0.17	0.27	73	Cu	0.83	0.50	0.18
22	Cu	0.50	0.16	0.36	48	Cu	0.83	0.67	0.27	74	Cu	0.83	0.83	0.18

Table F.2: Unit cell vectors and fractional coordinates for the optimized adsorption geometry of R-3MCHO on unreconstructed Cu (110) as calculated by PBE-B86b. The unit cell vectors are given in Angstrom. Atomic positions are given in fraction of the unit cell vectors.

		x	y	z	No	Atom	a	b	c	No	Atom	a	b	c
	a	10.79	0.00	0.00	17	H	0.82	0.94	0.43	37	Cu	0.50	0.13	0.18
	b	0.00	10.18	0.00	18	H	0.69	0.91	0.49	38	Cu	0.50	0.37	0.19
	c	0.00	0.00	20.00	19	H	0.48	0.93	0.38	39	Cu	0.50	0.62	0.19
No	Atom	a	b	c	20	H	0.68	0.06	0.36	40	Cu	0.50	0.88	0.19
1	C	0.67	0.17	0.45	21	Cu	0.67	0.00	0.25	41	Cu	0.17	0.12	0.19
2	C	0.47	0.27	0.41	22	Cu	0.67	0.25	0.25	42	Cu	0.17	0.38	0.19
3	C	0.61	0.29	0.41	23	Cu	0.67	0.50	0.25	43	Cu	0.17	0.63	0.19
4	C	0.44	0.14	0.38	24	Cu	0.67	0.75	0.25	44	Cu	0.17	0.88	0.19
5	C	0.50	0.02	0.41	25	Cu	0.33	1.00	0.25	45	Cu	0.67	0.00	0.13
6	C	0.65	0.04	0.41	26	Cu	0.33	0.25	0.25	46	Cu	0.67	0.25	0.13
7	C	0.71	0.93	0.44	27	Cu	0.33	0.50	0.25	47	Cu	0.67	0.50	0.13
8	O	0.36	0.13	0.33	28	Cu	0.33	0.75	0.25	48	Cu	0.67	0.75	0.13
9	H	0.64	0.31	0.36	29	Cu	0.00	0.00	0.25	49	Cu	0.33	0.00	0.13
10	H	0.65	0.16	0.50	30	Cu	0.00	0.25	0.25	50	Cu	0.33	0.25	0.13
11	H	0.47	0.00	0.46	31	Cu	0.00	0.50	0.25	51	Cu	0.33	0.50	0.13
12	H	0.62	0.38	0.44	32	Cu	0.00	0.75	0.25	52	Cu	0.33	0.75	0.13
13	H	0.77	0.19	0.44	33	Cu	0.83	0.13	0.19	53	Cu	0.00	0.00	0.13
14	H	0.43	0.27	0.46	34	Cu	0.83	0.38	0.19	54	Cu	0.00	0.25	0.13
15	H	0.42	0.34	0.38	35	Cu	0.83	0.63	0.19	55	Cu	0.00	0.50	0.13
16	H	0.69	0.84	0.41	36	Cu	0.83	0.88	0.19	56	Cu	0.00	0.75	0.13

Table F.3: Unit cell vectors and fractional coordinates for the optimized adsorption geometry of R-3MCHO on unreconstructed Cu (111) as calculated by PBE-B86b. The unit cell vectors are given in Angstrom. Atomic positions are given in fraction of the unit cell vectors.

		x	y	z	No	Atom	a	b	c	No	Atom	a	b	c
	a	10.18	0.00	0.00	21	Cu	0.67	0.17	0.33	45	Cu	0.25	0.75	0.25
	b	5.09	8.81	0.00	22	Cu	0.41	0.17	0.33	46	Cu	1.00	0.75	0.25
	c	0.00	0.00	25.00	23	Cu	0.92	0.17	0.33	47	Cu	0.50	0.75	0.25
No	Atom	a	b	c	24	Cu	0.17	0.92	0.33	48	Cu	1.00	0.50	0.25
1	C	0.35	0.32	0.48	25	Cu	0.17	0.17	0.33	49	Cu	0.75	0.50	0.25
2	C	0.25	0.50	0.48	26	Cu	0.92	0.92	0.33	50	Cu	0.75	0.75	0.25
3	C	0.50	0.27	0.45	27	Cu	0.92	0.42	0.33	51	Cu	0.25	0.50	0.25
4	C	0.34	0.58	0.50	28	Cu	0.42	0.92	0.33	52	Cu	0.50	0.50	0.25
5	C	0.59	0.34	0.47	29	Cu	0.92	0.67	0.33	53	Cu	0.09	0.33	0.16
6	C	0.49	0.52	0.47	30	Cu	0.67	0.67	0.33	54	Cu	0.09	0.83	0.16
7	C	0.58	0.60	0.48	31	Cu	0.16	0.67	0.33	55	Cu	0.33	0.09	0.16
8	O	0.54	0.18	0.41	32	Cu	0.17	0.42	0.33	56	Cu	0.33	0.33	0.16
9	H	0.22	0.53	0.43	33	Cu	0.42	0.67	0.33	57	Cu	0.33	0.59	0.16
10	H	0.36	0.56	0.54	34	Cu	0.67	0.91	0.33	58	Cu	0.33	0.83	0.16
11	H	0.62	0.32	0.52	35	Cu	0.67	0.42	0.33	59	Cu	0.59	0.33	0.16
12	H	0.15	0.53	0.50	36	Cu	0.41	0.42	0.33	60	Cu	0.59	0.83	0.16
13	H	0.27	0.70	0.49	37	Cu	0.75	0.00	0.25	61	Cu	0.83	0.09	0.16
14	H	0.38	0.29	0.52	38	Cu	0.50	0.25	0.25	62	Cu	0.83	0.33	0.16
15	H	0.30	0.26	0.46	39	Cu	0.75	0.25	0.25	63	Cu	0.83	0.59	0.16
16	H	0.68	0.56	0.46	40	Cu	0.50	0.00	0.25	64	Cu	0.83	0.83	0.16
17	H	0.51	0.72	0.48	41	Cu	0.25	0.25	0.25	65	Cu	0.08	0.08	0.16
18	H	0.60	0.58	0.53	42	Cu	1.00	0.00	0.25	66	Cu	0.08	0.58	0.16
19	H	0.70	0.30	0.45	43	Cu	0.25	0.00	0.25	67	Cu	0.58	0.08	0.16
20	H	0.46	0.54	0.42	44	Cu	1.00	0.25	0.25	68	Cu	0.58	0.58	0.16

APPENDIX G

STRUCTURAL INFORMATION FOR THE OPTIMIZED ADSORPTION GEOMETRY OF R-3MCHO ON COPPER SURFACES USING PBE-B88

Table G.1: Unit cell vectors and fractional coordinates for the optimized adsorption geometry of R-3MCHO on unreconstructed Cu(100) as calculated by PBE-B88. The unit cell vectors are given in Angstrom. Atomic positions are given in fraction of the unit cell vectors.

		x	y	z	No	Atom	a	b	c	No	Atom	a	b	c
	a	10.88	0.00	0.00	35	Cu	1.00	0.33	0.18	73	Cu	0.33	0.83	0.09
	b	0.00	10.88	0.00	36	Cu	0.17	0.50	0.18	74	Cu	0.50	0.67	0.09
	c	0.00	0.00	20.33	37	Cu	1.00	0.50	0.27	75	Cu	0.33	0.67	0.18
No	Atom	a	b	c	38	Cu	0.17	0.33	0.27	76	Cu	0.50	0.83	0.18
1	C	0.36	0.49	0.55	39	Cu	1.00	0.33	0.35	77	Cu	0.33	0.83	0.27
2	C	0.42	0.26	0.53	40	Cu	0.17	0.50	0.35	78	Cu	0.50	0.67	0.27
3	C	0.32	0.36	0.53	41	Cu	0.00	0.67	0.00	79	Cu	0.33	0.67	0.35
4	C	0.54	0.31	0.50	42	Cu	0.17	0.83	0.00	80	Cu	0.50	0.83	0.35
5	C	0.58	0.43	0.52	43	Cu	0.00	0.83	0.09	81	Cu	0.67	0.00	0.00
6	C	0.48	0.53	0.52	44	Cu	0.17	0.67	0.09	82	Cu	0.83	0.17	0.00
7	C	0.52	0.66	0.54	45	Cu	1.00	0.67	0.18	83	Cu	0.67	0.17	0.09
8	O	0.58	0.27	0.45	46	Cu	0.17	0.83	0.18	84	Cu	0.83	0.00	0.09
9	H	0.29	0.37	0.48	47	Cu	1.00	0.83	0.27	85	Cu	0.67	0.00	0.18
10	H	0.38	0.48	0.61	48	Cu	0.17	0.67	0.27	86	Cu	0.83	0.17	0.18
11	H	0.61	0.43	0.58	49	Cu	0.00	0.67	0.35	87	Cu	0.67	0.17	0.27
12	H	0.24	0.33	0.56	50	Cu	0.17	0.83	0.35	88	Cu	0.83	0.00	0.27
13	H	0.29	0.55	0.55	51	Cu	0.33	0.00	0.00	89	Cu	0.67	1.00	0.35
14	H	0.45	0.25	0.58	52	Cu	0.50	0.17	0.00	90	Cu	0.84	0.17	0.35
15	H	0.40	0.18	0.51	53	Cu	0.33	0.17	0.09	91	Cu	0.67	0.33	0.00
16	H	0.60	0.69	0.51	54	Cu	0.50	0.00	0.09	92	Cu	0.83	0.50	0.00
17	H	0.45	0.73	0.53	55	Cu	0.33	0.00	0.18	93	Cu	0.67	0.50	0.09
18	H	0.54	0.66	0.59	56	Cu	0.50	0.17	0.18	94	Cu	0.83	0.33	0.09
19	H	0.66	0.46	0.50	57	Cu	0.33	0.17	0.27	95	Cu	0.67	0.33	0.18
20	H	0.45	0.54	0.46	58	Cu	0.50	0.00	0.27	96	Cu	0.83	0.50	0.18
21	Cu	0.00	0.00	0.00	59	Cu	0.33	1.00	0.35	97	Cu	0.67	0.50	0.27
22	Cu	0.17	0.17	0.00	60	Cu	0.50	0.16	0.36	98	Cu	0.83	0.33	0.27
23	Cu	0.00	0.17	0.09	61	Cu	0.33	0.33	0.00	99	Cu	0.67	0.34	0.36
24	Cu	0.17	0.00	0.09	62	Cu	0.50	0.50	0.00	100	Cu	0.84	0.50	0.35
25	Cu	1.00	0.00	0.18	63	Cu	0.33	0.50	0.09	101	Cu	0.67	0.67	0.00
26	Cu	0.17	0.17	0.18	64	Cu	0.50	0.33	0.09	102	Cu	0.83	0.83	0.00
27	Cu	0.00	0.17	0.27	65	Cu	0.33	0.33	0.18	103	Cu	0.67	0.83	0.09
28	Cu	0.17	0.00	0.27	66	Cu	0.50	0.50	0.18	104	Cu	0.83	0.67	0.09
29	Cu	0.00	1.00	0.35	67	Cu	0.33	0.50	0.27	105	Cu	0.67	0.67	0.18
30	Cu	0.17	0.17	0.35	68	Cu	0.50	0.33	0.27	106	Cu	0.83	0.83	0.18
31	Cu	0.00	0.33	0.00	69	Cu	0.33	0.34	0.35	107	Cu	0.67	0.83	0.27
32	Cu	0.17	0.50	0.00	70	Cu	0.50	0.50	0.35	108	Cu	0.83	0.67	0.27
33	Cu	0.00	0.50	0.09	71	Cu	0.33	0.67	0.00	109	Cu	0.67	0.67	0.35
34	Cu	0.17	0.33	0.09	72	Cu	0.50	0.83	0.00	110	Cu	0.83	0.83	0.35

Table G.2: Unit cell vectors and fractional coordinates for the optimized adsorption geometry of R-3MCHO on unreconstructed Cu (110) as calculated by PBE-B88. The unit cell vectors are given in Angstrom. Atomic positions are given in fraction of the unit cell vectors.

		x	y	z	No	Atom	a	b	c	No	Atom	a	b	c
	a	10.88	0.00	0.00	17	H	0.80	0.94	0.44	37	Cu	0.50	0.13	0.19
	b	0.00	10.25	0.00	18	H	0.67	0.91	0.49	38	Cu	0.50	0.37	0.19
	c	0.00	0.00	20.00	19	H	0.47	0.93	0.37	39	Cu	0.50	0.63	0.19
No	Atom	a	b	c	20	H	0.67	0.05	0.36	40	Cu	0.50	0.88	0.19
1	C	0.66	0.17	0.45	21	Cu	0.67	0.00	0.25	41	Cu	0.17	0.12	0.19
2	C	0.46	0.27	0.41	22	Cu	0.67	0.25	0.25	42	Cu	0.17	0.38	0.19
3	C	0.60	0.29	0.42	23	Cu	0.67	0.50	0.25	43	Cu	0.17	0.63	0.19
4	C	0.43	0.14	0.38	24	Cu	0.67	0.75	0.25	44	Cu	0.17	0.87	0.19
5	C	0.49	0.02	0.41	25	Cu	0.33	1.00	0.25	45	Cu	0.67	0.00	0.13
6	C	0.63	0.04	0.41	26	Cu	0.33	0.26	0.25	46	Cu	0.67	0.25	0.13
7	C	0.70	0.92	0.44	27	Cu	0.33	0.50	0.25	47	Cu	0.67	0.50	0.13
8	O	0.35	0.13	0.33	28	Cu	0.33	0.75	0.25	48	Cu	0.67	0.75	0.13
9	H	0.63	0.30	0.36	29	Cu	0.00	0.00	0.25	49	Cu	0.33	0.00	0.13
10	H	0.63	0.16	0.50	30	Cu	0.00	0.25	0.25	50	Cu	0.33	0.25	0.13
11	H	0.46	0.00	0.46	31	Cu	0.00	0.50	0.25	51	Cu	0.33	0.50	0.13
12	H	0.62	0.38	0.44	32	Cu	0.00	0.75	0.25	52	Cu	0.33	0.75	0.13
13	H	0.76	0.18	0.45	33	Cu	0.83	0.13	0.19	53	Cu	0.00	0.00	0.13
14	H	0.42	0.27	0.46	34	Cu	0.83	0.38	0.19	54	Cu	0.00	0.25	0.13
15	H	0.41	0.34	0.38	35	Cu	0.83	0.63	0.19	55	Cu	0.00	0.50	0.13
16	H	0.68	0.84	0.41	36	Cu	0.83	0.87	0.19	56	Cu	0.00	0.75	0.13

Table G.3: Unit cell vectors and fractional coordinates for the optimized adsorption geometry of R-3MCHO on unreconstructed Cu (111) as calculated by PBE-B88. The unit cell vectors are given in Angstrom. Atomic positions are given in fraction of the unit cell vectors.

		x	y	z	No	Atom	a	b	c	No	Atom	a	b	c
	a	10.25	0.00	0.00	21	Cu	0.67	0.17	0.33	45	Cu	0.25	0.75	0.25
	b	5.13	8.88	0.00	22	Cu	0.41	0.17	0.33	46	Cu	1.00	0.75	0.25
	c	0.00	0.00	25.00	23	Cu	0.92	0.17	0.33	47	Cu	0.50	0.75	0.25
No	Atom	a	b	c	24	Cu	0.17	0.92	0.33	48	Cu	1.00	0.50	0.25
1	C	0.36	0.32	0.48	25	Cu	0.17	0.17	0.33	49	Cu	0.75	0.50	0.25
2	C	0.26	0.49	0.48	26	Cu	0.92	0.92	0.33	50	Cu	0.75	0.75	0.25
3	C	0.51	0.27	0.45	27	Cu	0.92	0.42	0.33	51	Cu	0.25	0.50	0.25
4	C	0.34	0.57	0.50	28	Cu	0.42	0.92	0.33	52	Cu	0.50	0.50	0.25
5	C	0.59	0.34	0.47	29	Cu	0.92	0.67	0.33	53	Cu	0.09	0.33	0.16
6	C	0.49	0.52	0.47	30	Cu	0.67	0.67	0.33	54	Cu	0.09	0.83	0.16
7	C	0.58	0.60	0.49	31	Cu	0.17	0.67	0.33	55	Cu	0.33	0.09	0.16
8	O	0.55	0.18	0.41	32	Cu	0.17	0.42	0.33	56	Cu	0.33	0.33	0.16
9	H	0.22	0.53	0.44	33	Cu	0.42	0.67	0.33	57	Cu	0.33	0.59	0.16
10	H	0.37	0.54	0.54	34	Cu	0.67	0.91	0.33	58	Cu	0.33	0.83	0.16
11	H	0.63	0.31	0.51	35	Cu	0.67	0.42	0.33	59	Cu	0.59	0.33	0.16
12	H	0.16	0.53	0.50	36	Cu	0.41	0.42	0.33	60	Cu	0.59	0.83	0.16
13	H	0.27	0.69	0.49	37	Cu	0.75	0.00	0.25	61	Cu	0.83	0.09	0.16
14	H	0.38	0.28	0.52	38	Cu	0.50	0.25	0.25	62	Cu	0.83	0.33	0.16
15	H	0.30	0.26	0.46	39	Cu	0.75	0.25	0.25	63	Cu	0.83	0.59	0.16
16	H	0.68	0.56	0.46	40	Cu	0.50	0.00	0.25	64	Cu	0.83	0.83	0.16
17	H	0.51	0.72	0.48	41	Cu	0.25	0.25	0.25	65	Cu	0.08	0.08	0.16
18	H	0.61	0.57	0.53	42	Cu	1.00	0.00	0.25	66	Cu	0.08	0.58	0.16
19	H	0.69	0.31	0.45	43	Cu	0.25	0.00	0.25	67	Cu	0.58	0.08	0.16
20	H	0.46	0.55	0.42	44	Cu	1.00	0.25	0.25	68	Cu	0.58	0.58	0.16

APPENDIX H

STRUCTURAL INFORMATION FOR THE OPTIMIZED ADSORPTION GEOMETRY AND NEB IMAGES OF THE HYDROGENATION OF FORMALDEHYDE AND METHOXIDE ON COPPER SURFACES

Table H.1: Unit cell vectors and fractional coordinates for the optimized Cu(111) surface. The unit cell vectors are given in Angstrom. Atomic positions are given in fraction of the unit cell vectors.

		x	y	z	No	Atom	a	b	c	No	Atom	a	b	c
	a	7.71	0.00	0.00	8	Cu	0.78	0.11	0.07	18	Cu	0.67	0.33	0.13
	b	3.86	6.68	0.00	9	Cu	0.67	0.00	0.13	19	Cu	0.22	0.89	0.00
	c	0.00	0.00	31.48	10	Cu	0.22	0.56	0.00	20	Cu	0.11	0.78	0.07
No	Atom	a	b	c	11	Cu	0.11	0.44	0.07	21	Cu	0.00	0.67	0.13
1	Cu	0.22	0.22	0.00	12	Cu	0.00	0.33	0.13	22	Cu	0.56	0.89	0.00
2	Cu	0.11	0.11	0.07	13	Cu	0.56	0.56	0.00	23	Cu	0.44	0.78	0.07
3	Cu	0.00	0.00	0.13	14	Cu	0.44	0.44	0.07	24	Cu	0.33	0.67	0.13
4	Cu	0.56	0.22	0.00	15	Cu	0.33	0.33	0.13	25	Cu	0.89	0.89	0.00
5	Cu	0.44	0.11	0.07	16	Cu	0.89	0.56	0.00	26	Cu	0.78	0.78	0.07
6	Cu	0.33	0.00	0.13	17	Cu	0.78	0.44	0.07	27	Cu	0.67	0.67	0.13
7	Cu	0.89	0.22	0.00										

Table H.2: Fractional coordinates for the optimized adsorption of formaldehyde on Cu(111). Atomic positions are given in fraction of the Cu(111) unit cell vector.

No	Atom	a	b	c
1	C	0.22	1.00	0.24
2	H	0.23	0.14	0.23
3	H	0.36	0.85	0.23
4	O	0.06	0.01	0.24

Table H.3: Fractional coordinates for the TS of the hydrogenation of formaldehyde on Cu(111). Atomic positions are given in fraction of the Cu(111) unit cell vector.

No	Atom	a	b	c
1	C	0.16	0.09	0.22
2	H	0.21	0.15	0.19
3	H	0.08	0.21	0.24
4	H	0.30	-0.03	0.23
5	O	0.03	0.02	0.20

Table H.4: Fractional coordinates for the optimized adsorption of methoxide on Cu(111). Atomic positions are given in fraction of the Cu(111) unit cell vector.

No	Atom	a	b	c
1	C	0.23	0.23	0.22
2	H	0.15	0.16	0.23
3	H	0.16	0.38	0.23
4	H	0.39	0.15	0.23
5	O	0.22	0.22	0.17

Table H.5: Fractional coordinates for the TS of the hydrogenation of methoxide on Cu(111). Atomic positions are given in fraction of the Cu(111) unit cell vector.

No	Atom	a	b	c
1	C	0.15	0.29	0.25
2	H	0.88	0.32	0.24
3	H	0.28	0.22	0.23
4	H	0.09	0.45	0.25
5	H	0.18	0.22	0.28
6	O	0.01	0.25	0.22

Table H.6: Fractional coordinates for the optimized adsorption of methanol on Cu(111). Atomic positions are given in fraction of the Cu(111) unit cell vector.

No	Atom	a	b	c
1	C	0.23	0.21	0.22
2	H	0.87	0.22	0.16
3	H	0.39	0.14	0.23
4	H	0.15	0.37	0.23
5	H	0.16	0.13	0.23
6	O	0.23	0.22	0.17

Table H.7: Unit cell vectors and fractional coordinates for the optimized Cu(211) surface. The unit cell vectors are given in Angstrom. Atomic positions are given in fraction of the unit cell vectors.

		x	y	z	No	Atom	a	b	c	No	Atom	a	b	c
	a	6.25	0.00	0.00	8	Cu	0.65	0.34	0.15	18	Cu	0.67	0.83	0.07
	b	0.00	7.64	0.00	9	Cu	0.65	0.67	0.15	19	Cu	0.00	0.00	0.05
	c	0.00	0.00	29.43	10	Cu	-0.01	0.17	0.13	20	Cu	0.00	0.33	0.05
No	Atom	a	b	c	11	Cu	0.99	0.50	0.13	21	Cu	0.00	0.67	0.05
1	Cu	-0.01	0.99	0.20	12	Cu	0.98	0.84	0.13	22	Cu	0.33	0.17	0.02
2	Cu	-0.01	0.34	0.20	13	Cu	0.33	0.00	0.10	23	Cu	0.33	0.50	0.02
3	Cu	-0.01	0.67	0.20	14	Cu	0.33	0.33	0.10	24	Cu	0.33	0.83	0.02
4	Cu	0.32	0.17	0.18	15	Cu	0.33	0.67	0.10	25	Cu	0.67	0.00	0.00
5	Cu	0.32	0.50	0.18	16	Cu	0.67	0.17	0.07	26	Cu	0.67	0.33	0.00
6	Cu	0.32	0.83	0.18	17	Cu	0.67	0.50	0.07	27	Cu	0.67	0.67	0.00
7	Cu	0.65	1.00	0.15										

Table H.8: Fractional coordinates for the optimized adsorption of formaldehyde on Cu(211). Atomic positions are given in fraction of the Cu(211) unit cell vector.

No	Atom	a	b	c
1	C	0.63	0.17	0.25
2	H	0.55	0.29	0.26
3	H	0.54	0.04	0.26
4	O	0.83	0.17	0.25

Table H.9: Fractional coordinates for the TS of the hydrogenation of formaldehyde on Cu(111). Atomic positions are given in fraction of the Cu(211) unit cell vector.

No	Atom	a	b	c
1	C	0.50	0.13	0.29
2	H	0.44	0.18	0.32
3	H	0.58	0.20	0.30
4	H	0.52	0.99	0.30
5	O	0.47	0.16	0.25

Table H.10: Fractional coordinates for the optimized adsorption of methoxide on Cu(211). Atomic positions are given in fraction of the Cu(211) unit cell vector.

No	Atom	a	b	c
1	C	0.21	0.17	0.29
2	H	0.17	0.28	0.30
3	H	0.16	0.05	0.30
4	H	0.39	0.16	0.28
5	O	0.12	0.17	0.24

Table H.11: Fractional coordinates for the TS of the hydrogenation of methoxide on Cu(211). Atomic positions are given in fraction of the Cu(211) unit cell vector.

No	Atom	a	b	c
1	C	1.17	0.22	0.29
2	H	1.10	0.21	0.32
3	H	1.29	0.33	0.29
4	H	1.25	0.10	0.28
5	H	1.19	0.49	0.22
6	O	1.00	0.26	0.26

Table H.12: Fractional coordinates for the optimized adsorption of methanol on Cu(211). Atomic positions are given in fraction of the Cu(211) unit cell vector.

No	Atom	a	b	c
1	C	0.60	0.15	0.29
2	H	0.53	0.14	0.31
3	H	0.64	0.27	0.29
4	H	0.65	0.04	0.29
5	H	0.57	0.52	0.22
6	O	0.57	0.15	0.24

Table H.13: Unit cell vectors and fractional coordinates for the optimized Cu(221) surface. The unit cell vectors are given in Angstrom. Atomic positions are given in fraction of the unit cell vectors.

		x	y	z	No	Atom	a	b	c	No	Atom	a	b	c
	a	15.42	0.00	0.00	31	Cu	0.31	0.17	0.40	64	Cu	0.61	0.00	0.29
	b	0.00	10.28	0.00	32	Cu	0.31	0.50	0.40	65	Cu	0.61	0.33	0.29
	c	0.00	0.00	21.81	33	Cu	0.31	0.83	0.40	66	Cu	0.61	0.67	0.29
No	Atom	a	b	c	34	Cu	0.81	0.17	0.40	67	Cu	0.47	0.17	0.27
1	Cu	0.45	0.00	0.42	35	Cu	0.81	0.50	0.40	68	Cu	0.47	0.50	0.27
2	Cu	0.00	0.00	0.50	36	Cu	0.81	0.83	0.40	69	Cu	0.47	0.83	0.27
3	Cu	0.00	0.33	0.50	37	Cu	0.17	0.00	0.38	70	Cu	0.97	0.17	0.27
4	Cu	0.00	0.67	0.50	38	Cu	0.17	0.33	0.38	71	Cu	0.97	0.50	0.27
5	Cu	0.50	0.00	0.50	39	Cu	0.17	0.67	0.38	72	Cu	0.97	0.83	0.27
6	Cu	0.50	0.34	0.50	40	Cu	0.67	1.00	0.37	73	Cu	0.33	0.00	0.25
7	Cu	0.50	0.66	0.50	41	Cu	0.67	0.33	0.38	74	Cu	0.33	0.33	0.25
8	Cu	0.36	0.17	0.48	42	Cu	0.67	0.67	0.38	75	Cu	0.33	0.67	0.25
9	Cu	0.36	0.50	0.48	43	Cu	0.03	0.17	0.35	76	Cu	0.83	0.00	0.25
10	Cu	0.36	0.83	0.48	44	Cu	0.03	0.50	0.35	77	Cu	0.83	0.33	0.25
11	Cu	0.86	0.17	0.48	45	Cu	0.03	0.83	0.35	78	Cu	0.83	0.67	0.25
12	Cu	0.86	0.50	0.48	46	Cu	0.53	0.17	0.35	79	Cu	0.19	0.17	0.23
13	Cu	0.86	0.83	0.48	47	Cu	0.53	0.50	0.35	80	Cu	0.19	0.50	0.23
14	Cu	0.23	0.00	0.46	48	Cu	0.53	0.83	0.35	81	Cu	0.19	0.83	0.23
15	Cu	0.23	0.33	0.46	49	Cu	0.39	0.00	0.33	82	Cu	0.69	0.17	0.23
16	Cu	0.23	0.67	0.46	50	Cu	0.39	0.33	0.33	83	Cu	0.69	0.50	0.23
17	Cu	0.73	0.00	0.46	51	Cu	0.39	0.67	0.33	84	Cu	0.69	0.83	0.23
18	Cu	0.73	0.34	0.46	52	Cu	0.89	0.00	0.33	85	Cu	0.06	0.00	0.21
19	Cu	0.73	0.66	0.46	53	Cu	0.89	0.33	0.33	86	Cu	0.06	0.33	0.21
20	Cu	0.09	0.17	0.44	54	Cu	0.89	0.67	0.33	87	Cu	0.06	0.67	0.21
21	Cu	0.09	0.50	0.44	55	Cu	0.25	0.17	0.31	88	Cu	0.56	0.00	0.21
22	Cu	0.09	0.83	0.44	56	Cu	0.25	0.50	0.31	89	Cu	0.56	0.33	0.21
23	Cu	0.59	0.17	0.44	57	Cu	0.25	0.83	0.31	90	Cu	0.56	0.67	0.21
24	Cu	0.59	0.50	0.44	58	Cu	0.75	0.17	0.31	91	Cu	0.42	0.17	0.19
25	Cu	0.59	0.83	0.44	59	Cu	0.75	0.50	0.31	92	Cu	0.42	0.50	0.19
26	Cu	0.45	0.33	0.42	60	Cu	0.75	0.83	0.31	93	Cu	0.42	0.83	0.19
27	Cu	0.45	0.67	0.42	61	Cu	0.11	0.00	0.29	94	Cu	0.92	0.17	0.19
28	Cu	0.95	0.00	0.42	62	Cu	0.11	0.33	0.29	95	Cu	0.92	0.50	0.19
29	Cu	0.95	0.33	0.42	63	Cu	0.11	0.67	0.29	96	Cu	0.92	0.83	0.19
30	Cu	0.95	0.67	0.42										

Table H.14: Fractional coordinates for the optimized adsorption of formaldehyde on Cu(221). Atomic positions are given in fraction of the Cu(221) unit cell vector.

No	Atom	a	b	c
1	C	0.11	0.17	0.44
2	H	0.13	0.18	0.49
3	H	0.15	0.11	0.41
4	O	0.05	0.24	0.42

Table H.15: Fractional coordinates for the TS of the hydrogenation of formaldehyde on Cu(221). Atomic positions are given in fraction of the Cu(221) unit cell vector.

No	Atom	a	b	c
1	C	0.05	0.03	0.47
2	H	0.57	0.08	0.51
3	H	0.09	-0.04	0.47
4	H	0.16	-0.07	0.49
5	O	0.04	0.06	0.44

Table H.16: Fractional coordinates for the optimized adsorption of methoxide on Cu(221). Atomic positions are given in fraction of the Cu(221) unit cell vector.

No	Atom	a	b	c
1	C	0.99	0.88	0.46
2	H	0.00	0.98	0.48
3	H	0.02	0.81	0.49
4	H	0.92	0.86	0.46
5	O	0.02	0.88	0.40

Table H.17: Fractional coordinates for the TS of the hydrogenation of methoxide on Cu(221). Atomic positions are given in fraction of the Cu(221) unit cell vector.

No	Atom	a	b	c
1	C	0.05	0.02	0.49
2	H	0.57	0.09	0.50
3	H	0.08	0.01	0.51
4	H	0.97	0.99	0.50
5	H	0.27	0.06	0.45
6	O	0.05	0.00	0.42

Table H.18: Fractional coordinates for the optimized adsorption of methanol on Cu(221). Atomic positions are given in fraction of the Cu(221) unit cell vector.

No	Atom	a	b	c
1	C	0.10	0.11	0.47
2	H	0.13	0.20	0.48
3	H	0.14	0.02	0.48
4	H	0.03	0.10	0.49
5	H	0.14	0.12	0.38
6	O	0.08	0.12	0.40

APPENDIX I

STRUCTURAL INFORMATION FOR THE OPTIMIZED ADSORPTION GEOMETRY AND NEB IMAGES OF THE HYDROGENATION OF FORMALDEHYDE AND METHOXIDE ON ZINC MODIFIED COPPER SURFACES

Table I.1: Unit cell vectors and fractional coordinates for the optimized Zn modified Cu(211) surface. The unit cell vectors are given in Angstrom. Atomic positions are given in fraction of the unit cell vectors.

		x	y	z	No	Atom	a	b	c	No	Atom	a	b	c
	a	12.49	0.00	0.00	17	Cu	0.33	0.17	0.07	36	Cu	0.83	0.67	0.15
	b	0.00	7.64	0.00	18	Cu	0.33	0.50	0.07	37	Cu	1.00	0.17	0.13
	c	0.00	0.00	29.43	19	Cu	0.33	0.83	0.07	38	Cu	0.50	0.50	0.13
No	Atom	a	b	c	20	Cu	0.00	0.00	0.05	39	Cu	1.00	0.83	0.13
1	Zn	0.00	0.00	0.20	21	Cu	0.00	0.33	0.05	40	Cu	0.66	0.00	0.10
2	Zn	0.50	0.00	0.20	22	Cu	0.00	0.67	0.05	41	Cu	0.67	0.33	0.10
3	Cu	1.00	0.33	0.20	23	Cu	0.17	0.17	0.02	42	Cu	0.67	0.67	0.10
4	Cu	1.00	0.67	0.20	24	Cu	0.17	0.50	0.02	43	Cu	0.83	0.17	0.07
5	Cu	0.17	0.17	0.18	25	Cu	0.17	0.83	0.02	44	Cu	0.83	0.50	0.07
6	Cu	0.17	0.50	0.18	26	Cu	0.33	0.00	0.00	45	Cu	0.83	0.83	0.07
7	Cu	0.17	0.84	0.18	27	Cu	0.33	0.33	0.00	46	Cu	0.50	0.00	0.05
8	Cu	0.33	0.00	0.15	28	Cu	0.33	0.67	0.00	47	Cu	0.50	0.33	0.05
9	Cu	0.33	0.34	0.15	29	Cu	0.50	0.33	0.20	48	Cu	0.50	0.67	0.05
10	Cu	0.33	0.67	0.15	30	Cu	0.50	0.67	0.20	49	Cu	0.67	0.17	0.02
11	Cu	0.50	0.17	0.13	31	Cu	0.66	0.17	0.18	50	Cu	0.67	0.50	0.02
12	Cu	0.99	0.50	0.12	32	Cu	0.66	0.50	0.18	51	Cu	0.67	0.83	0.02
13	Cu	0.50	0.83	0.12	33	Cu	0.67	0.83	0.18	52	Cu	0.83	0.00	0.00
14	Cu	0.17	0.00	0.10	34	Cu	0.83	0.00	0.15	53	Cu	0.83	0.33	0.00
15	Cu	0.16	0.33	0.10	35	Cu	0.83	0.33	0.15	54	Cu	0.83	0.67	0.00
16	Cu	0.16	0.67	0.10										

Table I.2: Fractional coordinates for the optimized adsorption of formaldehyde on Zn modified Cu(211). Atomic positions are given in fraction of the Zn modified Cu(211) unit cell vector.

No	Atom	a	b	c
1	C	0.51	0.34	0.30
2	H	0.50	0.42	0.34
3	H	0.56	0.22	0.30
4	O	0.47	0.40	0.27

Table I.3: Fractional coordinates for the TS for the hydrogenation of formaldehyde on Zn modified Cu(211). Atomic positions are given in fraction of the Zn modified Cu(211) unit cell vector.

No	Atom	a	b	c
1	C	0.51	0.09	0.32
2	H	0.49	0.19	0.34
3	H	0.51	-0.03	0.33
4	H	0.33	0.16	0.28
5	O	0.47	0.11	0.28

Table I.4: Fractional coordinates for the optimized adsorption of methoxide on Zn modified Cu(211). Atomic positions are given in fraction of the Zn modified Cu(211) unit cell vector.

No	Atom	a	b	c
1	C	0.50	0.83	0.30
2	H	0.48	0.95	0.31
3	H	0.47	0.71	0.31
4	H	0.59	0.82	0.30
5	O	0.47	0.83	0.25

Table I.5: Fractional coordinates for the TS for the hydrogenation of methoxide on Zn modified Cu(211). Atomic positions are given in fraction of the Zn modified Cu(211) unit cell vector.

No	Atom	a	b	c
1	C	0.55	0.00	0.31
2	H	0.51	0.06	0.33
3	H	0.56	0.00	0.32
4	H	0.62	0.93	2.99
5	H	0.37	0.58	0.25
6	O	0.51	0.00	0.26

Table I.6: Fractional coordinates for the optimized adsorption of methanol on Zn modified Cu(211). Atomic positions are given in fraction of the Zn modified Cu(211) unit cell vector.

No	Atom	a	b	c
1	C	0.61	0.17	0.28
2	H	0.54	0.17	0.31
3	H	0.66	0.28	0.29
4	H	0.66	0.05	0.29
5	H	0.66	0.67	0.24
6	O	0.56	0.17	0.24

Table I.7: Unit cell vectors and fractional coordinates for the optimized Zn modified Cu(221) surface. The unit cell vectors are given in Angstrom. Atomic positions are given in fraction of the unit cell vectors.

		x	y	z	No	Atom	a	b	c	No	Atom	a	b	c
	a	15.42	0	0	31	Cu	0.59	0.62	0.25	64	Cu	0.53	0.88	0.14
	b	0	10.3	0	32	Cu	0.59	0.88	0.25	65	Cu	0.39	0.00	0.11
	c	0	0	21.81	33	Cu	0.45	0.00	0.22	66	Cu	0.39	0.25	0.11
No	Atom	a	b	c	34	Cu	0.45	0.25	0.22	67	Cu	0.39	0.50	0.11
1	Zn	0.01	0.99	0.34	35	Cu	0.45	0.50	0.22	68	Cu	0.39	0.75	0.11
2	Zn	0.00	0.26	0.33	36	Cu	0.45	0.75	0.22	69	Cu	0.89	0.00	0.11
3	Cu	1.00	0.50	0.33	37	Cu	0.95	0.00	0.22	70	Cu	0.89	0.25	0.11
4	Cu	1.00	0.75	0.33	38	Cu	0.95	0.25	0.22	71	Cu	0.89	0.50	0.11
5	Cu	0.50	0.00	0.33	39	Cu	0.95	0.50	0.22	72	Cu	0.89	0.75	0.11
6	Cu	0.50	0.25	0.33	40	Cu	0.95	0.75	0.22	73	Cu	0.25	0.12	0.08
7	Cu	0.50	0.50	0.33	41	Cu	0.31	0.13	0.19	74	Cu	0.25	0.37	0.08
8	Cu	0.50	0.75	0.33	42	Cu	0.31	0.38	0.19	75	Cu	0.25	0.62	0.08
9	Cu	0.36	0.13	0.30	43	Cu	0.31	0.63	0.19	76	Cu	0.25	0.87	0.08
10	Cu	0.36	0.38	0.30	44	Cu	0.31	0.88	0.19	77	Cu	0.75	0.12	0.08
11	Cu	0.36	0.63	0.30	45	Cu	0.81	0.12	0.20	78	Cu	0.75	0.37	0.08
12	Cu	0.36	0.88	0.30	46	Cu	0.81	0.37	0.19	79	Cu	0.75	0.62	0.08
13	Cu	0.86	0.12	0.31	47	Cu	0.81	0.62	0.19	80	Cu	0.75	0.87	0.08
14	Cu	0.86	0.38	0.30	48	Cu	0.81	0.88	0.19	81	Cu	0.11	0.00	0.06
15	Cu	0.86	0.62	0.30	49	Cu	0.17	1.00	0.17	82	Cu	0.11	0.25	0.06
16	Cu	0.86	0.87	0.30	50	Cu	0.17	0.25	0.17	83	Cu	0.11	0.50	0.06
17	Cu	0.22	0.00	0.28	51	Cu	0.17	0.50	0.17	84	Cu	0.11	0.75	0.06
18	Cu	0.22	0.25	0.28	52	Cu	0.17	0.75	0.17	85	Cu	0.61	0.00	0.06
19	Cu	0.23	0.50	0.28	53	Cu	0.67	0.00	0.17	86	Cu	0.61	0.25	0.06
20	Cu	0.23	0.75	0.28	54	Cu	0.67	0.25	0.17	87	Cu	0.61	0.50	0.06
21	Cu	0.73	1.00	0.28	55	Cu	0.67	0.50	0.17	88	Cu	0.61	0.75	0.06
22	Cu	0.72	0.25	0.28	56	Cu	0.67	0.75	0.17	89	Cu	0.47	0.12	0.03
23	Cu	0.72	0.50	0.28	57	Cu	0.03	0.13	0.14	90	Cu	0.47	0.37	0.03
24	Cu	0.72	0.75	0.28	58	Cu	0.03	0.38	0.14	91	Cu	0.47	0.62	0.03
25	Cu	0.09	0.13	0.25	59	Cu	0.03	0.62	0.14	92	Cu	0.47	0.87	0.03
26	Cu	0.09	0.38	0.25	60	Cu	0.03	0.88	0.14	93	Cu	0.97	0.12	0.03
27	Cu	0.09	0.62	0.25	61	Cu	0.53	0.12	0.14	94	Cu	0.97	0.37	0.03
28	Cu	0.09	0.88	0.25	62	Cu	0.53	0.37	0.14	95	Cu	0.97	0.62	0.03
29	Cu	0.59	0.12	0.25	63	Cu	0.53	0.63	0.14	96	Cu	0.97	0.87	0.03
30	Cu	0.59	0.37	0.25										

Table I.8: Fractional coordinates for the optimized adsorption of formaldehyde on Zn modified Cu(221). Atomic positions are given in fraction of the Zn modified Cu(221) unit cell vector.

No	Atom	a	b	c
1	C	0.10	0.96	0.47
2	H	0.16	0.98	0.50
3	H	0.06	0.88	0.48
4	O	0.09	1.03	0.42

Table I.9: Fractional coordinates for the TS for the hydrogenation of formaldehyde on Zn modified Cu(221). Atomic positions are given in fraction of the Zn modified Cu(221) unit cell vector.

No	Atom	a	b	c
1	C	-0.06	0.97	0.46
2	H	-0.04	1.04	0.49
3	H	-0.05	0.92	0.48
4	H	-0.10	0.93	0.47
5	O	0.01	0.99	0.41

Table I.10: Fractional coordinates for the optimized adsorption of methoxide on Zn modified Cu(221). Atomic positions are given in fraction of the Zn modified Cu(221) unit cell vector.

No	Atom	a	b	c
1	C	-0.22	1.00	0.42
2	H	-0.24	1.09	0.44
3	H	-0.16	0.97	0.45
4	H	-0.27	0.92	0.43
5	O	-0.20	1.00	0.36

Table I.11: Fractional coordinates for the TS for the hydrogenation of methoxide on Zn modified Cu(221). Atomic positions are given in fraction of the Zn modified Cu(221) unit cell vector.

No	Atom	a	b	c
1	C	-0.02	0.99	0.44
2	H	-0.04	1.10	0.45
3	H	0.04	0.97	0.44
4	H	-0.06	0.93	0.47
5	H	0.11	0.92	0.42
6	O	-0.04	0.97	0.38

Table I.12: Fractional coordinates for the optimized adsorption of methanol on Zn modified Cu(221). Atomic positions are given in fraction of the Zn modified Cu(221) unit cell vector.

No	Atom	a	b	c
1	C	0.17	0.99	0.46
2	H	0.17	1.10	0.46
3	H	0.24	0.97	0.44
4	H	0.16	0.94	0.50
5	H	0.15	0.91	0.38
6	O	0.11	0.95	0.41

APPENDIX J

STRUCTURAL INFORMATION FOR THE OPTIMIZED ADSORPTION GEOMETRY AND NEB IMAGES OF THE HYDROGENATION OF FORMALDEHYDE AND METHOXIDE ON ZIRCONIUM MODIFIED COPPER SURFACES

Table J.1: Unit cell vectors and fractional coordinates for the optimized Zr modified Cu(211) surface. The unit cell vectors are given in Angstrom. Atomic positions are given in fraction of the unit cell vectors.

		x	y	z	No	Atom	a	b	c	No	Atom	a	b	c
	a	12.49	0.00	0.00	17	Cu	0.33	0.17	0.07	36	Cu	0.83	0.67	0.15
	b	0.00	7.64	0.00	18	Cu	0.33	0.50	0.07	37	Cu	1.00	0.17	0.13
	c	0.00	0.00	29.43	19	Cu	0.33	0.83	0.07	38	Cu	0.50	0.50	0.13
No	Atom	a	b	c	20	Cu	0.00	0.00	0.05	39	Cu	1.00	0.83	0.13
1	Zr	0.00	0.00	0.20	21	Cu	0.00	0.33	0.05	40	Cu	0.66	0.00	0.10
2	Zr	0.50	0.00	0.20	22	Cu	0.00	0.67	0.05	41	Cu	0.67	0.33	0.10
3	Cu	1.00	0.33	0.20	23	Cu	0.17	0.17	0.02	42	Cu	0.67	0.67	0.10
4	Cu	1.00	0.67	0.20	24	Cu	0.17	0.50	0.02	43	Cu	0.83	0.17	0.07
5	Cu	0.17	0.17	0.18	25	Cu	0.17	0.83	0.02	44	Cu	0.83	0.50	0.07
6	Cu	0.17	0.50	0.18	26	Cu	0.33	0.00	0.00	45	Cu	0.83	0.83	0.07
7	Cu	0.17	0.84	0.18	27	Cu	0.33	0.33	0.00	46	Cu	0.50	0.00	0.05
8	Cu	0.33	0.00	0.15	28	Cu	0.33	0.67	0.00	47	Cu	0.50	0.33	0.05
9	Cu	0.33	0.34	0.15	29	Cu	0.50	0.33	0.20	48	Cu	0.50	0.67	0.05
10	Cu	0.33	0.67	0.15	30	Cu	0.50	0.67	0.20	49	Cu	0.67	0.17	0.02
11	Cu	0.50	0.17	0.13	31	Cu	0.66	0.17	0.18	50	Cu	0.67	0.50	0.02
12	Cu	0.99	0.50	0.12	32	Cu	0.66	0.50	0.18	51	Cu	0.67	0.83	0.02
13	Cu	0.50	0.83	0.12	33	Cu	0.67	0.83	0.18	52	Cu	0.83	0.00	0.00
14	Cu	0.17	0.00	0.10	34	Cu	0.83	0.00	0.15	53	Cu	0.83	0.33	0.00
15	Cu	0.16	0.33	0.10	35	Cu	0.83	0.33	0.15	54	Cu	0.83	0.67	0.00
16	Cu	0.16	0.67	0.10										

Table J.2: Fractional coordinates for the optimized adsorption of formaldehyde on Zr modified Cu(211). Atomic positions are given in fraction of the Zr modified Cu(211) unit cell vector.

No	Atom	a	b	c
1	C	0.48	0.33	0.31
2	H	0.51	0.43	0.33
3	H	0.60	0.21	0.30
4	O	0.50	0.38	0.26

Table J.3: Fractional coordinates for the TS for the hydrogenation of formaldehyde on Zr modified Cu(211). Atomic positions are given in fraction of the Zr modified Cu(211) unit cell vector.

No	Atom	a	b	c
1	C	0.53	0.09	0.30
2	H	0.44	0.18	0.32
3	H	0.53	0.01	0.31
4	H	0.51	0.09	0.31
5	O	0.47	0.12	0.27

Table J.4: Fractional coordinates for the optimized adsorption of methoxide on Zr modified Cu(211). Atomic positions are given in fraction of the Zr modified Cu(211) unit cell vector.

No	Atom	a	b	c
1	C	0.49	-0.13	0.29
2	H	0.51	-0.03	0.31
3	H	0.49	-0.24	0.31
4	H	0.64	-0.22	0.30
5	O	0.45	-0.17	0.24

Table J.5: Fractional coordinates for the TS for the hydrogenation of methoxide on Zr modified Cu(211). Atomic positions are given in fraction of the Zr modified Cu(211) unit cell vector.

No	Atom	a	b	c
1	C	0.58	-0.02	0.30
2	H	0.50	0.07	0.32
3	H	0.58	-0.04	0.29
4	H	0.58	-0.11	0.30
5	H	0.62	0.54	0.27
6	O	0.55	-0.04	0.24

Table J.6: Fractional coordinates for the optimized adsorption of methanol on Zr modified Cu(211). Atomic positions are given in fraction of the Zr modified Cu(211) unit cell vector.

No	Atom	a	b	c
1	C	0.57	0.12	0.27
2	H	0.52	0.14	0.32
3	H	0.69	0.30	0.28
4	H	0.63	0.05	0.30
5	H	0.67	0.65	0.25
6	O	0.57	0.16	0.23

Table J.7: Unit cell vectors and fractional coordinates for the optimized Zr modified Cu(221) surface. The unit cell vectors are given in Angstrom. Atomic positions are given in fraction of the unit cell vectors.

		x	y	z	No	Atom	a	b	c	No	Atom	a	b	c
	a	15.42	0	0	31	Cu	0.59	0.62	0.25	64	Cu	0.53	0.88	0.14
	b	0	10.3	0	32	Cu	0.59	0.88	0.25	65	Cu	0.39	0.00	0.11
	c	0	0	21.81	33	Cu	0.45	0.00	0.22	66	Cu	0.39	0.25	0.11
No	Atom	a	b	c	34	Cu	0.45	0.25	0.22	67	Cu	0.39	0.50	0.11
1	Zr	0.01	0.00	0.34	35	Cu	0.45	0.50	0.22	68	Cu	0.39	0.75	0.11
2	Zr	0.00	0.24	0.34	36	Cu	0.45	0.75	0.22	69	Cu	0.89	0.00	0.11
3	Cu	1.00	0.50	0.33	37	Cu	0.95	0.00	0.22	70	Cu	0.89	0.25	0.11
4	Cu	1.00	0.75	0.33	38	Cu	0.95	0.25	0.22	71	Cu	0.89	0.50	0.11
5	Cu	0.50	0.00	0.33	39	Cu	0.95	0.50	0.22	72	Cu	0.89	0.75	0.11
6	Cu	0.50	0.25	0.33	40	Cu	0.95	0.75	0.22	73	Cu	0.25	0.12	0.08
7	Cu	0.50	0.50	0.33	41	Cu	0.31	0.13	0.19	74	Cu	0.25	0.37	0.08
8	Cu	0.50	0.75	0.33	42	Cu	0.31	0.38	0.19	75	Cu	0.25	0.62	0.08
9	Cu	0.36	0.13	0.30	43	Cu	0.31	0.63	0.19	76	Cu	0.25	0.87	0.08
10	Cu	0.36	0.38	0.30	44	Cu	0.31	0.88	0.19	77	Cu	0.75	0.12	0.08
11	Cu	0.36	0.63	0.30	45	Cu	0.81	0.12	0.20	78	Cu	0.75	0.37	0.08
12	Cu	0.36	0.88	0.30	46	Cu	0.81	0.37	0.19	79	Cu	0.75	0.62	0.08
13	Cu	0.86	0.12	0.31	47	Cu	0.81	0.62	0.19	80	Cu	0.75	0.87	0.08
14	Cu	0.86	0.38	0.30	48	Cu	0.81	0.88	0.19	81	Cu	0.11	0.00	0.06
15	Cu	0.86	0.62	0.30	49	Cu	0.17	1.00	0.17	82	Cu	0.11	0.25	0.06
16	Cu	0.86	0.87	0.30	50	Cu	0.17	0.25	0.17	83	Cu	0.11	0.50	0.06
17	Cu	0.22	0.00	0.28	51	Cu	0.17	0.50	0.17	84	Cu	0.11	0.75	0.06
18	Cu	0.22	0.25	0.28	52	Cu	0.17	0.75	0.17	85	Cu	0.61	0.00	0.06
19	Cu	0.23	0.50	0.28	53	Cu	0.67	0.00	0.17	86	Cu	0.61	0.25	0.06
20	Cu	0.23	0.75	0.28	54	Cu	0.67	0.25	0.17	87	Cu	0.61	0.50	0.06
21	Cu	0.73	1.00	0.28	55	Cu	0.67	0.50	0.17	88	Cu	0.61	0.75	0.06
22	Cu	0.72	0.25	0.28	56	Cu	0.67	0.75	0.17	89	Cu	0.47	0.12	0.03
23	Cu	0.72	0.50	0.28	57	Cu	0.03	0.13	0.14	90	Cu	0.47	0.37	0.03
24	Cu	0.72	0.75	0.28	58	Cu	0.03	0.38	0.14	91	Cu	0.47	0.62	0.03
25	Cu	0.09	0.13	0.25	59	Cu	0.03	0.62	0.14	92	Cu	0.47	0.87	0.03
26	Cu	0.09	0.38	0.25	60	Cu	0.03	0.88	0.14	93	Cu	0.97	0.12	0.03
27	Cu	0.09	0.62	0.25	61	Cu	0.53	0.12	0.14	94	Cu	0.97	0.37	0.03
28	Cu	0.09	0.88	0.25	62	Cu	0.53	0.37	0.14	95	Cu	0.97	0.62	0.03
29	Cu	0.59	0.12	0.25	63	Cu	0.53	0.63	0.14	96	Cu	0.97	0.87	0.03
30	Cu	0.59	0.37	0.25										

Table J.8: Fractional coordinates for the optimized adsorption of formaldehyde on Zr modified Cu(221). Atomic positions are given in fraction of the Zr modified Cu(221) unit cell vector.

No	Atom	a	b	c
1	C	0.08	0.94	0.46
2	H	0.18	0.97	0.49
3	H	0.01	0.86	0.48
4	O	0.06	1.05	0.42

Table J.9: Fractional coordinates for the TS for the hydrogenation of formaldehyde on Zr modified Cu(221). Atomic positions are given in fraction of the Zr modified Cu(221) unit cell vector.

No	Atom	a	b	c
1	C	-0.06	0.93	0.45
2	H	0.00	1.06	0.49
3	H	-0.01	0.94	0.48
4	H	-0.10	0.96	0.47
5	O	0.00	1.00	0.40

Table J.10: Fractional coordinates for the optimized adsorption of methoxide on Zr modified Cu(221). Atomic positions are given in fraction of the Zr modified Cu(221) unit cell vector.

No	Atom	a	b	c
1	C	-0.20	0.98	0.42
2	H	-0.21	1.12	0.44
3	H	-0.15	0.93	0.45
4	H	-0.28	0.94	0.43
5	O	-0.24	1.04	0.35

Table J.11: Fractional coordinates for the TS for the hydrogenation of methoxide on Zr modified Cu(221). Atomic positions are given in fraction of the Zr modified Cu(221) unit cell vector.

No	Atom	a	b	c
1	C	-0.07	1.04	0.44
2	H	-0.06	1.10	0.45
3	H	0.00	0.93	0.45
4	H	-0.04	0.96	0.48
5	H	0.11	0.88	0.42
6	O	-0.04	0.95	0.39

Table J.12: Fractional coordinates for the optimized adsorption of methanol on Zr modified Cu(221). Atomic positions are given in fraction of the Zr modified Cu(221) unit cell vector.

No	Atom	a	b	c
1	C	0.21	0.98	0.46
2	H	0.20	1.12	0.46
3	H	0.26	0.98	0.44
4	H	0.12	0.94	0.49
5	H	0.13	0.93	0.38
6	O	0.15	0.96	0.42